STUDIES OF THE BETA DECAY OF LIGHT PROJECTILE FRAGMENTS FAR FROM STABILITY

By

David Mikolas

A DISSERTATION

Submitted to
Michigan State University
in partial fulfillment of the requirements
for the degree of

DOCTOR OF PHILOSOPHY

Department of Physics and Astronomy

1989

ABSTRACT

STUDIES OF THE BETA DECAY OF
LIGHT PROJECTILE FRAGMENTS
FAR FROM STABILITY

By

David Mikolas

Nuclei far from stability can be produced by the fragmentation of beams at the National Superconducting Cyclotron Laboratory at Michigan State University, and separated by the Reaction Product Mass Separator. Since these fragments maintain a significant fraction of the momentum of the beam broadened by the reaction dynamics, the beta decay of these nuclei can be observed only after they come to rest in a thick layer of material such as an active silicon detector. Here decay products such as the emitted ß particle and any ß-delayed charged particles can be detected and often their energy determined.

New techniques to study beta decay and beta delayed particle emission from projectile fragmentation have been developed. Problems such as the determination of absolute partial and total decay rates, contamination by other isotopes, background and daughter activity, fitting procedures where only a small number of events are available or where data are contaminated with other activity or background and energy calibration are discussed. Techniques for their management are presented.

The Nuclear Shell Model, with an empirical Hamiltonian based upon tabulated nuclear structure information from stable or close to stability nuclei, will benefit particularly from information of the

structure of nuclei far from stability for two reasons. At first, observables such as beta decay rates can be measured and compared to predictions. Any deviations might give insight into the limitations of the present Hamiltonians. Later as more information is gathered, a significant body of excited states will be compiled facilitating a new fit of the matrix elements of the Hamiltonian including far-from-stability configurations. It is however difficult to extract the standard quantities such as beta decay matrix elements from the data in a form comparable to the predicted values. Many levels will be unbound to nuclear decay, often to the emission of two or more particles. The distribution in phase space of all of these particles must somehow be interpreted with a reasonably simple model in order to extract beta decay matrix elements. In this thesis, a simple model is presented in order to interpret such data. This model incorporates the generalized density of states concept into the standard model of beta decay to bound levels.

To My Favorite Scientist
and my Love,
Hiroko Takayasu

ACKNOWLEDGMENTS

I was watching an episode of NOVA a while ago. Two senior scientists were reminiscing an evening which took place in the early days of radar. On that night they were graduate student and advisor, peering into space at a wavelength of a cm or so, seeing for the first time the universe calling out at 4°K. Their two faces became almost those of children as they recreated in their minds the excitement of that night.

The experience of gazing into the controls of some contraption in the middle of the night with my advisor at my side, learning something new about our universe is one which I shall not ever forget. Thank you, Jerry Nolen.

I want also to point out the miracle that my parents Eugene and Ailene Mikolas worked in nurturing ten billion base-pairs of DNA (a few picograms) into what I am today. Wow. They are responsible for putting me in college and making sure I stayed there.

Writing this thesis has been a long process. I hope that it was worth it. I therefore thank its audience Rick Harkewicz in advance, for his (hopefully) reading it.

This whole thing started when my grand-advisor Ruby Sherr was rummaging around in the p shell looking for trouble. He found it. The beta decay branching information for ^9C in Ajzenberg-Selove left a lot to the reader's imagination. He called up Jerry Nolen who told him where to put the ^9C, and there began the practice of implanting delayed

charged particle radioactivity in active Silicon detectors here at NSCL. Thanks Ruby.

I give special thanks to the members of my PhD. committee. They have been both helpful and patient. In particular, Alex Brown's tuition in Nuclear Physics gave to me a sense of purpose for this project. I hope that the techniques discussed in this thesis will ultimately repay him with lots and lots of B(GT)'s! Walter Benenson proved to be a source of guidance and support in both Physics and in the English language itself. I should also thank Jack Hetherington for simply being himself.

I want to emphasize that EVERYONE at NSCL is to be thanked for creating a warm, friendly environment in which to do research. I am always proud of this point when I describe this laboratory to others. If you have a question or need help, one only need wander down the hall and ask. Dick Blue, Ed Kashy, Dave Morrissey and Brad Sherrill have all provided essential help at some point. The NSCL Computer group deserves a standing ovation for maintaining an incredibly reliable network of computers and a damn good data aquisition environment which as far as I can tell surpasses that at any other Nuclear Physics Laboratory.

Michael Maier has been a consistent source of information and perspective. His door has always been open for questions - including those dumb 'emergency' questions. He has been an important resource for me throughout my stay here at NSCL.

Finally, I would like to thank Hiroko Takayasu for all kinds of things. If I did so, it would require another chapter. Instead, I'll just say 'Thanks Hiro!'

TABLE OF CONTENTS

LIST OF FIGURES

LIST OF TABLES

SECTION I

I. Introduction:

The beta decay properties of nuclei provide a view on the internal structure of the nucleus predominantly by the association of decay rates with the overlaps of calculated wave-functions and known or empirical operators. The study of the decay properties of nuclei far from stability allows us to put theories of nuclear structure and decay to the test. This is because most of the information used in the construction of these theories represents properties of nuclei very close to the line of stability[1]. Often, the beta decay will populate unbound levels. In this case further study of the nuclear structure can be extracted from the nuclear decay properties following beta decay. A recent compilation of beta decay data was produced by BROWN85. While the data spans decades of research, a clear peak in the number of 'new' nuclei measured and B(GT) (see Equation 2.4) occured. The number of newly accessible nuclei has diminished as the current production and detection technologies have matured. This trend is illustrated in Figure 1.1.

The characteristics of beta decay of nuclei far from stability differ from those closer to stability in many ways. The major difference lies in the greater amount of energy released in each decay. The available phase space for the electron and neutrino behaves roughly

1. The stability line is drawn on the Z,N axis. Z and N represent proton and neutron number respectively. The nuclei which define the stability line are those with the ratio of protons to neutrons which provide the lowest energy configuration for a given number of total nucleons (Z+N).

as the fifth power of decay energy, and thus half lives become dramatically shorter for those nuclei farther from stability.

Many more excited states become energetically accessible with the increase in available energy, and the binding energy of the daughter nucleus simultaneously decreases. This is illustrated in the series of graphs in Figure 1.2. Here the beta decay energy and nucleon separation energy of the daughter are graphed for each element (Z) as a function of 'neutron richness' (N-Z).

With the availability of more isotopes for decay studies, higher production rates and improved and innovative measurement techniques, new decay phenomena and un-expected variances with theoretical models will be discovered as the study of nuclei far from stability continues. One area of particular growth will be the observation and understanding of delayed multi-particle emission. The probability of observing such processes rapidly increases farther from stability. The case of the decay of ^{19}B is illustrated in Figure 1.3, where the beta decay energies and neutron decay thresholds in Mass 19 are shown. Here, up to <u>seven</u> neutrons can be emitted following the beta decay of ^{19}B.

In other fields of nuclear physics, the breakup of light systems is studied as they are emitted from hot nuclear sources. Table 1.1 gives some examples of high energy beta decays which can provide between 1 and 2 MeV of excitation energy <u>per nucleon</u> in the daughter. The associated nuclear temperature T which one might assign to this excitation energy per nucleon from a simple Fermi gas model is given by,

$$T = \sqrt{a\, E_x/A} \quad . \qquad [1.1]$$

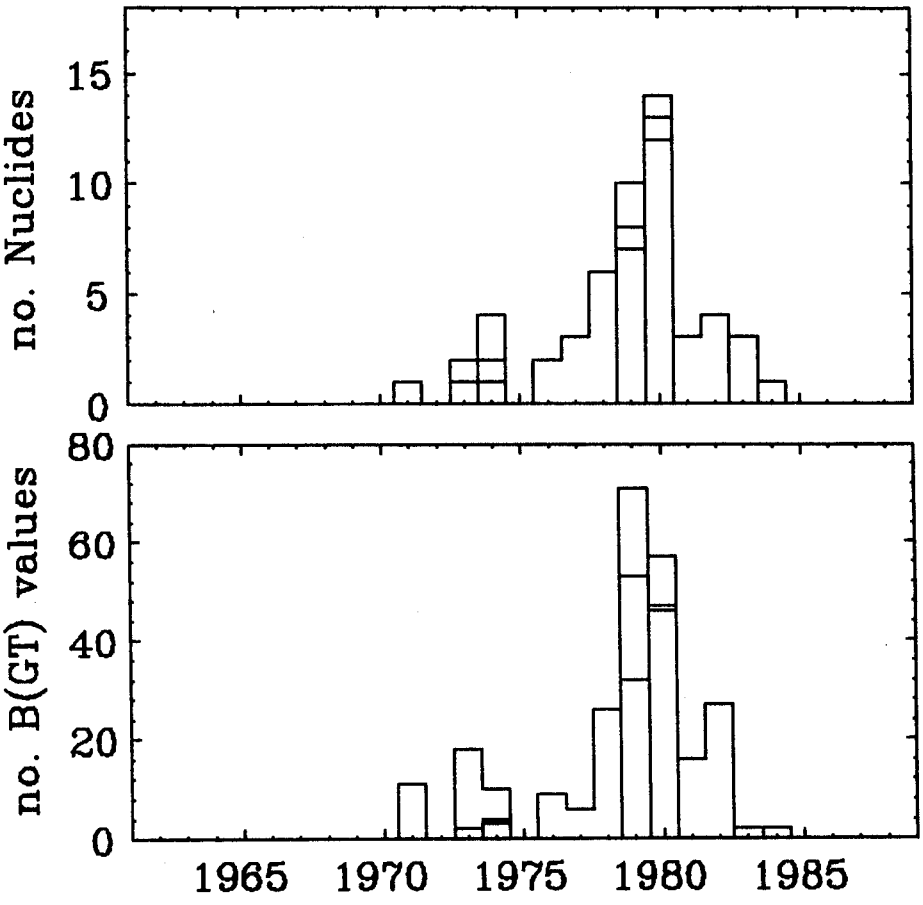

Figure 1.1 Year of publication for the data used in the compilation of BROWN85.

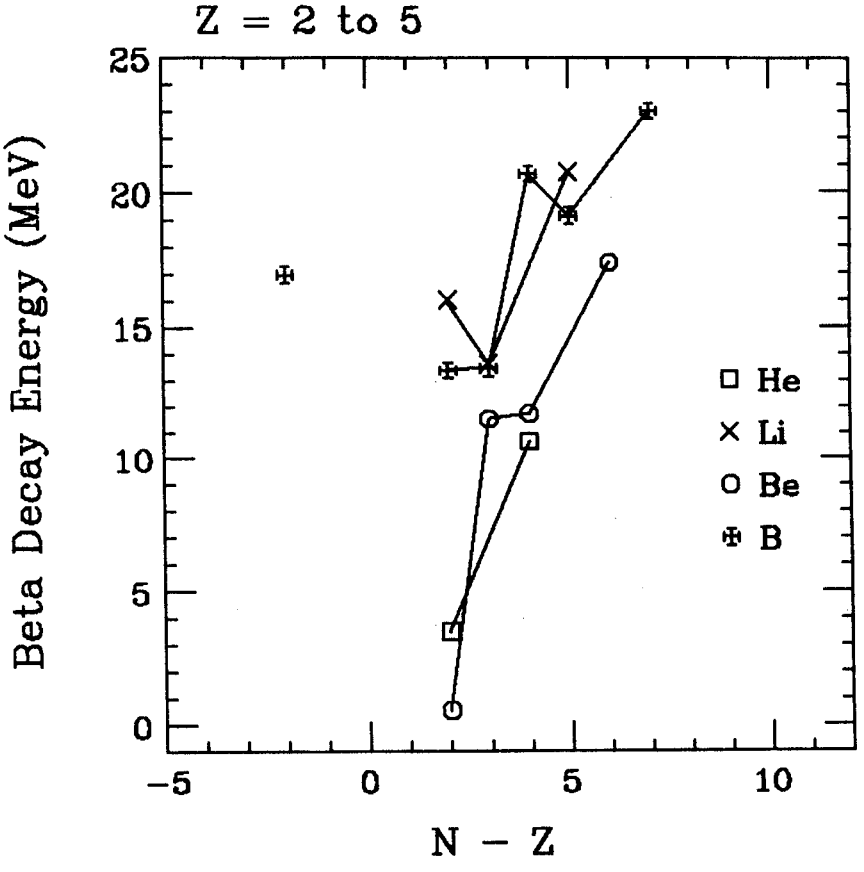

Figure 1.2 Trends in beta decay energies and nucleon decay thresholds of daughters. In both cases data are plotted for N-Z of the parent. Graphs are arranged with beta decay energies and nucleon separation energies on alternate pages so that one can look through two consecutive pages into a source of light and visualize the relationship to distance from stability.

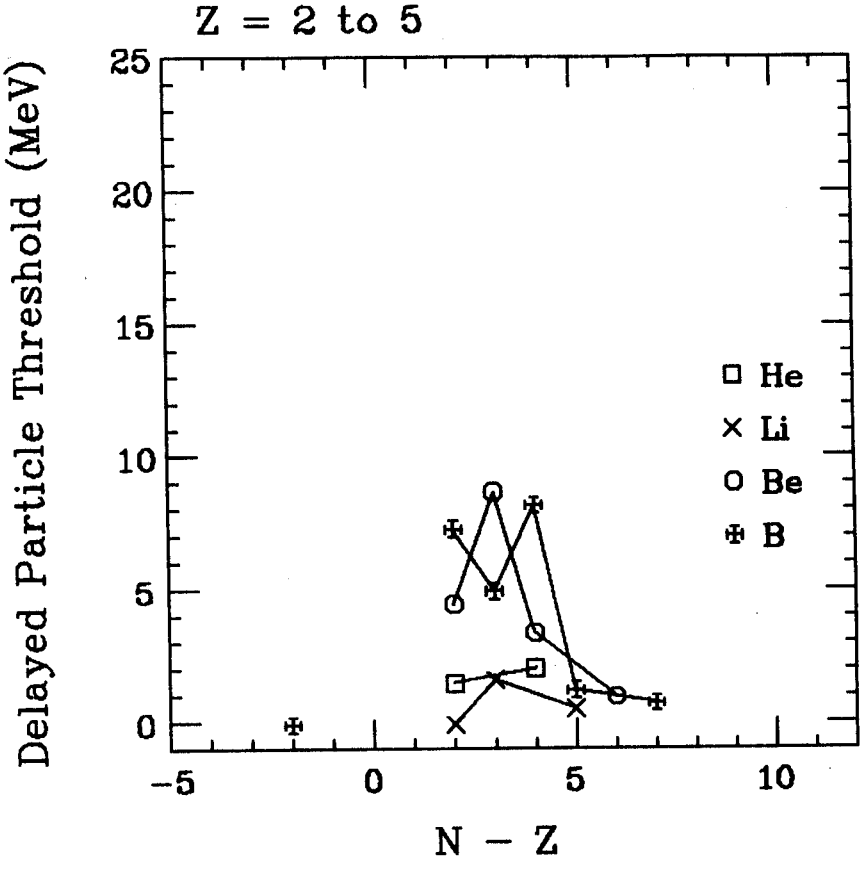

Figure 1.2 (continued)

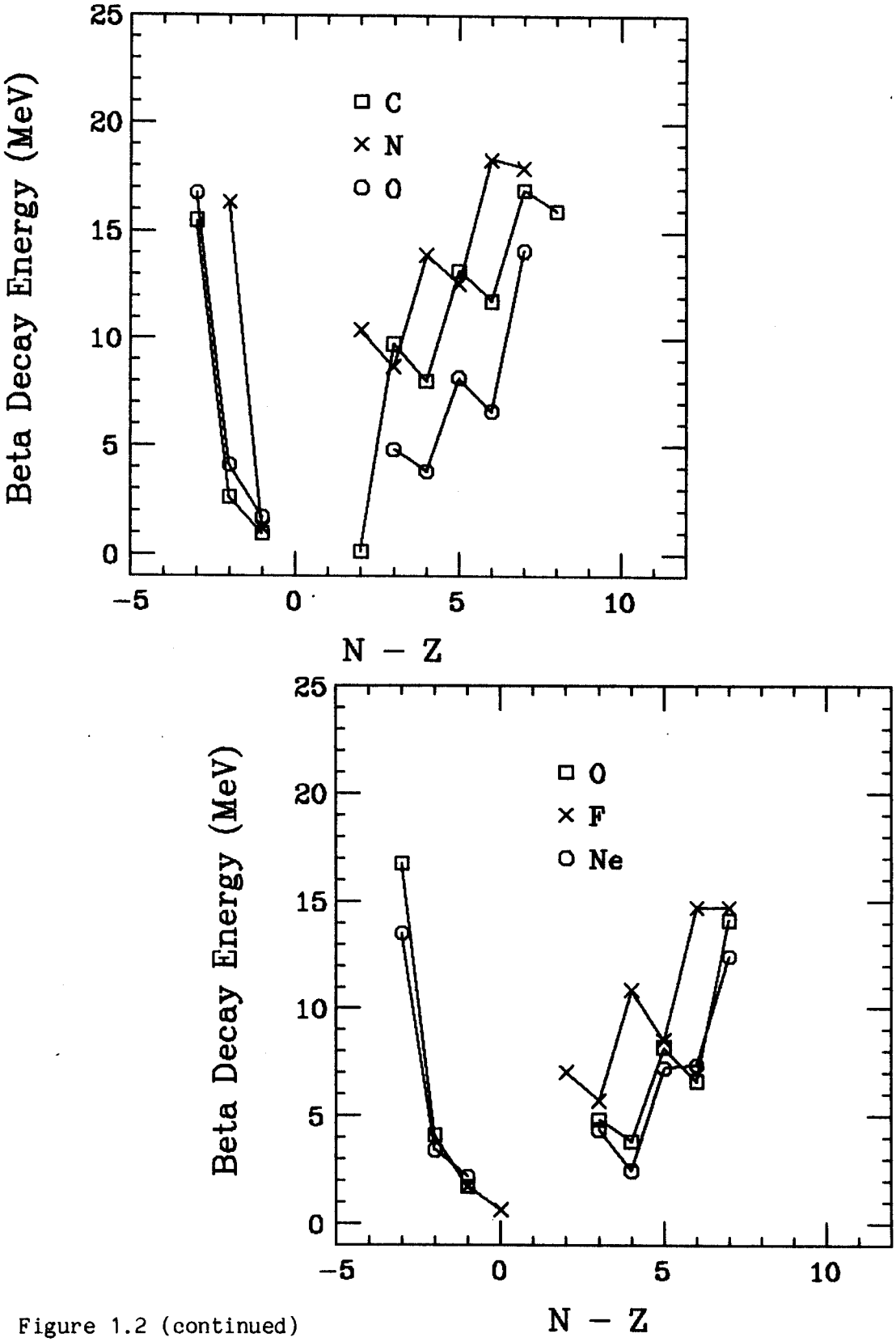

Figure 1.2 (continued)

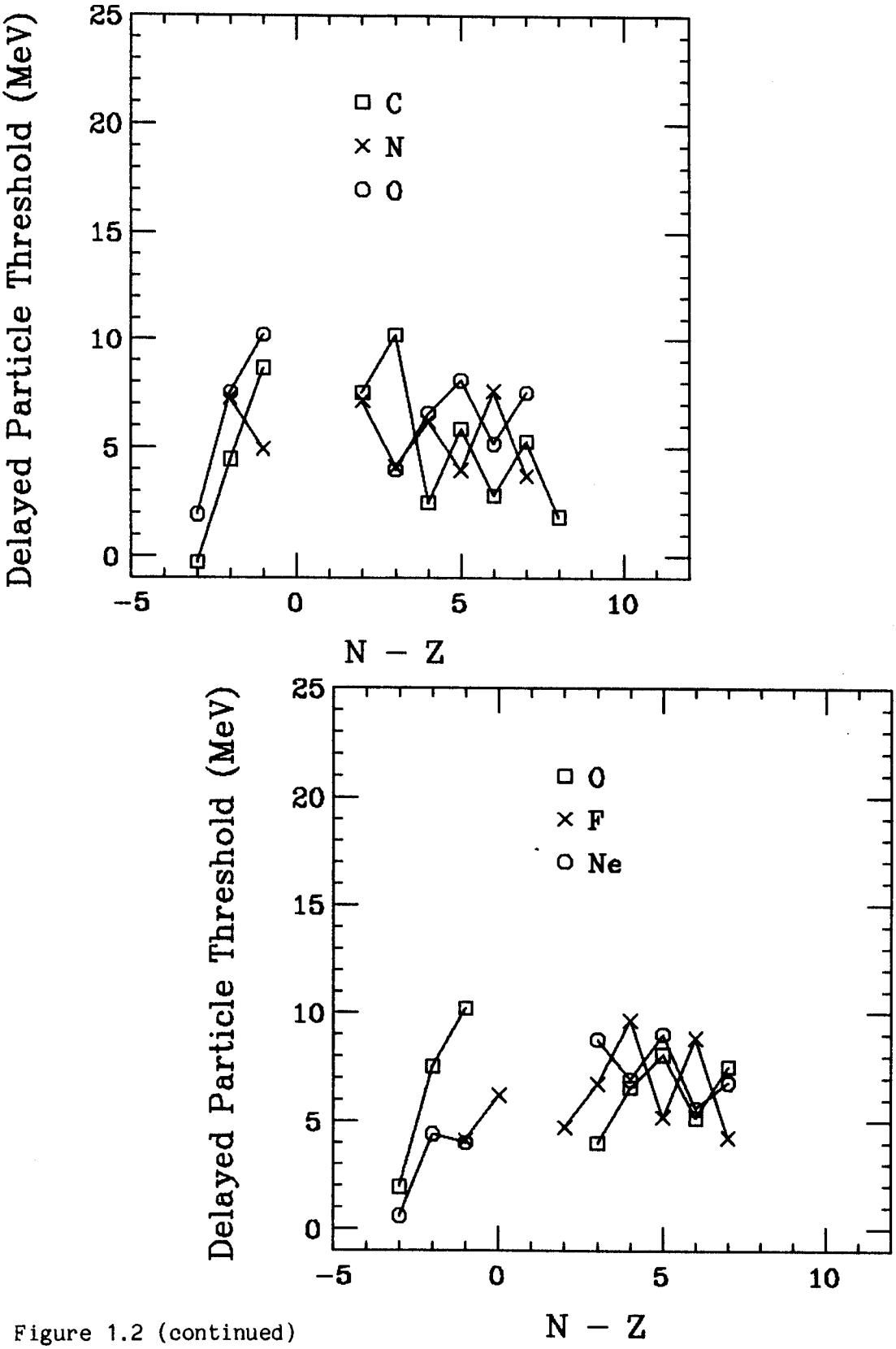

Figure 1.2 (continued)

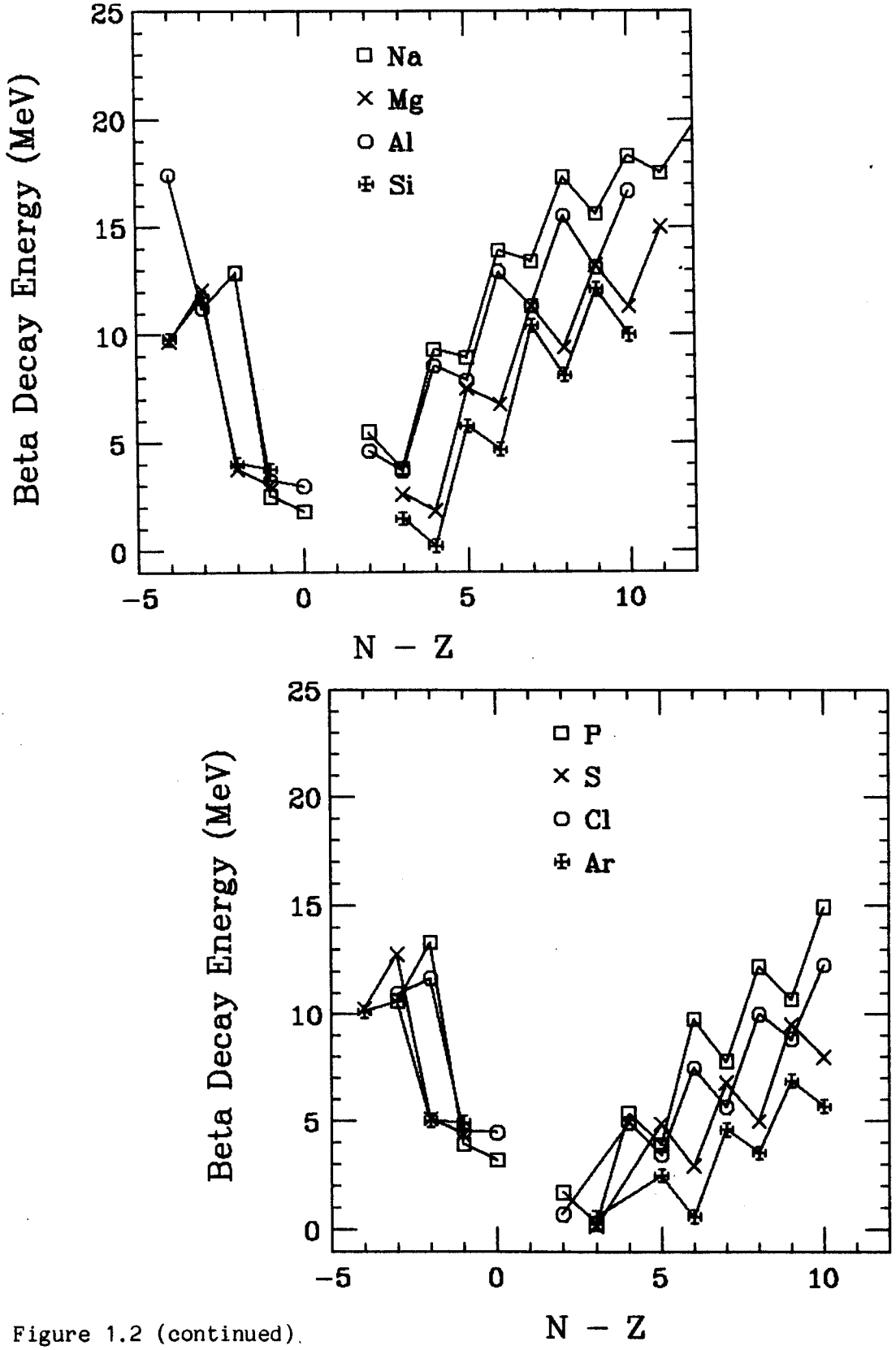

Figure 1.2 (continued).

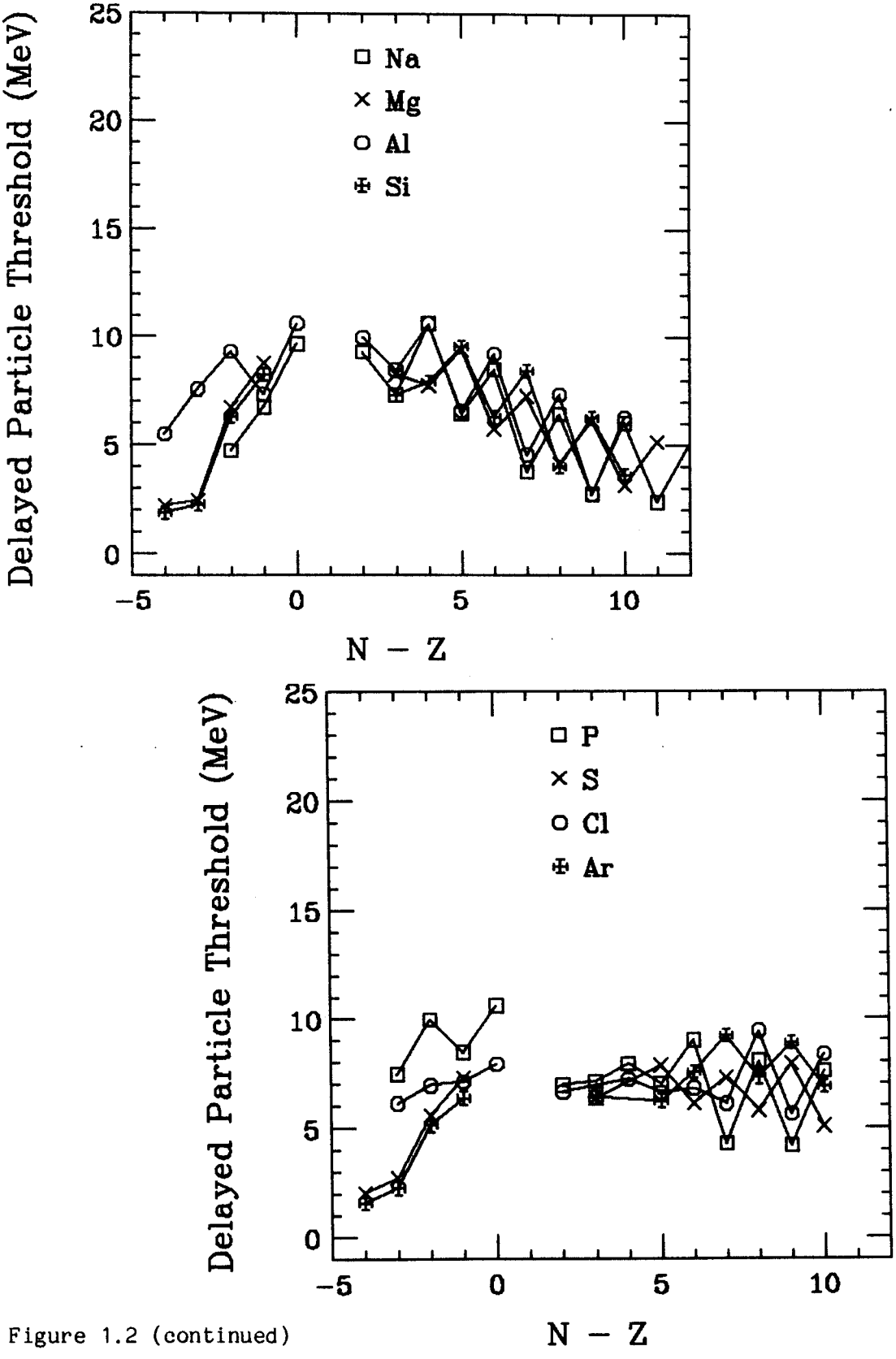

Figure 1.2 (continued)

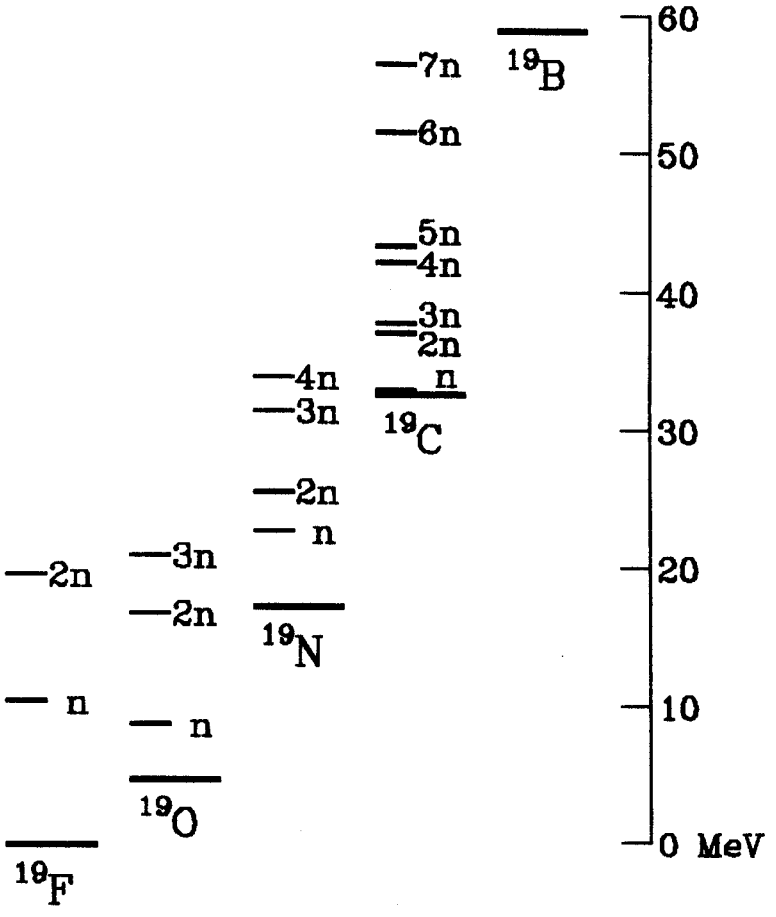

Figure 1.3 Beta decay energies and neutron decay thresholds in Mass 19.

Table 1.1 Some maximum excitation energies and inferred temperatures following beta decay.

Parent Isotope	Daughter Isotope	Maximum E_x (MeV)	Maximum Inferred Temperature (MeV)
^{8}He	^{8}Li	10.65	3.3
^{8}Li	^{8}Be	16.00	4.0
^{8}B	^{8}Be	16.96	4.1
^{9}Li	^{9}Be	13.61	3.5
^{9}C	^{9}B	15.48	3.7
^{11}Li	^{11}Be	20.73	3.9
^{11}Be	^{11}B	11.51	2.9
^{12}Be	^{12}B	11.71	2.8
^{12}B	^{12}C	13.37	3.0
^{12}N	^{12}C	16.32	3.3
^{13}O	^{13}N	16.74	3.2
^{14}Be	^{14}B	17.36	3.1
^{14}B	^{14}C	20.64	3.4
^{15}B	^{15}C	19.10	3.2
^{17}B	^{17}C	22.98	3.3
^{19}B	^{19}C	26.	3.3
^{22}Al	^{22}Mg	17.41	2.5

The level density parameter a is set to 8 MeV in this case (from NAYAK88).

A great deal of research is presently underway at NSCL and other laboratories to infer the conditions which occur in a heavy ion reaction from the break-up of light nuclei emitted from the reaction environment. The observation of the breakup of these nuclear systems in the 'clean environment' of beta decay (no nuclear spectators or contamination from other processes when beam strikes target) may improve our understanding of such processes, and may indeed yield important spectroscopic information not easily obtainable in any other way.

Some beta delayed particle decay channels will be quite complex, or compete with two or more other particle decay channels. In Figure 1.4 the beta delayed particle decay channels for ^{22}Al are shown. In Appendix B maximum beta decay energies and particle decay thresholds for all energetically accessable channels are tabulated for nuclei with protons and neutrons in the 0p and 0s1d shells.

While it will become more difficult to extract detailed structure information from delayed particle distributions as the decay process becomes more complex (more particle decay channels and greater multiplicities), the large number of isotopes which will be available for study in the future will make these types of investigations very attractive and productive. Projectile fragmentation will be a predominant source of unstable nuclei for nuclear structure studies. However the study of the decay properties of projectile fragments beyond half-life is still in it's infancy. This reaction provides it's

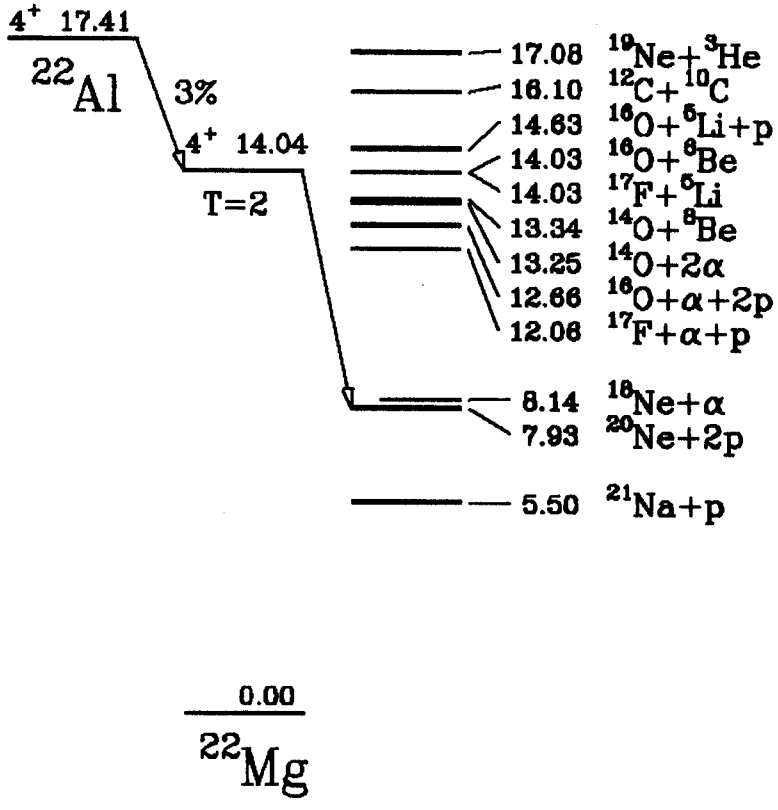

Figure 1.4 Beta delayed particle decay thresholds for ^{22}Al.

own advantages and disadvantages to the experimenter with a particular observable in mind. New techniques are presently being developed, and more will no doubt be necessary in the future to push the quantity and quality of nuclear structure information obtainable from nuclei far from stability to their limit.

This thesis is the result of a fusion between two goals. The first goal is to provide a discussion of a set of studies of the decay properties of a particular nucleus ^{9}C, which involved the development of a formalism with which to study the beta delayed multi particle final states and extract information which can be compared to shell model calculations. The second is an attempt to create a 'how to manual' for investigators interested in the study of the beta decay properties of nuclei produced by projectile fragmentation. This work is then naturally divided in two halves. The first half dealing with specific experiments, results, and comparisons to theoretical calculations. These are given in Sections II through IV. The second half is represented by the remaining sections, which contain detailed discussions of the various elements of an experiment and subsequent analysis which have been worked out over the years I have been at NSCL.

In section II, the standard formalism for connecting 'observables' such as beta decay half-life and branching ratio with 'calculables' such as nuclear wave functions, beta decay operators, and phase space factors for the beta-neutrino pair are presented. In section III, this connection is rederived for the situation where the final state is unbound. While various approximations are made, a system is developed to make preliminary interpretation of beta-delayed breakup spectra, even

in the extreme case where the nucleus 'breaks-up' into three or more parts.

In section IV, these models are applied to data from a recent experiment on the decay of ^{9}C. The experiment its self is described in MIKOLAS88a, which has been included here as Appendix 1. A summary of the information gained from the study of the beta-delayed three body final state of ^{9}C is given in section IV.3

The remaining sections of this thesis are devoted to the various experimental and analytical techniques which have been developed in order to record the 'observables' with enough precision in order to begin to address the phenomena discussed in sections II through IV.

The Conclusion section summarizes what has been learned about the decay of nuclei far from stability, and how this differs from experience to date on those nuclei closer to stability. The final Recommendations section suggests what new work, both theoretically and experimentally must be carried out in order to address these issues in more precise and calculable ways in the future.

SECTION II

II. Beta Decay to Bound States:

The rate of beta decay of a nucleus can be calculated in terms of a factor representing available phase space, and an overlap of the final and initial nuclear wave functions including the appropriate operators and coupling constants. The necessary overlaps and operators are briefly discussed in Section II.1, and the determination of lepton phase space is outlined in Section II.2. In Section II.3, the relationship between calculated quantities (such as B(GT) and lepton phase space) and measured quantities (such as half life and branching ratios) is derived for discrete final states. When states are unbound and broad, this derivation does not apply. That situation is discussed further in Section III.

Empirical values for the coupling constants derived from measured nuclear beta decay rates are discussed in Section II.4. Finally, an observed reduction in some types of nuclear beta decays rates with respect to that of the free neutron (Gamow-Teller Quenching) is discussed in Section II.5.

Good discussions of all facets of beta decay can be found in many texts. KONOPINSKI66, SCHOPPER69, and MORITA73 are especially useful, with the latter text the most advanced of the three.

II.1 Transition Rates in Nuclear Beta Decay:

The original proposals of Fermi (FERMI33) and of Gamow and Teller (GAMOW36) have remained as the two known forms of allowed (see below) nuclear beta decay, and are referred to as Fermi and Gamow-Teller beta decay. Fermi first proposed that the electron and neutrino were emitted such that their spins (S=1/2) were anti-parallel and thus

coupled to S=0. (The neutrino was postulated at that time by PAULI33, but had not been observed until much later by REINES60.) Thus since the two leptons couple to spin 0, no change in the spin of the nucleon or nucleus results. In a simple model for the structure of the nucleon, Fermi beta decay is just the change in identity of one of the quarks within the nucleon, such that [uud] <-> [udd] (i.e. proton <-> neutron), while the spin of the quark remains unchanged (VENTO84). It then follows that the spin of the whole nucleon is unchanged, as is the isospin and spatial wave function including parity. The change in the quark results in a change in T_z, and thus only the charge of the nucleus is altered in Fermi beta decay. Pure Fermi decay will then only connect two states of practically identical wave functions in all respects except for T_z, the charge. There is only one such state in the daughter nucleus, called the analog state. All of the Fermi strength is directed toward this state where isospin is a good quantum number for the states involved.

Fermi decay could explain only a fraction of the known beta decays. The Gamow-Teller theory of beta decay could explain many more, by requiring the electron and neutrino couple to S=1. The spin of the quark and thus the nucleon must then flip, which allows the nucleon to mix with other spatial and isospin (but not other parity) configurations. The operator permits a change of up to one unit of spin and of isospin of the nucleus. Thus Gamow-Teller decay populates many levels in a nucleus, including but not limited to the analog state. The selection rules for Fermi and Gamow-Teller beta decay are as follows. Fermi: $\Delta T = 0$; $\Delta J^{\pi} = 0^{no}$, Gamow-Teller: $\Delta T = 1,0,-1$; $\Delta J^{\pi} = 1,0,-1^{n}$,

(except $0^+ \rightarrow 0^+$). At low excitation energy in the daughter where the phase space for beta decay is large, most of the levels have the same isospin as the ground state. Since this is of course one unit different from that of the parent nucleus, the half life of a nucleus is predominantly determined by Gamow-Teller decay.

Both Fermi and Gamow-Teller are called allowed beta decay because the orbital angular momentum of both emitted leptons is 0. Forbidden beta decay is more complex of a process than allowed decay to accurately calculate, since the leptons must carry angular momentum. The small mass of the leptons requires them to be emitted at a great distance from the nucleus in order to carry one or more quanta of angular momentum, and this results in a strong inhibition of decays where $\Delta\ell \geq 1$. Thus the name forbidden decay. The degree of forbiddeness is defined as the number of orbital angular momentum quanta which must be carried by the leptons. Thus $\Delta\ell = 1$ is first forbidden, $\Delta\ell = 2$ is second forbidden, etc. Forbidden decays provide a mechanism to connect states of different Parity not connected by allowed beta decay processes (viz. $\Delta\pi=(-1)^{\Delta\ell}$. Thus $3/2^- \rightarrow 1/2^+$ can proceed through first forbidden decay and $5/2^+ \rightarrow 1/2^+$ through second since $\Delta\ell \geq 1$ and $\Delta\pi$ = no. $5/2^- \rightarrow 1/2^+$ may proceed by first forbidden decay, since $\Delta\ell = 1$ and $\Delta\pi$ = yes (the electron neutrino pair are coupled to J = 1.)

Allowed beta decay rates can be calculated to a very good approximation by the simple application of Fermi's Golden Rule,

$$\lambda_j = \frac{2}{\hbar} \rho(k) \, |\langle \psi_j | O | \psi_i \rangle|^2 \, . \qquad [2.1]$$

The two allowed beta decay operators, Fermi and Gamow-Teller, will have different intrinsic strengths independent of spatial overlap.

These have been parameterized as g_A and g_V, the Axial-Vector and Vector coupling constants, respectively, which represent the strength of the Fermi and Gamow-Teller (τ and $\sigma\tau$) operators. With these coupling constants and all other coefficients included, the beta decay rate can be expressed as

$$\lambda_j = C\, f_A(W_o,Z)\, [\delta_V g_V^2 |\langle\psi_j|\tau|\psi_i\rangle|^2 + Q_{GT} g_A^2 |\langle\psi_j|\sigma\tau|\psi_i\rangle|^2], \qquad [2.2]$$

where,

$$C = \frac{(\hbar c)^7}{c\,(m_o c^2)^5}, \qquad [2.3]$$

Here f_A is the dimensionless phase space factor evaluated specifically for Gamow-Teller decay, and δ_V (Equation 2.17) is f_V/f_A, a correction factor of order $1\pm\alpha$ ($\alpha \approx 1/137$) which represents the slight difference between the phase space factors for Fermi and Gamow-Teller decay. W_o represents the total decay energy, and is given in Equation (2.22). The evaluation of the phase space factor is discussed in more detail in Section II.2. Q_{GT} is an empirical quenching factor for the Gamow-Teller decay, and is discussed further in Section II.5. $m_o c^2$ is the energy equivalent of the rest mass of the electron.

The squares of the transition matrix elements for Fermi and Gamow-Teller (abbreviated as F and GT respectively) are traditionally expressed as the dimensionless quantities,

$$B(F) = |\langle\psi_j|\tau|\psi_i\rangle|^2,$$
$$B(GT) = (g_A/g_V)^2\, |\langle\psi_j|\sigma\tau|\psi_i\rangle|^2. \qquad [2.4]$$

The formalisms used in the evaluation of the matrix elements are described by BROWN85, and in references therein such as MAYERS55.

The nuclear beta decay rate becomes,

$$\lambda_j = C\, g_V^2\, f_A(W_o,Z)\, [\delta_V B(F) + Q_{GT} B(GT)], \qquad [2.5]$$

With C explicitly evaluated, and a value for g_V^2 obtained as described in Section II.4, the expression for the decay rate becomes,

$$\lambda_j = \frac{\ln(2)}{6170\pm4}\, f_A(W_o,Z)\, [\delta_V B(F) + Q_{GT} B(GT)]\ \ s^{-1}, \qquad [2.6]$$

The factor of ln(2) comes from the traditional discussion of the half life of a nucleus rather than the decay rate. This is discussed more in Section II.3.

II.2 lepton Phase Space:

The present theory of the Electroweak interaction states that the process of nuclear beta decay is actually a sequential pair of two body decays. Thus for β^- decay of a nucleus (A,Z),

$$(A,Z) \rightarrow (A,Z+1) + W^-,$$
$$W^- \rightarrow e^- + \bar{\nu}. \qquad [2.7]$$

The mass of the W boson has recently been measured to be roughly 90 GeV (ARNISON83 and BANNER83; see also WATKINS86 for casual reading.) This is four or five orders of magnitude more massive than typical nuclear beta decay energies. Thus the W is created in a virtual state, and lasts such a short time that one does not need to consider it as an independent particle in the kinematics. The available phase space can therefore be calculated by the simple approximation of direct three body decay (daughter nucleus and two leptons). Since the mass of the nucleus is much greater than that of the leptons, the approximation can be made that all of the kinetic energy is carried by the leptons. The available phase space is the proportional to

$$\rho = \int p_e^2 dp_e d\Omega_e\ p_\nu^2 dp_\nu d\Omega_\nu, \qquad [2.8]$$

with the appropriate delta functions inserted. The solution of Equation 2.8 can be found in any introductory text on beta decay, such as those mentioned in the beginning of Section II or MARMIER60. The result is a dimensionless phase space factor for the lepton pair in the absence of any Coulomb effects upon the electron,

$$f(W_o,Z=0) = \int_1^{W_o} pW(W_o-W)^2\,dW$$
$$= \frac{1}{60}(2W_o^4-9W_o^2-8)p_o + \frac{1}{4}W_o\ln(W_o+p_o) \quad . \qquad [2.9]$$

Here W_o is the total decay energy of the two leptons (including their rest mass) divided by m^oc^2, W is the total energy of just the electron, and,

$$p = (W^2-1)^{1/2} \quad . \qquad [2.10]$$

The calculation of the total decay energy W_o is discussed in Section II.3, and given explicitly in Equation 2.22.

The effect of the Coulomb field on the accessible states in phase space is significant at all energies, and can have orders of magnitude effects for heavy, highly charged nuclei. The effect can be approximated by simply multiplying the phase space factor for Z=0 by the ratio of the squares of the amplitudes of electron wave functions at infinity, to that at the nucleus. Thus,

$$f(W_o,Z) = f(W_o,Z=0)\,\frac{|\langle\psi(\infty)\rangle|^2}{|\langle\psi(R)\rangle|^2} \qquad [2.11]$$

where ψ is the electron wave function from the solution of the Schrödinger or Dirac equations in the nuclear Coulomb potential. The radius R must be chosen carefully for an accurate determination of the phase space calculation. The finite size and internal structure of the nucleus would require, for a complete solution, the phase space factor

to be weighed by the expectation value of the beta decay transition as a function of R. This however is most likely inordinately rigorous for most applications, and usually one assumes the weight to be uniformly distributed over the volume of the nucleus. This subject has been approached in light nuclei by TOWNER73b and WILKINSON74.

The Coulomb correction has been extensively calculate by Wilkinson and Macefield (WILKINSON74), where the ratio of the squares of the amplitudes in Equation 2.11 for the solution of the Dirac equation is evaluated for a uniformly charged nucleus as a uniform source of leptons. The Coulomb field is corrected for the screening of the atomic electrons, such that the field does not have a strict r^{-2} dependence, but instead drops to zero at a finite distance. A 'radiative' correction is evaluated, taking into account a type of bremsstrahlung radiation as the electron suddenly leaves the nucleus, and the charge distribution within the nucleus is re-arranged. This process can involve both the production of real photons, and emission and reabsorbtion of virtual photons. It has been evaluated to order α in WILKINSON74. The various types of radiative corrections are discussed in detail in SCHOPPER69. Corrections for the finite mass of both the nucleon and the nucleus are also included. The overall correction factor is expressed as an analytic function of beta energy of four coefficients. This correction, termed δ_{WM} after the authors, (in keeping with the notation of BROWN85) is given as,

$$\delta_{WM} = \exp\Big[\sum_{n=0,3} a_n \big(\ln(E_0)^n\big) \Big] , \qquad [2.12]$$

where the coefficients a_n are those given in tabular form in WILKINSON74. E_0 is the maximum kinetic energy of the beta, such that

$$E_o = (W_o-1)m_oc^2 \quad . \qquad [2.13]$$

Wilkinson and Macefield state that the correction δ_{WM}, applied to Equation 2.6 will provide f_A (see below) to an accuracy better than 0.1% for electron endpoint energies E_o from 10 keV to 20 MeV, and for Z=1 to 101.

Brown also includes two more correction factors. The first is an additional radiative correction to orders $Z\alpha^2$ and $Z^2\alpha^3$, as described in WILKINSON73, 74, and is given as,

$$\delta_R = 1 + 3.67\times10^{-4}Z + 3.60\times10^{-6}Z^2 \quad . \qquad [2.14]$$

The second correction in BROWN85 allows for the 'diffuseness' of the nuclear charge distribution (δ_{WM} is calculated for a hard sphere), and is discussed in WILKINSON78. It is given as,

$$\delta_D = 1 + 1.8\times10^{-5}Z^{1.36} - 1.2\times10^{-6}ZW_o. \qquad [2.15]$$

The differences in the mechanisms of Fermi and Gamow-Teller beta decay require slightly different choices of R, and involve slightly different forms of some of the other corrections. This is discussed in detail in WILKINSON74. The phase space factor for Gamow-Teller decay f_A is first calculated,

$$f_A(W_o,Z) = \delta_D\delta_R\delta_{WM}f(W_o,Z=0) \quad . \qquad [2.16]$$

The factor f_V is then obtained for $e^{\pm}$ decay by a small correction factor δ_V,

$$\delta_V = 1 \pm \left(\frac{2}{15}\right)\left(\frac{W_oR}{197}\right)\alpha Z - \left(\frac{4}{105}\right)\left(\frac{W_oR}{197}\right)^2 \quad , \qquad [2.17]$$

such that,

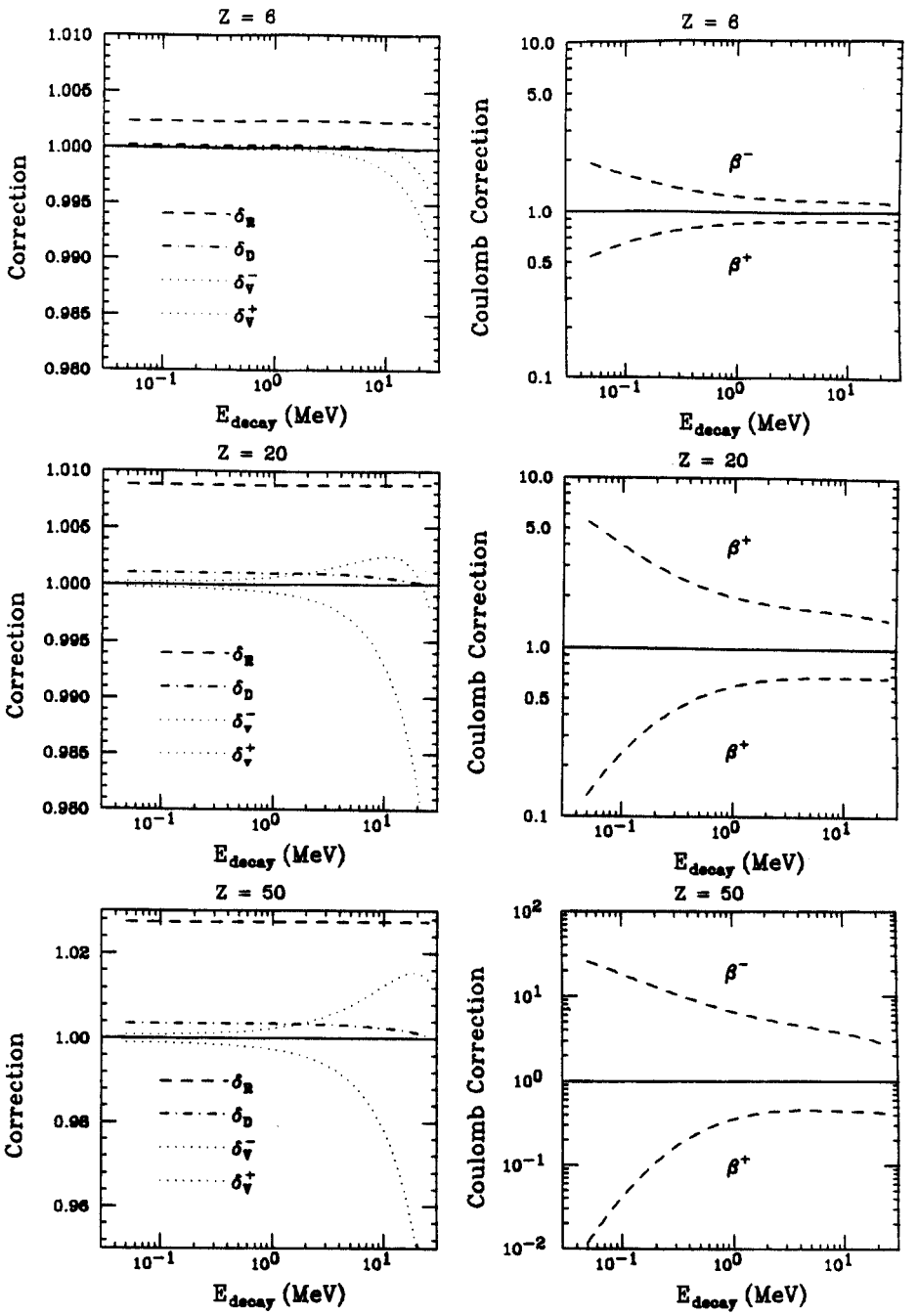

Figure 2.1. The behavior of various expressions related to nuclear beta decay rates as a function of beta decay energy for three values of Z for the daughter. See text for complete discussion.

$$f_V(W_o,Z) = \delta_V f_A(W_o,Z) \ . \qquad [2.18]$$

In Figure 2.1 the behavior and magnitudes for various expressions above are illustrated as a function of beta decay energy. They are evaluated for a daughter Z of 6, 20 and 50.

Further discussion of lepton phase space can be found in any of the texts listed in the beginning of this section. The subject is comprehensively, exhaustively and rigorously examined by BEHRENS82.

In the future, as beta decay rates are determined for isotopes further from stability, a re-evaluation of the phase space correction factors will become necessary. The corrections listed above are all given as only a function of Z. Implicit in the numerical coefficients are evaluations for the most stable A. The gentle rise in the mass surface on the neutron rich side provides a large range in N which are particle stable, for a given Z. n For example, it may be possible to compare such isotopes as ^{35}Ca and ^{70}Ca. Here the nuclear mass changes by a factor of 2. and the radius by 26%, while the nuclear charge remains constant. Further, the diffuseness will be different for neutron rich, near stability and neutron deficient nuclei.

Further corrections are necessary, but become increasingly complex. In a review article on the subject, HOLSTEIN74 reviews a set of corrections collectively referred to as 'recoil effects.' Briefly, the finite mass of the nucleon and thus nucleus with respect to the decay energy implies that the recoil momentum of the nucleon/nucleus must be explicitly considered. In an interesting discussion on beta decay, SAMSONENKO89 discuss the importance of treating the mesons within the nucleus in the beta decay process.

II.3 Branching Ratios and Half Lives:

The principal quantities which one can directly calculate in allowed nuclear beta decay are the decay matrix elements B(GT) and B(F), and their corresponding phase space factors $f_A(W_o,Z)$ and $f_V(W_o,Z)$. However, the observables in beta decay are usually the overall half-life (t) of a nucleus and branching ratios (BR) to well defined discrete final states, such that,

$$\sum_j BR_j = 1. \qquad [2.19]$$

The decay rate is related to the half-life by,

$$\lambda = \frac{\ln(2)}{t}. \qquad [2.20]$$

For each excited state j, a partial half life t_j can be defined in terms of the total half life t and branching ratio as,

$$t_j = \frac{\ln(2)}{\lambda_j} = \frac{t}{BR_j}. \qquad [2.21]$$

The phase space factor is a function of the decay energy of the i^{th} state to the j^{th} state. Q_B is defined as the difference between the atomic mass excess of the ground state of the parent nucleus, and that of the daughter. The atomic mass excess of a nuclear state represents the difference between the mass of the atom (the nucleus in that state plus Z electrons bound in their atomic ground state) and A/12 times the mass of a neutral atom of ^{12}C.

Many subtleties exist in the details of the energy differences when the beta decay of ions or fully stripped atoms are dealt with in beta decay in astrophysical environment, or in storage rings such as the SIS/ESR project underway at GSI in Darmstadt. The change in binding energies of each of the electrons as the nuclear charge is changed must be taken into account, as well as decay rate to competing

processes. One such process is the beta decay to bound electronic states such that the electron is captured into an un-occupied atomic orbital.

For most beta decay experimental situations, the parent nucleus is at rest, imbedded in matter so that it is a neutral atom. In this case, the decay energies for e^- and e^+ beta decay are just,

$$W_{o_-} = Q_\beta + (Ex_i - Ex_j) ,$$
$$W_{o_+} = (Q_\beta - 2m_o c^2) + (Ex_i - Ex_j) . \qquad [2.22]$$

In light nuclei, Ex_i is usually 0 for states whose beta decay can be observed. The low spins and large level separations of light nuclei discourage isomeric levels with half-lives long enough to compete with photon emission. However, occasional isomeric states do occur, and the beta decay rate from levels such as ^{16}N ($J\pi=0^-$, $t\approx5\mu s$?) have been measured (GAGLIARDI83, MINAMISONO83, HAMEL85 and HEATH85). Isomeric states with much longer half lives are found in isotopes of Na and Al.

The symbol ft has been agreed upon as a simple way to express the strength of a given measured decay rate. It is defined such that,

$$ft = f_A(W_o,Z)\, t_j . \qquad [2.23]$$

The combination of Equations 2.6, 2.21, and 2.23 yields the relationship,

$$ft \left[\delta_V B(F) + Q_{GT} B(GT)\right] = 6170\pm4 \text{ s} . \qquad [2.24]$$

Often, ft values are reported as their logarithm in base 10. Thus the symbol log(ft) is most often reported. Values of log(ft) from 3.3 to 6 are typical for GT beta decay.

II.4 Empirical Coupling Constants:

The vector coupling constant g_V can been empirically determined from the analysis of the decay rates of many nuclear $0^+ \rightarrow 0^+$ transitions, where only Fermi decay contributes. In these cases, both the matrix elements B(F) and the phase space factors f_V can be calculated very precisely, and thus the observed decay rates are presumed to be accurate determinations of the coupling constant g_V. Such an analysis is discussed in WILKINSON78a, and it is the results of this analysis which is incorporated into the numerical coefficient of Equation 2.6. A current summary of experimental and theoretical work associated with $0^+ \rightarrow 0^+$ nuclear transitions and their relationship to more fundamental concepts has been compiled by HARDY89.

While the beta decay of the free nucleon (neutron) seems the most fundamental source of beta decay information, it is useful only after a value for g_V has been obtained since the neutron can undergo both Fermi and Gamow-Teller beta decay. The ratio $(g_A/g_V)^2$ can be estimated as follows.

The accepted half life of the neutron is presently 10.6 minutes. See FREEDMAN85, FREEDMAN86. With a Q_β of 0.7823 MeV (WAPSTRA86), the phase space factor for both Fermi and Gamow-Teller transitions is 1.637. The B(F) for a free nucleon is 1, and $|\langle\sigma\tau\rangle|$ is 3 for the free nucleon. The ratio (g_A/g_V) can be determined from Equation 2.24, with the quenching factor Q_{GT} explicitly set to unity for neutron decay (see Section II.5). Thus,

$$(1.637)(636.)\left[1+3(g_A/g_V)^2\right] = 6170, \qquad [2.25]$$

which gives,

$$(g_A/g_V) = 1.28 \ . \qquad [2.26]$$

This is close to the value of 1.251(9) of WILKINSON73, which has been adopted by BROWN85, and the newer value of 1.2606(75) of WILKINSON78. See also FREEDMAN85 and FREEDMAN86.

II.5 Gamow-Teller Quenching:

The strength of the Vector coupling constant g_V has been empirically determined from a set of carefully chosen and measured $0^+ \rightarrow 0^+$ nuclear beta decays, and the Axial-Vector coupling constant g_A has been evaluated for the case of the free neutron where the strength is all to one final state. Nuclei with more than a single nucleon can not be used in determinations of the coupling constants. This is because unlike Fermi decay, Gamow-Teller connects an initial nuclear state with many final states, and all of the Gamow-Teller strength to these final states must be summed up in order to calculate g_A. This is usually impossible, since many of the final states sharing the Gamow-Teller strength lie above Q_β, and thus can not be populated by beta decay. Thus g_A is ultimately obtained from the neutron decay half-life alone, and the value thus obtained is called the free nucleon value.

A careful study of hundreds of experimentally determined ft values and M1 gamma ray decay rates for nuclei in the sd shell was carried out by BROWN85. A clear trend in the predicted versus measured ft values was observed. The experimental ft values were consistently larger than the predicted values. The theory could be brought into agreement with the experimental values when a quenching factor Q_{GT} of 0.6 was introduced. This Gamow-Teller quenching has been the subject of many investigations. It at first appears that the nucleon somehow changes

in the nuclear environment, such that the g_A is reduced by a factor $0.6^{1/2} \approx .77$ with respect to the free nucleon value!

However, it is now believed that a much simpler explanation exists, without requiring a renormalization of the Axial-Vector coupling constant. Most likely the quenching is actually an artifact of some of the simplifying assumptions in the shell model theory used to predict the B(GT) values. The Gamow-Teller strength has not disappeared, but instead is distributed over more levels than was previously thought. The present shell model configurations do not include enough degrees of freedom to predict all of these states, and thus assign extra strength to the states which it does predict. Calculations using larger model spaces will be useful (if difficult and time consuming) in order to confirm the presence of the missing strength in higher lying levels.

A second source of quenching involves mixing of the predicted states with the Δ resonance, representing mesonic degrees of freedom not included in the shell model. BROWN87 estimates that roughly 2/3 of the quenching is a result of configuration mixing, and the other 1/3 is a result of mixing with the Δ resonance.

As discussed in the Introduction Section, Conclusions Section, and Recommendation Section, decay studies of nuclei far from stability might increase the information on Gamow-Teller quenching. This will be made possible by exploring Q_{GT} in nuclei with greatly different N/Z ratios and greater W_o than those which have been studied to date, where the behavior of the quenching might shed some light upon the underlying mechanism.

SECTION III

III. Beta Decay to Unbound States:

When the final state of a nuclear beta decay is unbound to still further decay modes such as nuclear particle emission, the connection between the beta decay matrix elements (e.g. B(GT), B(F)) and the observed decay rate becomes more complex than the relationship derived in Section II. This is primarily because the final state is now no longer discrete but is instead spread out in energy. In some cases states populated by beta decay are sufficiently excited to break up into three or more nuclear particles. In this situation the connection between the observed distribution in n-body phase space to the initial beta decay matrix elements is even more complex.

While the connection between observed and directly calculable quantities is complex and will continue to involve some approximations, it will become an increasingly popular problem as more and more information is gathered on the decay of exotic nuclei. Decay properties are the predominant source of information on the structure of nuclei when only thousands to millions of atoms of a particular isotope are available[2].

The determination of most of the B(GT) in the decay of nuclei very far from stability will involve the observation of delayed particle emission. The initial states are often close to being unbound and most

2. The only other piece of information which can be obtained from a sample of a thousand to a million nuclei is the ground-state mass. In the future, techniques involving high intensity lasers and storage techniques such as ionic traps or storage rings may be able to probe other ground state properties such as magnetic moment and RMS matter and charge radius of the nucleus when only a small number of nuclei are available.

of the final states are indeed unbound. There are two important complications which arise when the final state of a beta decay is unbound to particle emission; 1) the radial wave functions must somehow be modified since there is a finite expectation value for finding some part of the nucleus well beyond a radius inferred from a standard Harmonic Oscillator (HO) wavefunction, and 2) the problem becomes time dependant and thus the excitation energy of the state is no longer well defined.

III.1 Structure of Unbound and Loosely Bound levels:

The first point actually applies to levels which are loosely bound as well as those which are unbound. The most dramatic example of this might be found in ^{11}Li. This nucleus is believed to be bound to two neutron emission by only 197 ± 110 keV (WAPSTRA85). TANIHATA85a, b, TANIHATA88 and KOBAYASHI88 report a nuclear radius extracted from total reaction cross section measurements which is roughly 20% larger than that of its beta decay daughter ^{11}Be! If this is indeed a valid interpretation of the reaction crossection, it is the most dramatic example of variation of a nuclear radius with binding energy.

In most situations the radial wave functions will not show such a dramatic difference between parent and daughter. However, slight changes in the radial wave functions induced by changes in binding energy have been studied for many years. THOMAS51 and EHRMAN51 studied the coulomb energy shift of single particle levels which could be represented by a single nucleon and an N=Z core. The difference in mass between the mirror ground states represents the coulomb interaction of

the proton with the core, under the assumption that all other interactions are the same for the nucleon whether it is a neutron or proton. Because of the mutual Coulomb repulsion, the proton rich nucleus usually becomes unbound to particle decay first. Thus the radial wave function of the proton expands more rapidly than that of the neutron as a function of excitation energy, which in turn decreases the overlap of the proton's wave function with the core. This results in a smaller coulomb energy shift than that for the ground state, shifting the excitation energy of the proton-rich level less than that of the neutron-rich level. This shift is usually referred to as a Thomas-Ehrman shift[3]. It is experimentally observed as a lower excitation energy for a state (relative to the ground state) in the nucleus with a proton excess than the mirror state in the nucleus with a neutron excess.

Most wave functions needed to obtain B(GT) will not be of single particle nature, and thus binding energy effects can not be easily calculated. ORMAND85, 86, and 89 are developing an Isospin Non-Conserving (INC) Shell Model Hamiltonian which partially addresses this issue. Here binding energy effects will be indirectly represented as an Isospin dependence in the interaction which has the potential for some success because of the correlation between binding energy and the T_z of the nucleus.

3. A systematic study of shifts in mirror levels was carried out by NOLEN68. They found that a small fraction of the shift could not be accounted for by any known phenomena. No simple solutions have yet been found to explain the residual shift. This residual shift is often referred to as the Nolen-Schiffer anomaly.

A different approach was taken by TOWNER73 to calculate the effect of binding energy upon the wave functions of nuclei. Here, each state was expanded into a series of nucleon + A-1 configurations where excited states in the A-1 nucleus were included. The binding energy effects were calculated for each configuration. B(GT) were then calculated for mirror decays both to the same final state (such as ^{12}B, ^{12}N decay to ^{12}C) and to mirror final states (such as ^{13}O ->^{13}N, and ^{13}B->^{13}C.) The observed differences in the mirror B(GT) could usually be reproduced, serving the dual purpose of explaining the observed asymmetry in B(GT) and providing a way to incorporate binding energy effects into the wave functions of levels which could not be represented as single particle configurations.

III.2 Excitation Energy and Unbound Levels:

As pointed out above, unbound levels will have a finite width. This implies that the beta decay may populate the level at more than one energy. The beta decay rate must now take into account not only the density of states available to the beta neutrino pair in phase space, but the internal density of states of the final nucleus.

The internal density of states for the unbound system can be obtained from a Breit-Wigner parameterization of the line-shape. It can be derived in various forms from first order perturbation theory. A complete treatment of R-matrix theory can be found in LANE45. This representation has a wide range of application in resonant phenomena where an unbound state can remain static long enough so that its decay can be treated in first order perturbation theory.

One form often used to represent scattering states is

$$\rho(E)\, dE = \frac{\Gamma(E)/2\pi}{(\Gamma(E)/2)^2 + (E-E_0)^2}\, dE. \qquad [3.1]$$

Here the local width $\Gamma(E)$ represents the decay rate of the level at energy E. E_0 is often quoted as the excitation energy of the state, but actually is best described as the energy at which the phase shift would be 90° if the resonance were produced in a scattering situation with no other scattering processes interfering. When describing an observed state without a complete phase-shift analysis, it is simply an adjustable parameter which gives a best fit.

If the state is relatively narrow, such that $\Gamma(E)$ is nearly constant over the region $(E_0-\Gamma/2) \leq E \leq (E_0+\Gamma/2)$, then the full width at half-maximum (FWHM) of the distribution is just Γ. However this is true only when Γ is constant and thus the distribution symmetric. $\Gamma(E)$ actually represents the size of the transition matrix element for the decay of the state being described at each energy, and its ability to describe the FWHM of the line shape is true only in certain limits.

In the same fashion that the beta decay rate was obtained in Section II, the nuclear decay rate $\Gamma(E)$ can be expressed as the product of an overlap between initial and final states, and a phase space factor. However, one must keep in mind that the emission of a nuclear particle from a nucleus is a complex process, and only approximate tools exist for the treatment of such problems. The dynamics of how a complex particle and residual nucleus form out of a single initial nucleus, and of how they penetrate the nuclear potential barrier is a difficult and poorly understood topic, and will not be dealt with in detail here. The concept of a spectroscopic factor from shell model overlaps, and a penetrability from standard R-Matrix theory will be

used. The calculation of spectroscopic factors is discussed in Appendix A. (MIKOLAS88a).

The spectroscopic factor is usually expressed as a fraction of a Wigner single particle unit,

$$\gamma^2 = \frac{3}{2}\frac{(\hbar c)^2}{mR_0^2}, \qquad [3.2]$$

where μ is the reduced mass of the two products of the decay. The decay can often proceed through more than one angular momentum ℓ, so that a spectroscopic factor is usually expressed as θ_ℓ for each partial wave. If one or both particles have a non-zero spin, then a second quantum number, channel spin, must also be summed over. This will be ignored in the present derivation for simplicity.

The final state is actually the two nuclear particles separated at large distances. Thus the complete overlap of final and initial states includes the expectation value of finding the two particles at a separation r as $r\to\infty$. However, this factor is traditionally included in the penetrability factor discussed below.

The phase space factor is in fact obtained in a manner very similar to the phase space factor for beta decay. Here the Schrödinger equation is solved for relative angular momentum ℓ in the region $r>R_0$ for the relative kinetic energy of the decay channel of interest, giving the ratio of intensities of the wave function at $r=R_0$ and $r=\infty$.

Using the standard Wigner parameters ρ and η,

$$\rho = kr,$$

$$\eta = \frac{Z_1 Z_2 e^2}{\hbar c}, \qquad [3.3]$$

where,

$$k = \frac{\sqrt{2\mu E}}{v\hbar c}, \qquad [3.4]$$

velocity,

$$v = \sqrt{2E/\mu}, \qquad [3.5]$$

and E, the decay energy in the center of mass with μ as the reduced mass, the penetrability P_ℓ for a given decay into two spin-zero particles is,

$$P_\ell = \frac{\rho}{F_\ell^2(\rho,\eta) + G_\ell^2(\rho,\eta)}, \qquad [3.6]$$

where F and G are the regular and irregular coulomb wave functions, and can be obtained either from iterative computer programs (e.g. BARNETT82[4]) or from tables (e.g. MARION68 and SHARP55.) For neutron decay, η=0 and F and G reduce to Bessel functions.

The local width of the state is finally given as

$$\Gamma_\ell(E) = \frac{2\,\theta_\ell^2\,\gamma^2\,\rho}{F_\ell^2(\rho,\eta) + G_\ell^2(\rho,\eta)}, \qquad [3.7]$$

or in the more compact form

$$\Gamma(E) = 2\,\theta_\ell^2\,\gamma^2\,P_\ell(E). \qquad [3.8]$$

The state is often unbound to more than one value of ℓ, and sometimes to even more than one type of particle decay channel. In order

4. At low decay energies (below roughly 100 keV for light nuclei) the program discussed in this reference sometimes fails to converge in certain energy windows, while converging both below and above this window. An error message is returned to notify of such failure. Adjusting the constant ACCUR ($\approx 10^{-29}$) will move the window around enough to calculate any desired value. If extensive low-energy calculation is important, then this problem should be investigated more thoroughly.

to avoid the proliferation of indices, a 'master' equation will not be written down. Instead, the expression,

$$\Gamma(E) = \sum_i \sum_\ell \Gamma_{i\ell}(E_i), \qquad [3.9]$$

illustrates that the total decay rate is simply the sum of all of the partial decay rates into the partial waves ℓ and particle decay channel i.

In Figure 3.1, a level diagram of the beta delayed alpha decay from ^{11}Be is shown. The level in ^{11}B decays by the emission of an alpha particle to both the ground state and first excited state of ^{7}Li. This situation illustrates the use of Equation 3.9 in calculating the total decay rate as a sum of the partial decay rates.

One fact which becomes important in the comparison of beta decay rates to the beta decay matrix elements is the area of the Breit-Wigner distribution. For a constant Γ the area of Equation 3.1 is unity when integrated over the unlikely limits of $-\infty$ to ∞. However, if the penetrability is varying over the line shape under consideration, then the are is no longer normalized to unity. Figure 3.2 shows various line shapes for a hypothetical state in $^{8}Be_{gs}$ for different values of E_0. In Figure 3.3, the areas of these distribution are plotted as a function of E_0. Two important points can be extracted from this exercise. First, the areas can vary significantly from unity which has a direct effect upon the beta decay rates and thus half-life of a nucleus which populates this state. Secondly, the line shape may become so asymmetrical that a second maximum, or 'ghost' appears at higher excitation energy. Ghosts like this often appear near threshold, where the penetrability is varying exponentially and can

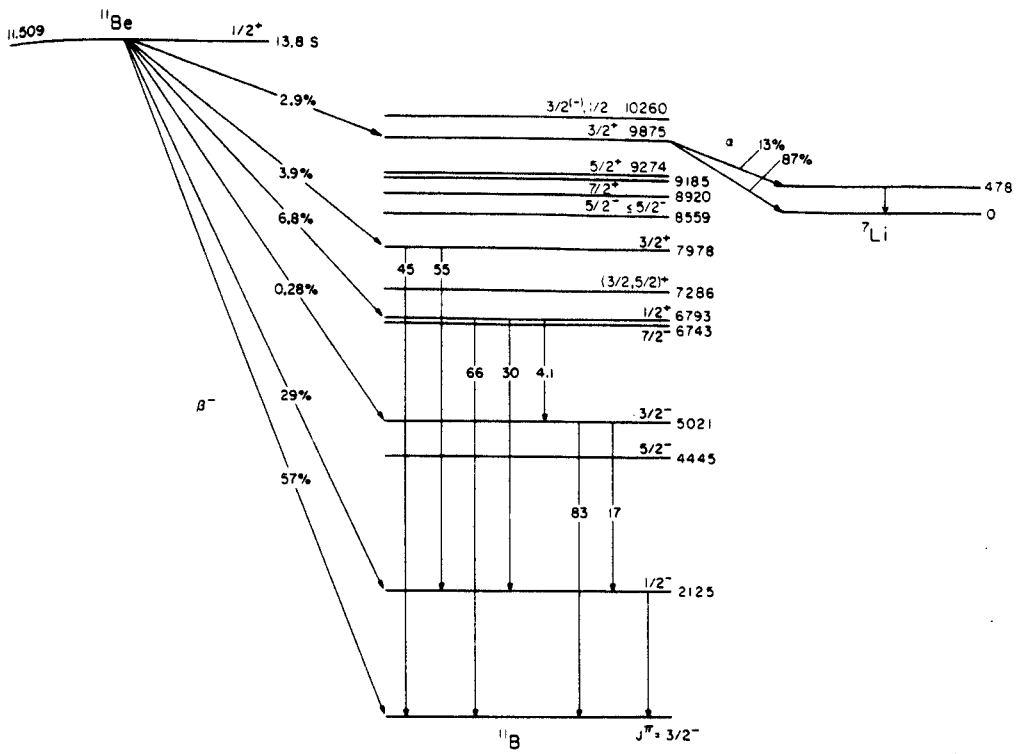

FIG. 4. Proposed decay scheme of ^{11}Be. New information from the present work includes the β-ray branching intensity to the 9875-keV state and α branching ratios to the ground and 478-keV states of ^{7}Li.

Figure 3.1 Energy level diagram for the beta delayed alpha emission of ^{11}Be. Branching ratios are from ALBURGER81 and MILLENER82.

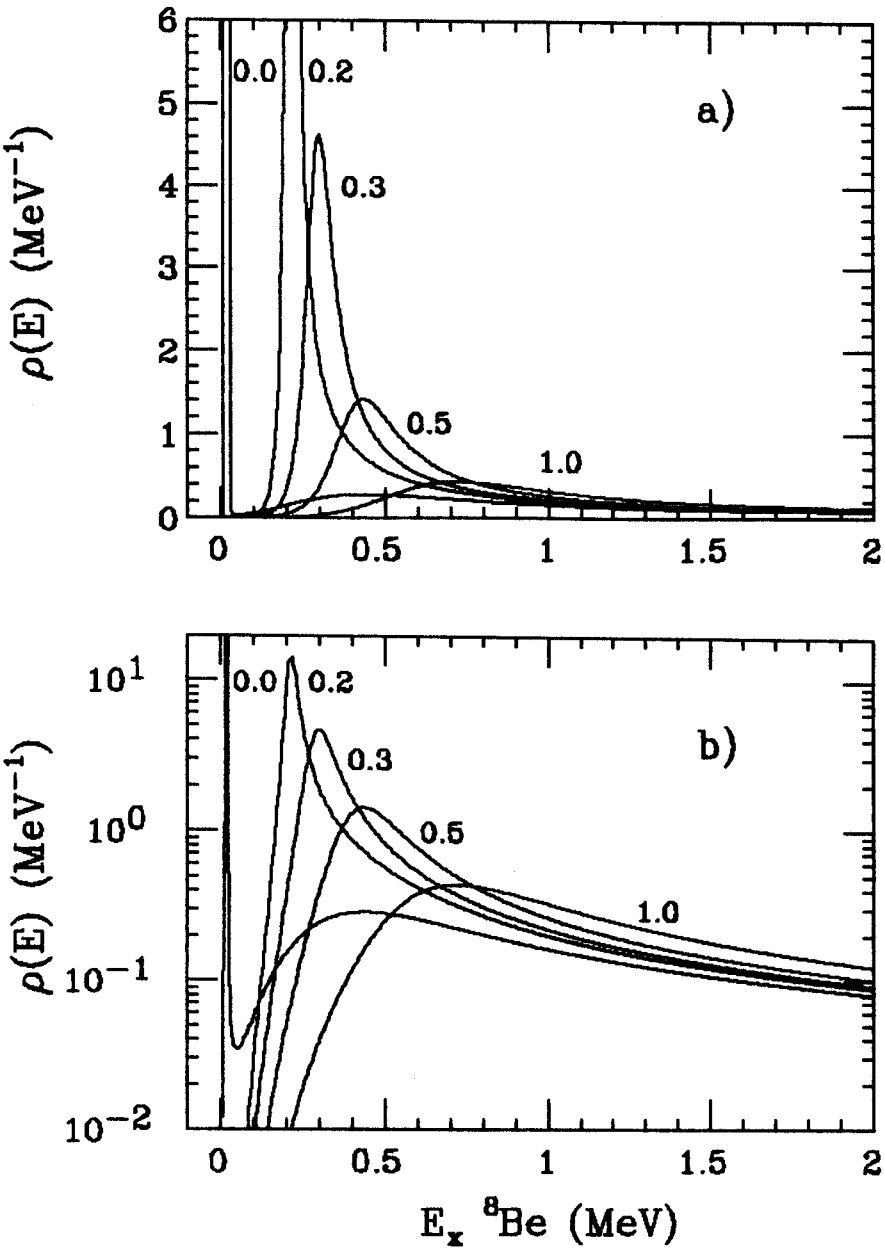

Figure 3.2a Density of states ρ(E) for a hypothetical state in ^{8}Be which decays by s-wave (ℓ=0) emission of two alpha particles. A spectroscopic factor $\theta^2_{\ell=0}$ of 1.0 was used, which is close to the actual value for $^8Be_{gs}$ decay into this channel. Values for E_0 of 0.0, 0.2, 0.3, 0.5 and 1.0 MeV are used. Note the ghost structure for E_0 = 0.0 MeV.

Figure 3.2b, same as Figure 3.2a but with a logarithmic scale.

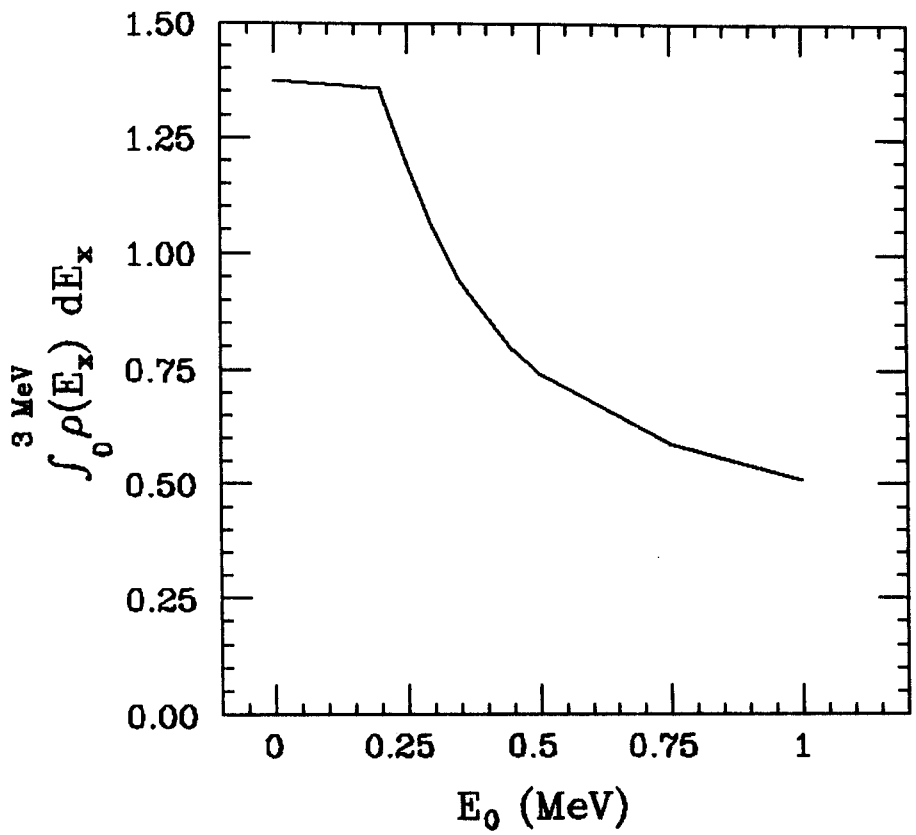

Figure 3.3 Area of ρ(E) (examples of which are in Figures 3.2a,b) integrated from 0 to 3 MeV as a function of E_0. Note that this area is either significantly greater or less than unity under most circumstances. For E_0 = 0.0 MeV, the area of the sharp spike shown in Figures 3.2a,b is 1.0, and the remaining 0.37 is contained in the high energy ghost.

change by many orders of magnitude. This 'ghost' of the ground state in ^{8}Be has been been observed by BECHETTI81.

It is interesting to note that the reaction $^{12}C(\alpha,\gamma)^{16}O$, which is the predominant source of ^{16}O production in the Helium burning in starts, proceeds almost exclusively through the high energy tail of the 7.115 MeV 1^- state in ^{16}O, which is actually bound with respect to this channel by 44 keV. See Section 5.5 of CLAYTON68 for a further discussion.

III.3 Beta Decay Rate:

Equations 3.8 and 3.1 give ρ, the internal density of final states. The external density of states for the beta decay has been discussed previously, and is given in Equation 2.11. The beta decay rate will then be a product of these two densities of state. Thus the beta decay rate λ dE at an energy E is given by

$$\lambda(E)\,dE = \frac{(\hbar c)^7\, g_V^2}{c\,(m_o c^2)^5}\, f_A(W_o,Z)\,\left[\delta_V B(F) + Q_{GT} B(GT)\right]\,\rho(E)\,dE, \qquad [3.10]$$

or

$$\lambda(E)\,dE = \frac{\ln(2)}{6170\pm4}\,\frac{f_A(W_o,Z)\,\left[\delta_V B(F) + Q_{GT} B(GT)\right]\,\Gamma(E)/2\pi}{(\Gamma(E)/2)^2 + (E-E_o)^2}\,dE, \qquad [3.11]$$

where the results of Section II are combined with equation 3.10. In the limit of small and constant Γ, Equation 3.11 reduces back to Equation 2.6. However because of the strong energy dependence of the electron neutrino phase-space factor, a Breit-Wigner lineshape will be populated asymmetrically, with the lower energy tail producing more beta decay rate than the higher energy counterpart.

Figure 3.4 illustrates the effect of the beta neutrino phase-space factor upon the shape of the distribution. The closer a state is to

the endpoint energy, the more dramatic the asymmetry, up to the point where a second maximum ('ghost') at lower energy is produced. Likewise, the larger the width, the stronger the 'ghost'.

This type of ghost phenomena was probably first described by MATT64, while observing the decay of ^{8}B to the lower 16.67 MeV level of the Isospin mixed doublet in ^{8}Be. In that example the decay fed not only the peak, but even more strongly to a tail at lower energy which rapidly increased at lower excitation energy.

It is important to point out that something like an ft value should no longer be defined, since f is no longer evaluated only at a single point. Neither should a branching ratio be defined. A more complete analysis of multi-level final states (see WARBURTON86) shows that interference between two final states of the same spin and parity can actually reduce the beta decay rate.

However in spite of the warnings above, in this simple model a branching ratio might be defined as

$$BR_i = \frac{t}{\ln(2)} \int dE\ \lambda_i(E) \qquad [3.12]$$

if interference effects are ignored (see ZHAO89 for example.) Here t is the beta decay halflife of the parent.

III.4 Beta Delayed Three Body Final States:

Two particularly dramatic examples of beta delayed multiple particle emission were described in the Introduction (Figures 1.2 and 1.3), those of ^{19}B and of ^{22}Al. In these examples many of the states populated by beta decay will result in final states which involve three or more nuclear particles. In the model described above, the beta decay rate per unit energy into one of those levels at a specific

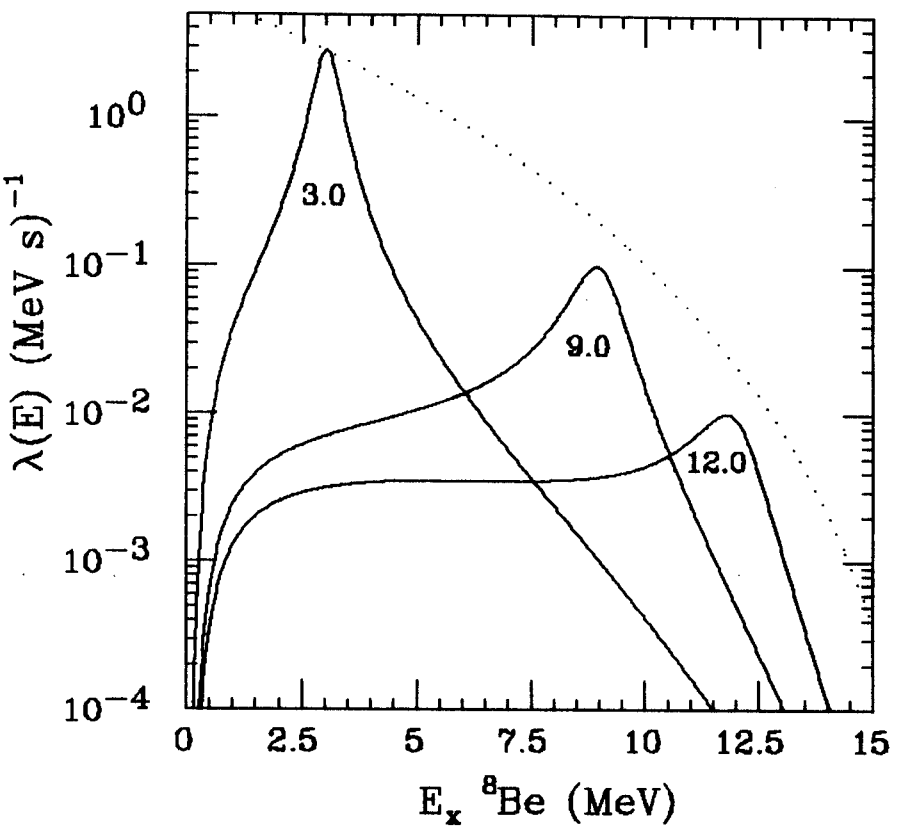

Figure 3.4 The beta decay rate per unit energy $\lambda(E)\,dE$ for ^{8}B decay to a hypothetical state in ^{8}Be with E_o = 3.0, 9.0 and 12.0 MeV. The dotted line represents the shape of the beta neutrino phase space factor $f_A(W_o,A)$ evaluated at each excitation energy E_x.

energy can be obtained as the product of three quantities; 1) the phase space factor for beta decay to that energy, 2) the beta decay matrix element and their associated coupling constants, and 3) the internal density of states at that energy $\rho(E)$ as given in Equation 3.1. The internal density of states at energy E was calculated from the local width of the state at that energy and E_o. Thus independent of the type or complexity of the particle decay, once the total particle decay rate of the state at each specified energy is evaluated by calculation or experiment, the beta decay rate can then be evaluated.

In Figures 3.5 and 3.6, a schematic representation of a beta delayed three body decay is shown. The particle decay rate of the level in the beta decay daughter can not be calculated in a straightforward manner, since the particle decay energy and thus penetrability depends upon what energy in the intermediate state the primary particle decay feeds. In the spirit of Equation 3.9 where the total decay rate is just the sum of all possible partial decay rates, one can imagine that the decay has a differential rate to each excitation energy in the intermediate nucleus proportional to the penetrability at that energy times the internal density of states in that intermediate nucleus. Thus with the intermediate state described by,

$$\rho_i(E_i)\, dE_i = \frac{\Gamma_i(E_i)/2\pi}{(\Gamma_i(E_i)/2)^2 + (E_i - E_{o_i})^2}\, dE_i, \qquad [3.13]$$

and

$$\Gamma_i(E_i) = 2\, \theta_\ell^2\, \gamma^2\, P_\ell(E_2) \qquad [3.14]$$

as prescribed in Equations 3.2 through 3.8, the local decay rate of the state in the daughter populated at E_d becomes

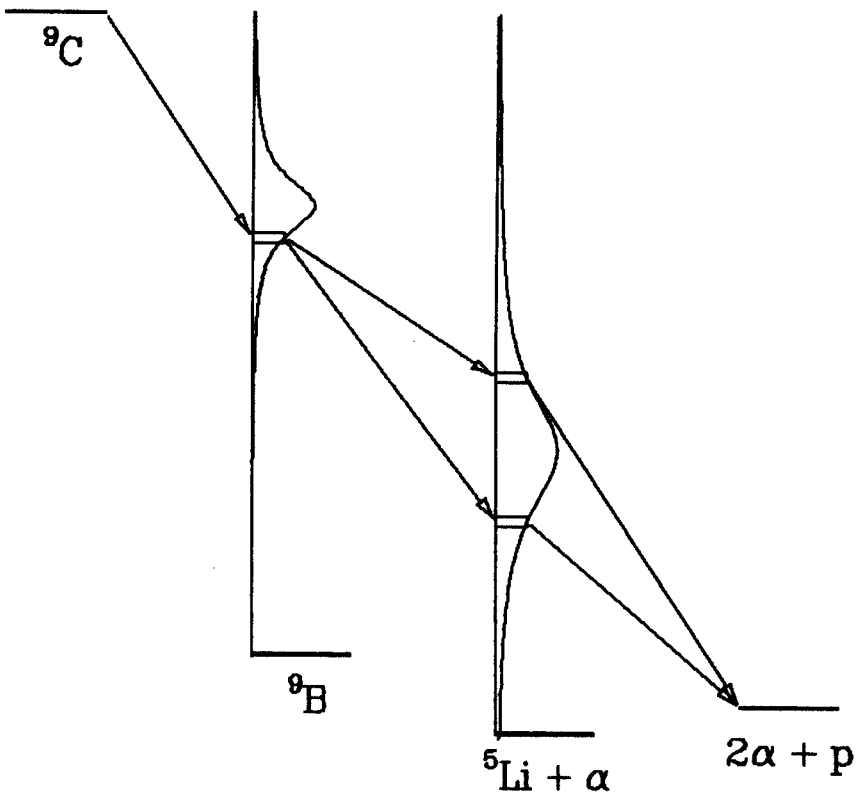

Figure 3.5 Schematic representation of a beta delayed three body decay.

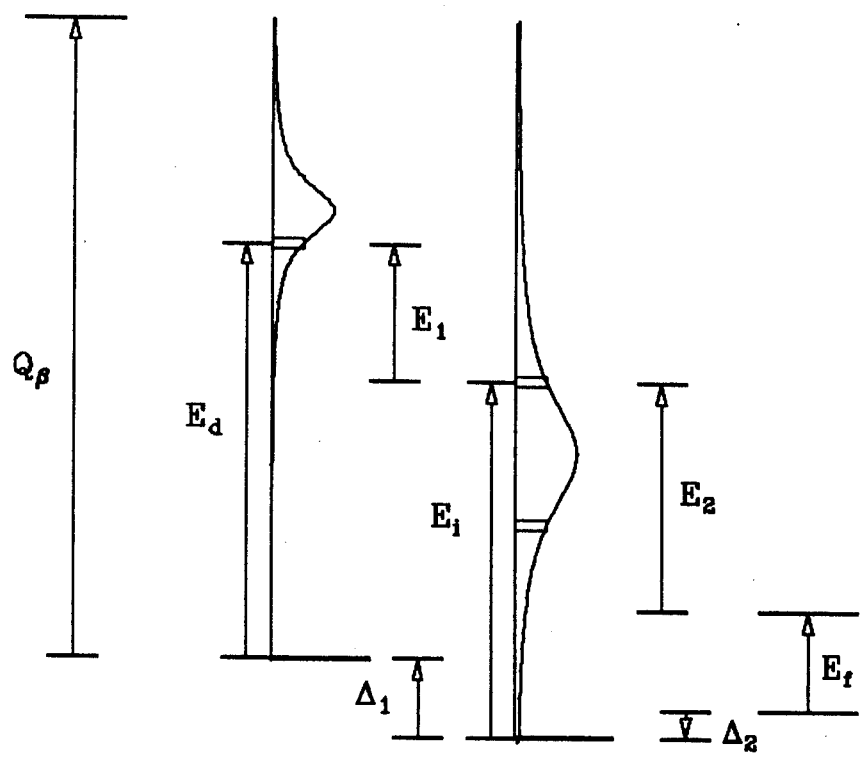

Figure 3.6 Illustration of various energy variables. The excitation energies E_d, E_i and E_f of the daughter, intermediate and final nucleus respectively are defined in the text. Arrows point from A to B where E=B-A. Thus Δ_2 is negative. The beta decay energy from parent to daughter E_β, and particle decay energies from the daughter to intermediate nucleus E_1, and from the intermediate to final nucleus E_2 are used to calculate the penetrabilities $P_1(E_1)$ and $P_2(E_2)$. These then give the local decay rates $\Gamma_d(E_d)$ and $\Gamma_i(E_i)$ in the daughter and intermediate nucleus. Energy differences are calculated by subtracting the value at the tip of the arrow from that at the origin. While two decay channels are illustrated for the decay of the intermediate nucleus, only one particle decay channel of the daughter is shown for the sake of simplicity.

$$\Gamma_d(E_d)\, dE_d = 2\,\theta_\ell^2\,\gamma^2 \int \rho(E_i)\, dE_i\, P_\ell(E_2). \qquad [3.15]$$

The integral in Equation 3.15 represents an average penetrability, weighted by the internal density of states. The internal density of states in the daughter is then,

$$\rho_d(E_d)\, dE_d = \frac{\Gamma_d(E_d)/2\pi}{(\Gamma_d(E_d)/2)^2 + (E_d - E_{o_d})^2}\, dE_d. \qquad [3.16]$$

This expression finds its roots in the generalized density of states concept described in HENLEY60.

In the present notation, the widths are all functions of excitation energy in some nucleus, while the penetrabilities are functions of particle decay energies. As illustrated in Figure 3.5, the relationship between these variables are,

$$\begin{aligned} E_\beta &= m_o c^2 W_o = Q_\beta - E_d\,, \\ E_1 &= E_d + \Delta_1 - E_i \text{ and} \\ E_2 &= E_i + \Delta_2 - E_f\,. \end{aligned} \qquad [3.17]$$

Q_β is the atomic mass excess of the parent minus that of the daughter ground state, Δ_1 is the atomic mass excess of the ground state of the daughter minus that of the intermediate nucleus, and Δ_2 is the atomic mass excess of the ground state of the intermediate nucleus minus that of the final nucleus. E_f is the residual excitation energy in bound or narrow levels in the final nucleus.

III.5 Acceptable Level of Approximation:

The extrapolation of predicted nuclear properties from nuclei close to stability become increasingly unreliable as they are applied farther from stability, and therefore so does the acceptable degree of approximation in the interpretation of the data. Thus even though the

beta-delayed particle emission channels become more complex, the requirements on the thoroughness of the interpretation decreases.

As discussed above, the shell model itself involves some approximations which limit the degree of agreement one would expect with experiment. As discussed in Section II, the apparent quenching of the Gamow-Teller operator is most likely due in part to GT strength to configurations not included in the calculation. It represents on the average a reduction in the observed rate to 0.6 of the calculated value. This value would actually be somewhat different for each individual B(GT), with the value of 0.6 representing an average. It is therefore likely that a large body of experimental B(GT) extracted from delayed particle emission data from nuclei far from stability would be very useful even though they may contain random uncertainties up to perhaps 20% and systematic uncertainties of perhaps 5%.

Unless binding energy effects upon the radial wave functions can be understood better in the future, it is possible that this might even preclude the study of GT quenching far from stability even if the experimental uncertainties mentioned above are achieved.

In a beta delayed three body decay, there are at the minimum five parameters which can be used to fit a given branch; one beta decay branch with a matrix element B(GT), which feeds a level defined by E_{o_d}, which decays with a spectroscopic factor θ_1^2 to a level in the intermediate nucleus defined by E_{o_i}, which then decays with a spectroscopic factor θ_2^2 to the ground state of the final nucleus. In a realistic situation there may be five or ten times this number which contribute significantly to the total beta decay rate of a nucleus. With good

spectroscopy these can be decoupled into groups so that all of them would not be simultaneously adjustable. However, it is probably certain that some residual uncertainty in the B(GT) will remain. The level density in the daughter and in the intermediate and final nucleus will determine the difficulty with which reliable B(GT) will be extracted. When states are broad enough and close enough so that they overlap, they will interfere. In this situation a more complex version of Equation 3.1 should be recovered from the appropriate limit in R-Matrix theory in order to include all phase shifts. An example of such analysis for two body decay can be found in WARBURTON86.

The first place to apply this method is a very light system where the level density is low as are the particle decay multiplicity and complexity. The following Section describes a study of beta decay in Mass 9.

SECTION IV

IV. Beta Decay of ^{9}C:

Figure 4.1 shows the first record of the decay of an atom of ^{9}C from SWAMI56. It was found in a routine analysis of tracks in nuclear emulsion. The decay of ^{8}Li and ^{8}B to ^{8}Be has often been observed as 'hammer tracks,' with the long ionization path of the parent nucleus ending in a short back-to-back 'hammer head' of two alpha particles from the breakup of $^{8}Be(2^{+})$. This first event of ^{9}C was conspicuous in that there were three charged particles emitted following beta decay. The incoming track of the ^{9}C ion and outgoing tracks of the beta particle, two alpha particles as well as that of a proton are all resolved. There energies were calculated from the density and length of the tracks. The analysis of the decay suggests that by the emission of an electron of 4 MeV (suggesting a Q_{β} above 16 MeV), the ^{9}C decayed to a state in ^{9}B at 12.2 MeV, which decayed by the emission of a proton of 7 MeV, the rest of the energy shared by the two alphas. Remarkably this is exactly the decay sequence which while dominating the high energy decay particle spectrum of ^{9}C has been most difficult to study. It has never again been directly observed!

In this section, I will briefly summarize an experiment in which the beta delayed charged particle emission of ^{9}C was studied here at Michigan State University (MSU) by implanting the ^{9}C activity directly into silicon. This experiment has been thoroughly described elsewhere (MIKOLAS88a and Appendix A.) I will then focus on the beta decay to, and particle decay of a state in ^{9}B at 12.1 MeV which is most likely the decay process illustrated in Figure 4.1. This requires using the model described in Section III to simulate the beta delayed three body

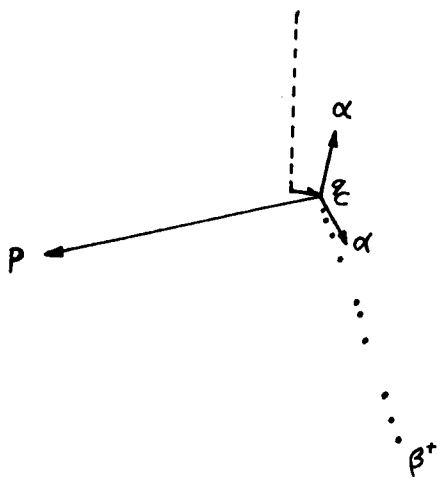

FIG. 1. A photograph of an event interpreted as the beta decay of C^9. The C^9 nucleus (track *F*) was produced in star (*A*) and disintegrated into a proton, two alpha particles, and a positron (tracks 1, 2, 3, and 4, respectively).

TABLE I. Characteristics of C^9 decay.

Track	Range in microns	Identification	Energy in Mev	Angles
F	6.2	C^9	9.4	65°
1	341.0	P	7.6	115°
2	9.9	He^4	2.7	
3	7.8	He^4	2.1	136.5°
4	...		3.1	11°

Figure 4.1 Enlargement of a nuclear emulsion track from a fragment produced in an energetic collision of a relativistic proton with a nucleus of the emulsion. This product was identified as ^9C by its unusual decay mode; $\beta+2\alpha+p$. This is the first atom of ^9C ever to be observed in decay. The energies of the charged particle imply that the ^9C decay populated a level in ^9B at 12.2 MeV, which then decayed by the emission of a proton and two high-energy alpha particles which could not have come from the ground state of ^8Be. This decay mode is the subject of this chapter.

sequential decay of ^{9}B following the beta decay of ^{9}C. I will compare the MSU data with that taken at the 88 inch cyclotron in Berkeley (HARDY65, ESTERL72.) In each situation only an inclusive energy spectrum exists, with no correlations between pairs of particles. In the MSU data, the total energy of all three emitted particles is collected and summed for each event. In the Berkeley data, only the energy of the proton is recorded.

By means of the Generalized Density of States model described in Section III, and comparison with shell model predictions, these two sets of data can be used to produce a single model which explains all data and is consistent with all predictions.

IV.1 The MSU Experiment:

As pointed out above, the experiment is described in detail in MIKOLAS88a which is reproduced in Appendix A. Only the relevant points will be outlined here.

The Reaction Product Mass Separator (RPMS) at the National Superconducting Cyclotron Laboratory (NSCL) at MSU was used to separate fragments of a ^{12}C beam produced by collisions with a Nickel target. ^{9}C fragments were separated from all other activity and implanted within active silicon detectors. When the ^{9}C atoms decayed, the beta particle left the silicon depositing on the average only a few hundred keV of ionization. However, the state in ^{9}B would always decay by the breakup into three particles, two alphas and a proton. A level diagram for ^{9}C decay is given in Figure 4.2. Since the proton and alphas have no energetically accessible excited states in this reaction, the sum of the kinetic energies of the three particles is equal to the excitation

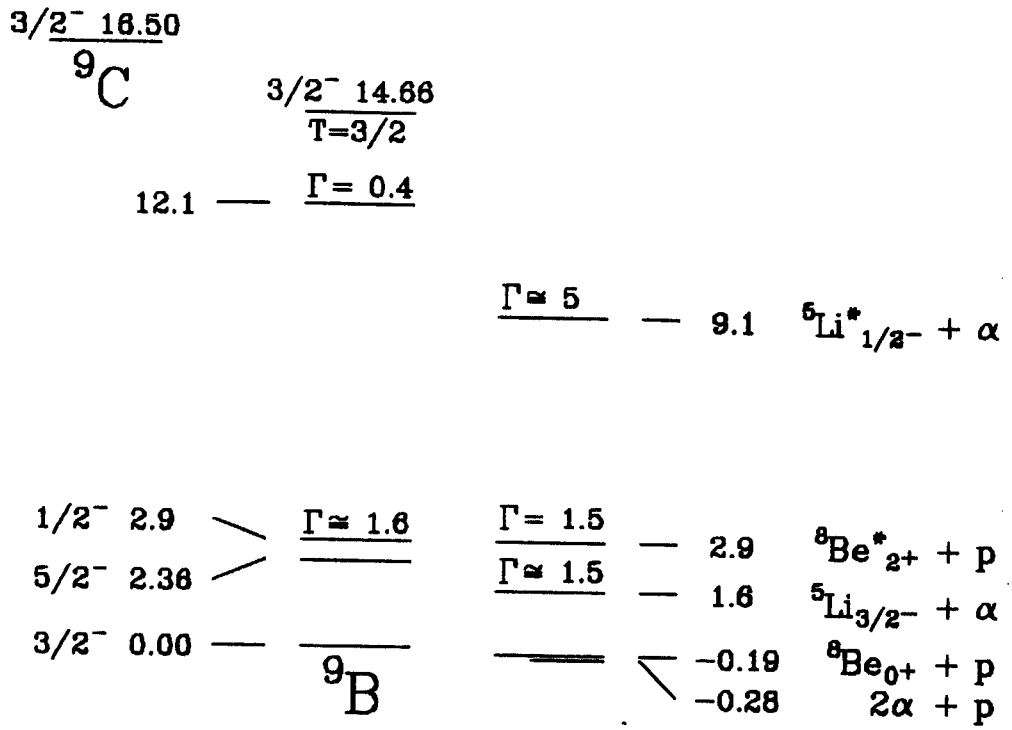

Figure 4.2 Energy level diagram for the decay of ^9C. From Figure 1. of Appendix A (MIKOLAS88a).

energy in the ^{9}B nucleus plus the energy associated with the breakup of the ground state of ^{9}B. If all three particles come to rest within the silicon detectors, their ionizations are collected together and the a signal is produced proportional to the total breakup energy of the system.

In figure 3 of Appendix A, the energy spectrum recorded in a silicon surface barrier detector of 400μm thickness is shown. The two prominent peaks at low energy represent the population of the ground state and $5/2^{-}$ excited state of ^{9}B at 2.36 MeV. A small peak near 12 is also observed. The number of ^{9}C ions implanted was compared to the area of these peaks, and branching ratios were extracted under the assumptions that these levels were narrow and their shapes calculable directly from a simple model of the energy loss of the beta particle as it is emitted in different direction. The branching ratios so extracted are summarized in Table 1 of Appendix A. They are also converted to B(GT) under the assumption that the levels are narrow and formulae of Section II can be used. The experimental B(GT) are compared to those predicted by the shell model, and those extracted from various published observations of ^{9}Li decay. Overall agreement between all three sets of B(GT) is good. However, for the branch to the $5/2^{-}$ level the B(GT) extracted from ^{9}C decay is over a factor of two lower than that observed for ^{9}Li. As pointed out in Section VII of Appendix A, if these values are verified it represents the strongest mirror asymmetry observed to date.

A peak is also observed near 12 MeV resulting most likely from the decay of a level in ^{9}B at 12.1 MeV. If it were to decay by proton

emission to the ground state of ^{8}Be, the resulting protons would have a kinetic energy of 11 MeV, and a corresponding range of almost 1 mm in silicon - twice the thickness of the detector used. Only the protons emitted close to the the plane of the silicon would come to rest within the silicon and result in complete collection of the ionization. Many more would pass out the sides such that a significant fraction of their energy would be missing from the spectrum. These protons would produce a tail at lower energy in the spectrum.

The results of a Monte Carlo simulation of such a situation are shown in Figure 4.3 where they are compared to the experimental data. The simulation represents the beta decay of ^{9}C to a state in ^{9}B at 12.1 MeV which decays 100% by proton emission to the ground state of ^{8}Be. The peak lies at a slightly higher energy because of the energy loss of the beta particle in the data and in the simulation. The simulation has been normalized to the data in such a way that the areas within 800 keV of the peak are equal. Under these assumptions only 20% of the events occur within the normalized area, with 80% of the events generating counts at lower energy. This efficiency implies a B(GT) for the 12.1 MeV near 3.0, which is very large, containing 20% of the Ikeda sum rule strength of $(g_A/g_V)^2$ 3 |N-Z|. However, as can be seen below, this is an extreme upper limit.

IV.2 Three Body Simulation for ^{9}C:

Three factors taken together strongly suggest that the level at 12.1 MeV in ^{9}B decays most often through some channel which distributes the energy much more evenly between the three particles than does the ^{8}Be(gs) channel. The first is the beta delayed alpha and two alpha

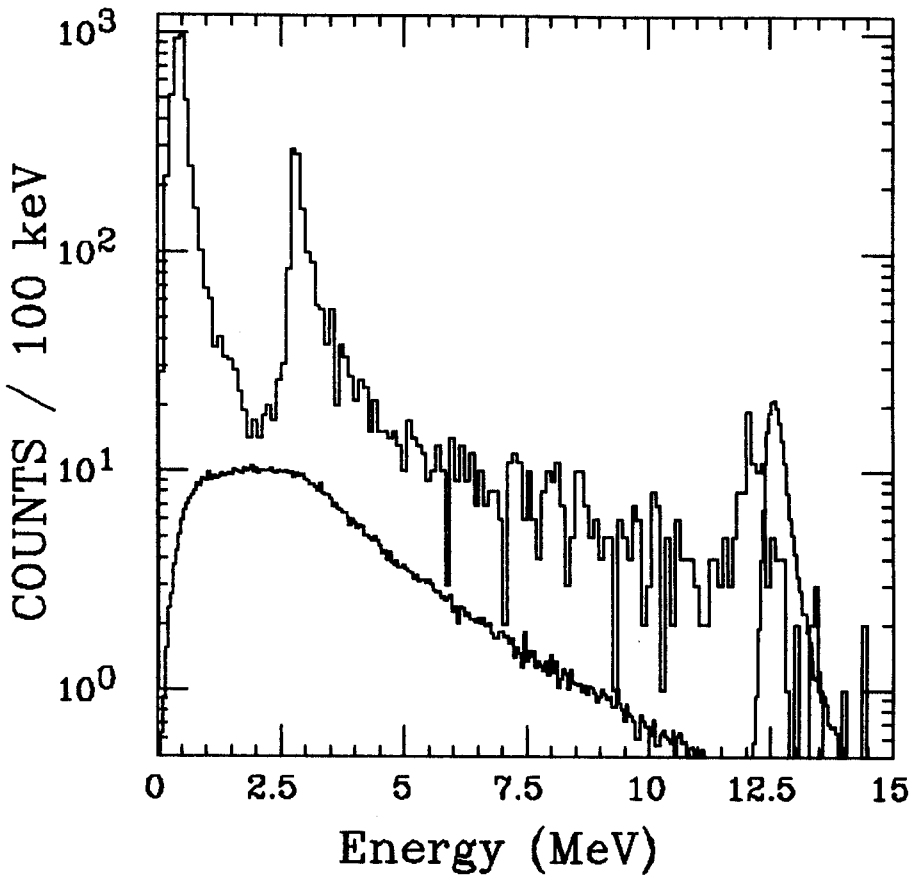

Figure 4.3 Monte Carlo simulation of the decay of ^{9}C to a level in ^{9}B at 12.1 MeV. The ^{9}C is uniformly distributed in a 400μm thick silicon detector. In this situation 81% of the events produce counts below 10 MeV because of the escape of the proton from the silicon before losing its full energy. The disagreement in the 12.1 MeV peak position is within the quoted uncertainty in energy in MIKOLAS88a. The energy assignment comes from ESTERL72.

spectra of ^{9}Li from NYMAN81 and LANGEVIN81. In these experiments ^{9}Li was deposited on a thin carbon foil, and the alpha activity counted in separate silicon detectors. A strong component in the beta decay resulted in single alpha particles up to 6 MeV, and two alpha summed energies of 9 MeV. Clearly a process not involving ^{8}Be was contributing these high energies.

^{9}Li activity was also implanted in silicon at MSU. In Figure 4.4, the beta delayed two alpha spectrum for ^{9}Li decay is shown. Since the decay of ^{9}Be is to two alpha particles plus a neutron instead of a proton in the case of ^{9}B decay, the fraction of the energy shared by the alphas could be determined. Again a significant fraction of the events result in high energy alpha particles.

The second factor suggesting channels other than proton + ^{8}Be(gs) is the shape of the delayed proton spectrum from ^{9}C decay of ESTERL72. Here in addition to two small peaks at 9 and 12 MeV, a large continuum in the proton spectrum rises to lower energies, containing more than 95% of the strength above 3 MeV in the proton spectrum. No such intense continuum is seen in the MSU ^{9}C data (Figure 3 of Appendix A.)

Thirdly, the behavior of the predicted spectroscopic factors for states near 12 MeV in ^{9}B is quite erratic, often favoring ^{5}Li channels over those involving ^{8}Be. A complete table of spectroscopic factors for six decay channels is given in Table 2 of Appendix A, and they are discussed in Section VI of that reference.

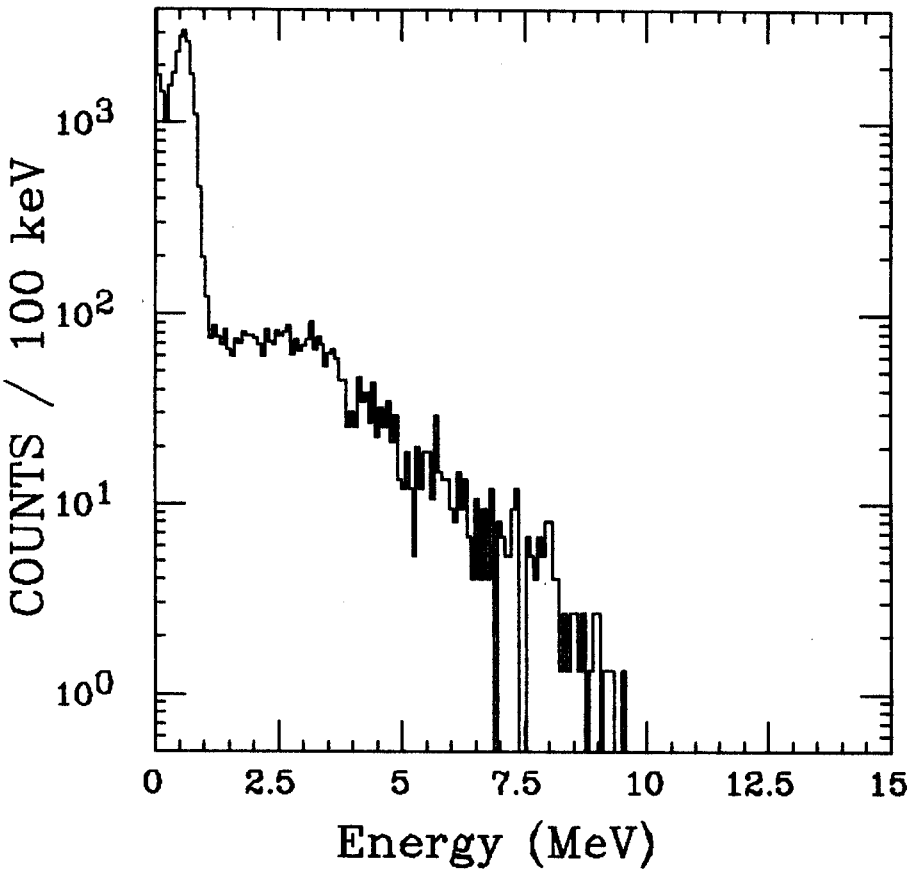

Figure 4.4 Charged particle sum energy spectrum for the beta delayed 2α(+n) decay of ^{9}Li separated with the RPMS. The uncharged neutron deposits no energy in the silicon; thus the energy of the two alpha particles can be determined separately from the total breakup energy.

Finally, the single event of SWAMI56, while not statistically overwhelming, does suggest that channels for the decay of the 12.1 MeV state involving ^{5}Li (suggested by lower energy protons) are not unlikely.

In order to investigate the role of ^{5}Li +α channels in the decay of the 12.1 MeV level, a computer program was written to calculate the decay probabilities for states unbound to three body decay. The program is generalized and easy to use. The proposed excitation energies, B(GT) and spectroscopic factors for each ℓ are entered in a small table. The complete 3 body decay is simulated, and inclusive and correlated two particle energy spectra are generated for the beta decay of interest. The data can be compared directly with experiment and the agreement evaluated. The calculation is complex, and takes up to many minutes to complete a calculation of a delayed particle spectrum using a VAX 8530 computer. Thus it is not well suited for a fitting procedure which varies each of the parameters. In the case of ^{9}C decay the number of fitted parameters far outweighs the number of features in the data. None-the-less, little is known about the decay of this level, and it's basic nature can be explored with such an analysis.

For the sake of simplicity only three channels were chosen for the initial calculation; ^{8}Be(0^{+}) + p; (ℓ=1), ^{8}Be(2^{+}) + p; (ℓ=1), ^{5}Li($3/2^{-}$) + α; (ℓ=2). The ℓ=2 channel for ^{5}Li+α was chosen as the one which tended to show the strongest spectroscopic factor for those levels near 12 MeV calculated in Appendix A. The first step in the procedure is to reproduce the shape of the intermediate states in ^{8}Be and ^{5}Li. In Figure 4.5, the ground state and first excited states of

^{8}Be near 3 MeV are shown as calculated from a simple Breit-Wigner. The spectroscopic factors and E_os are varied to reproduce published widths. In Figure 4.6 the shape of the ground state ($3/2^-$) of ^{5}Li is shown. Here only the spectroscopic factor is varied, as E_o is defined as zero for the ground state.

Next, the width $\Gamma_d(E_d)$ of the daughter ^{9}B is calculated as a function of energy. At each energy E_d the width is calculated from Equations 3.13 through 3.15 by evaluating the probability of particle decay into each of the channels. Finally the shape of the 12.1 MeV level in ^{9}B is calculated. It is shown as the solid curve in figure 4.7. The dotted curve in that figure is the same shape, but weighted by the phase space factor for the beta neutrino pair. A long low energy tail emerges which represents the competition between the decrease in internal density of states in the ^{9}B nucleus off-resonance, and the rapid increase of density of states in phase space for the beta neutrino pair. The curve falls to zero at the particle decay threshold for ^{9}B.

At each energy E_d in the ^{9}B level the fraction of particle decays which feed each energy in each of the intermediate states is now calculated. These fractions are normalized, inverted and then used by a Monte-Carlo routine to produce the final spectra. An important element in the Monte-Carlo simulation is the decay in flight of the intermediate nucleus. For example if the ^{9}B nucleus decays to ^{5}Li + α, the ^{5}Li takes 4/9 of this primary decay energy as kinetic energy. The recoiling ^{5}Li then emits the proton with some angular distribution, and the laboratory kinetic energy of the proton depends upon this angle.

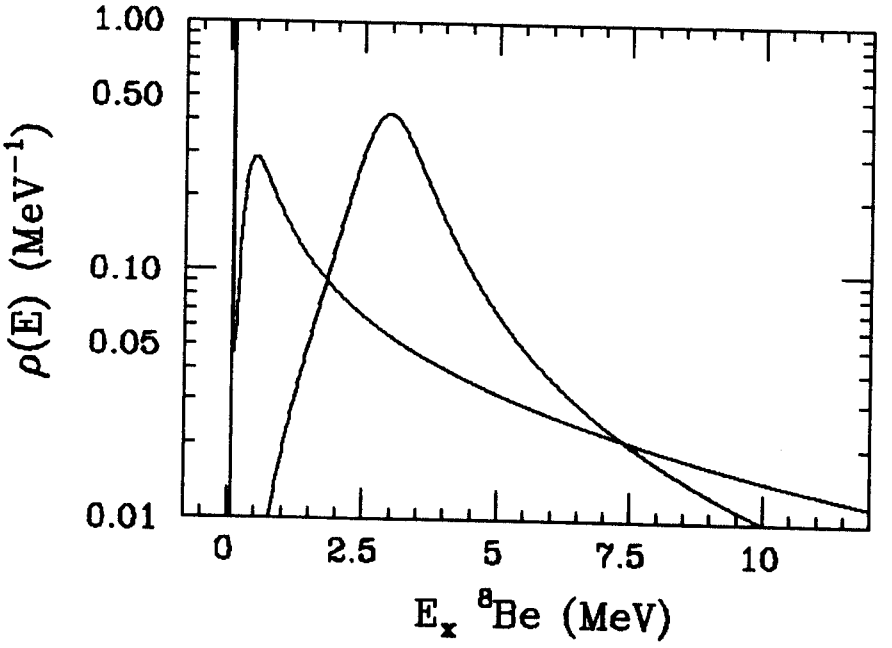

Figure 4.5 Line shape for the ground state (0^+) and first excited state (2^+, 2.9 MeV) of ^{8}Be used in the calculation of the breakup of ^{9}B through these channels.

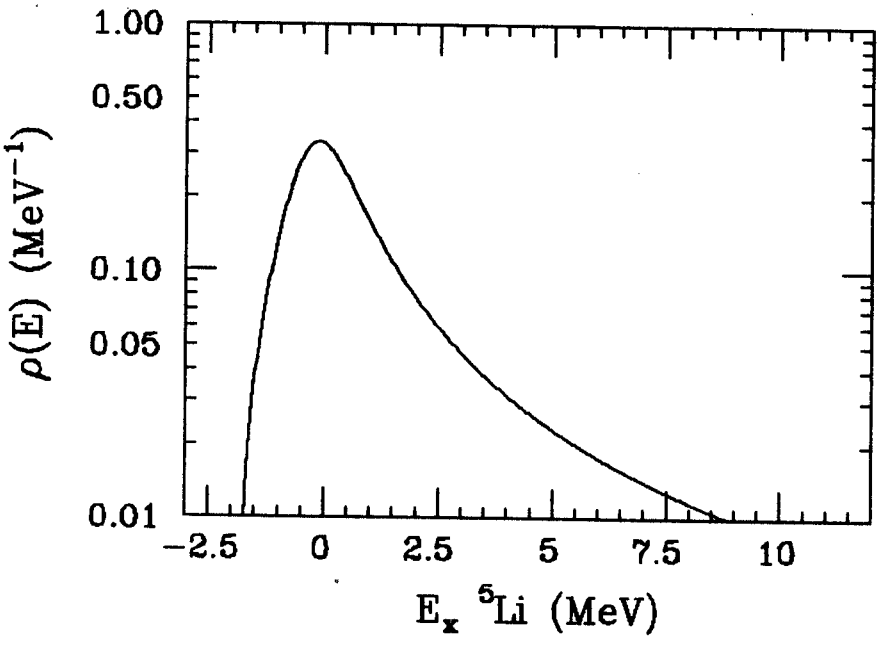

Figure 4.6 Line shape for the ground state ($3/2^-$) of ^{5}Li.

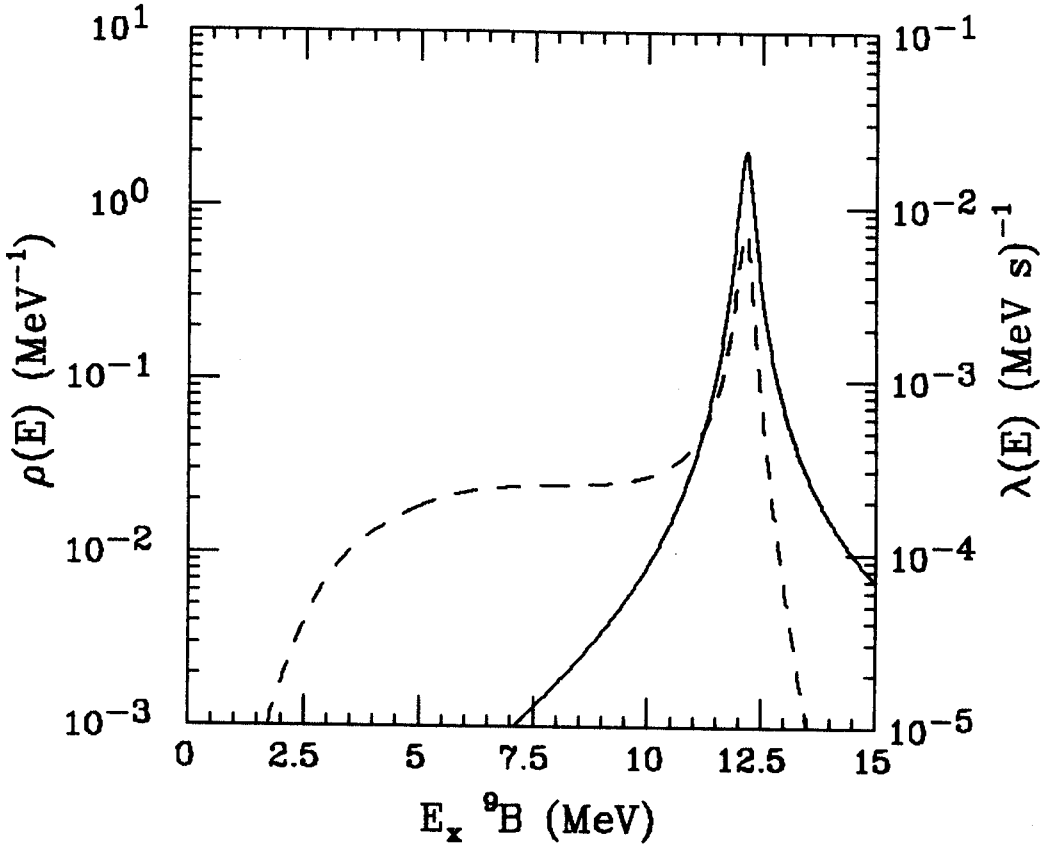

Figure 4.7 (Solid) Density of states function ρ(E) for the 12.1 MeV state in ^9B populated by the decay of ^9C. The spectroscopic factors have been adjusted to reproduce the observed FWHM of 400 keV. (Dotted) The decay rate λ(E) to ^9B obtained by multiplying ρ(E) by the phase space factor for the beta neutrino pair.

While the program will accommodate an angular distribution with respect to the primary decay axis, none is used in this simulation again for reasons of simplicity.

The simulation of the total charged particle energy spectra for the decay is shown in Figures 4.8 and 4.9. The agreement of the proton inclusive spectrum with that of ESTERL72 is excellent. In Figure 4.9 the same proton spectrum is superimposed on the Berkeley data. A branch to the broad $1/2^-$ level in ^{9}B at 2.9 MeV is also included to represent the lowest energy portion of the data. The agreement is excellent. Even with the simple assumptions above the complete spectrum can be explained by the strong population of the ^{5}Li channel and weak and nearly equal population of the channels involving ^{8}Be. The results of the fit are summarized in Table 4.1.

The process by which the final set of θ_ℓ^2 were obtained was an interactive process between the researcher and the computer. For example, when structures are isolated, first approximations to some parameters can be obtained in a nearly uncoupled mode. Adjusting certain parameters to fit certain peaks is the quickest way to pin down some parameters. Others require many iterations of trial and error. A second version of the program is being written which should run in a much shorter period of time, perhaps a few CPU seconds per iteration. When this is complete, automated iteration can be implemented. However, the number of fitted parameters will be large, and a large amount of interactive work will still be necessary in most cases to 'keep the program honest.'

Table 4.1. Spectroscopic Factors fit to the beta delayed proton spectrum of Esterl et al. The last column represents the calculated efficiency for collection of the full energy peak for ^{9}C activity in the 400μm thick detector used in the present experiment.

Channel	Spectroscopic Factor Wigner SP units	Partial Width at Resonance (MeV)	Full Energy Peak Efficiency (400μ)
$^{5}Li + \alpha$	0.07089	0.531	0.88
$^{8}Be(gs) + p$	0.00104	0.027	0.27
$^{8}Be(2^{+}) + p$	0.00363	0.047	0.46
	TOTAL:	0.606	TOGETHER: 0.79

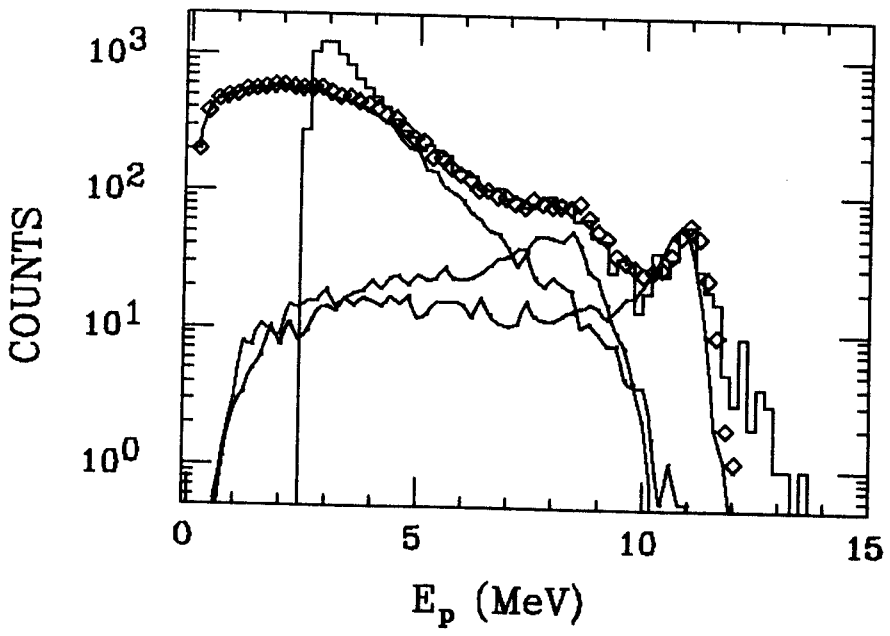

Figure 4.8 Components of the calculated beta delayed proton spectrum. The three solid curves represent alpha decay to the $3/2^-$ ground state of ^{5}Li which then emits a proton in flight, proton decay to the 2^+ excited state of ^{8}Be near 3 MeV and proton decay to the 0^+ ground state of ^{8}Be, listed in increasing order in average energy. Diamonds represent the sum of the three contributions, and the histogram is the data of ESTERL72.

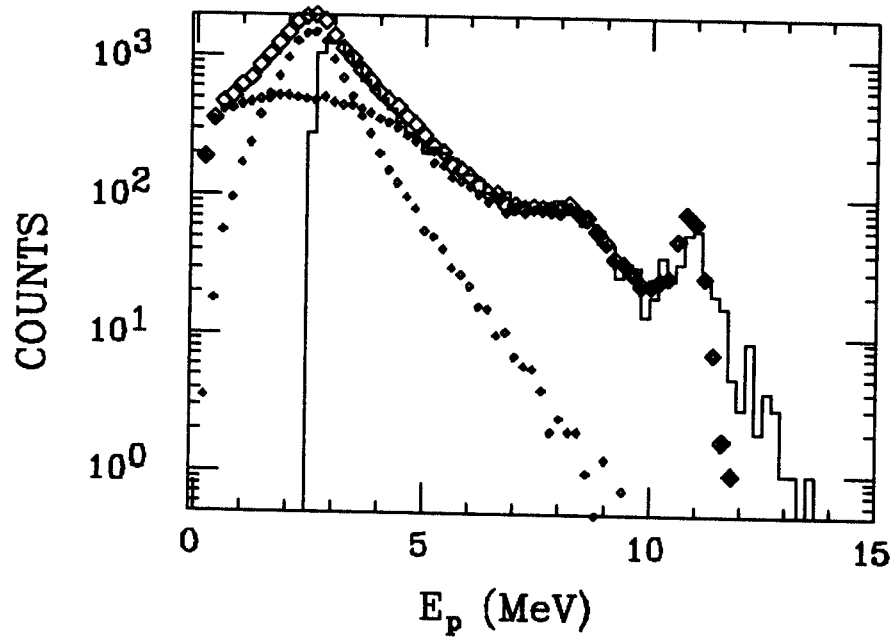

Figure 4.9 The contribution from the long high-energy tail of the $1/2^-$ level at 2.9 is included. The sum of all four components is shown by the large diamonds. The histogram is the same as in Figure 4.8.

In order to use such model to extract accurate B(GT) from delayed multi-body breakup, better coincidence data will be needed. In the same spirit that three-moving-source fits are performed to inclusive date where double-differential cross-sections are available, two particle angular correlations will significantly improve the reliability with which spectroscopic factors and B(GT) can be determined from beta delayed multi-particle data. A further discussion of such possibilities can be found in the final Recommendations section.

IV.3 Conclusion on ^{9}C study:

A technique for the study of the beta decay branching ratios of beta delayed particle decay precursors has been developed. The technique takes takes advantage of the recoil energy of projectile fragments to implant them within the volume of an active silicon detector where the sum energy of the three particles is recorded. This technique, coupled with the intermediate energy heavy ion beams available at NSCL and the mass separation of projectile fragments with the RPMS, provided a situation in which the decay of the exotic nucleus ^{9}C to the ground state and first two negative parity states of ^{9}B could for the first time be observed. Branching ratios and B(GT) have been extracted for these states.

Higher lying states are open to complex decay channels which sometimes produce high energy protons. In particular, a state at 12.1 MeV in ^{9}B is strongly populated by ^{9}C decay ($\log(ft)\approx 3.6$). While the particle breakup of this level produces a distinct peak at 12 MeV in the data, the branching ratio is not immediately available from a straightforward analysis of the spectrum. A strong proton decay branch of this state to the ground state of ^{8}Be would result in an efficiency

of only ≈25% for containing the total energy of the 12 MeV (cm) proton since its range is much greater than the thickness of the detector. On the other hand, the delayed proton data of Esterl show that the decay predominantly proceeds through channels which result mostly in the emission of low energy protons.

A model has been developed to understand the particle decay of broad levels populated in beta decay. The model follows sequential particle decay where the final state involves three separate nuclear particles - in this case two alpha particles and a proton. A simple Breit-Wigner representation of the internal density of states in the primary (^{9}B) and intermediate (^{8}Be and ^{5}Li) resonances coupled to an external density of states function generated by the Coulomb wave-functions. A generalized program has been written to carry out such calculations, providing various density of states functions and the resulting inclusive and coincident laboratory energy spectra of each of the resulting particles. Thus experimental data of both inclusive and kinematically more complete nature can be fit with a few simple parameters; beta decay and particle decay matrix elements and resonance energies.

The beta delayed proton data of Esterl were fit with this model. The data show two distinct peaks which correspond to two particle decay channels; ^{8}Be(gs)+p and ^{8}Be(2^{+})+p. The area of these structures are almost exclusively the result of decays through these channels, and thus represent a nearly independent measure of these branches. The third channel to be considered is ^{5}Li+α. This channel appears to dominate the particle decay spectrum of the 12 MeV state. The spectroscopic factors for the three particle decay channels were adjusted to

match this spectrum. As each channel dominated a given region of the proton energy spectrum, a straightforward fitting could be carried out in this particular case without a least-squares fitting procedure. Since the overall width of the state is experimentally known to lie between 400 and 600 keV, only two parameters were varied; the ratios of the spectroscopic factors of the two ^{8}Be+p channels to that of the ^{5}Li channel. The three spectroscopic factors were always renormalized to maintain a constant width in the peak.

Table 4.1 gives the final spectroscopic factors obtained in the fit to the data of Esterl. The certainty of the two ^{8}Be values is a factor of two in either direction, while that of the ^{5}Li is closer to 30% - the certainty of the width of the 12.1 MeV peak in the present NSCL data. Uncertainty due to inadequacies of the model itself are difficult to assess. More detailed examination of empirical phase shift data in α-α and p-α scattering may provide a slightly better representation of these resonant states.

The calculated laboratory proton spectrum is then used to produce a predicted total energy spectrum as would be recorded in a 400μm thick silicon detector as used in the present experiment. This calculation shows that 25% of the events which are in the 12.1 MeV peak in ^{9}B produce a sum energy well below this value because the protons physically escape the silicon detector before depositing all of their energy. Efficiencies for the proton from each of the three channels considered are also given in Table 4.1.

The calculated efficiency of 75%, obtained from the model using the parameters fit the data of Esterl can then be used to extract a B(GT) for the 12.1 MeV state. A value of 1.7 is obtained for this

matrix element (log(ft)≈3.6). This represents 13% of the total GT sum rule strength for ^{9}C decay. See Figure 4.10. The value compares very favorably to the predicted value of 1.9 to the third $3/2^-$ level in 9B using the 6-16TBME interaction. The three other interactions give predicted values between 1.4 and 1.8. That reference gives other evidence which supports the assignment of the observed 12.1 MeV level to the third $3/2^-$ state in ^{9}B. Thus the agreement of the experimental B(GT) with the theoretical values is reassuring, especially when the theoretical values are relatively interaction-independent.

Future studies of the decay of ^{13}O to particle unbound levels in ^{13}N will involve a further technical extension (four particles in the final state) as well as a further extension of the model itself. This experiment is outlined in the following chapter. More kinematically complete data (multiple detectors measuring different particles) may help distinguish between competing particle decay channels. Other techniques, such as two α plus neutron detection for the mirror decay of ^{9}Li will also be helpful in separating the various particle decay channels and thus improving the reliability of the fitting.

Computational improvements on the program which calculates the spectra will bring the iteration time down to roughly one per second. At this point automated search and fitting routines will be able to produce fits where the channels are not so clearly separate in the inclusive data as they are for ^{9}C decay.

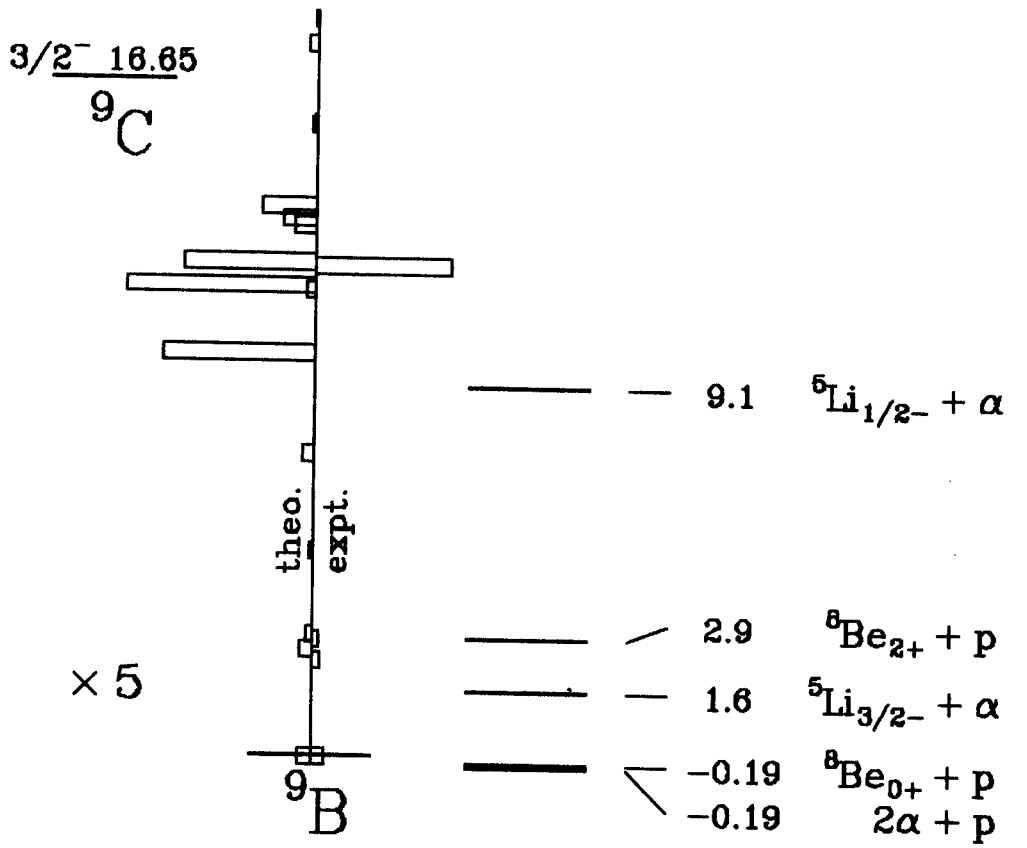

Figure 4.10 Experimental and Theoretical beta decay B(GT) distributions and calculated particle decay threshold energy for ^{9}C. The third predicted $3/2^-$ is assigned to the strongly populated state observed at 12.1 MeV as discussed in the text. Good agreement is found between the predicted and new experimental B(GT) to the three lowest negative parity states, as well as for the third $3/2^-$.

SECTION V

V. Other Cases of Beta Delayed Charged Particle Emission:

V.I ^{18}N:

While the method of implanting beta delayed charged particle emitting precursors inside silicon was developed for the study of ^{9}C decay, it was even better suited to the study of the delayed alpha emission from the beta decay of ^{18}N. While ^{9}C produced high energy protons which could have a range up to 1 mm in Si, ^{18}N activity produces beta delayed α particles only up to a few MeV which have a ten times shorter range. Thus for this study the detectors could be much thinner (50μm vs. 400μm) and thus the effect of the beta energy loss on the delayed charged particle spectrum could be minimized.

Figure 5.1 shows a partial decay scheme for ^{18}N. A more complete summary of decay to bound and narrow ($\Gamma \approx \Gamma_\gamma$) states can be found in OLNESS82. Two levels are of special interest in this experiment. The 1^-_3 level (E_x = 7.619) and 1^-_4 level (E_x = 8.039) are 1.392 and 1.812 MeV respectively above α decay threshold in ^{18}O at 6.227 MeV. They are predicted by OLNESS82 to be strongly populated by Gamow-Teller decay of ^{18}N. In a future experiment ZHA088 plan to determine the parity non-conserving α decay of a 0^- level (E_x = 6.880) at 0.653 MeV above alpha decay threshold. Since the alpha spectrum is dominated by the allowed alpha decays, it was critical to understand the allowed beta delayed alpha spectrum before finalizing the design of the PNC experiment.

In the present experiment ^{18}N activity was implanted in a series of 50μm thick silicon surface barrier detectors. The range distribution covered about 300μm, and thus to contain most of the

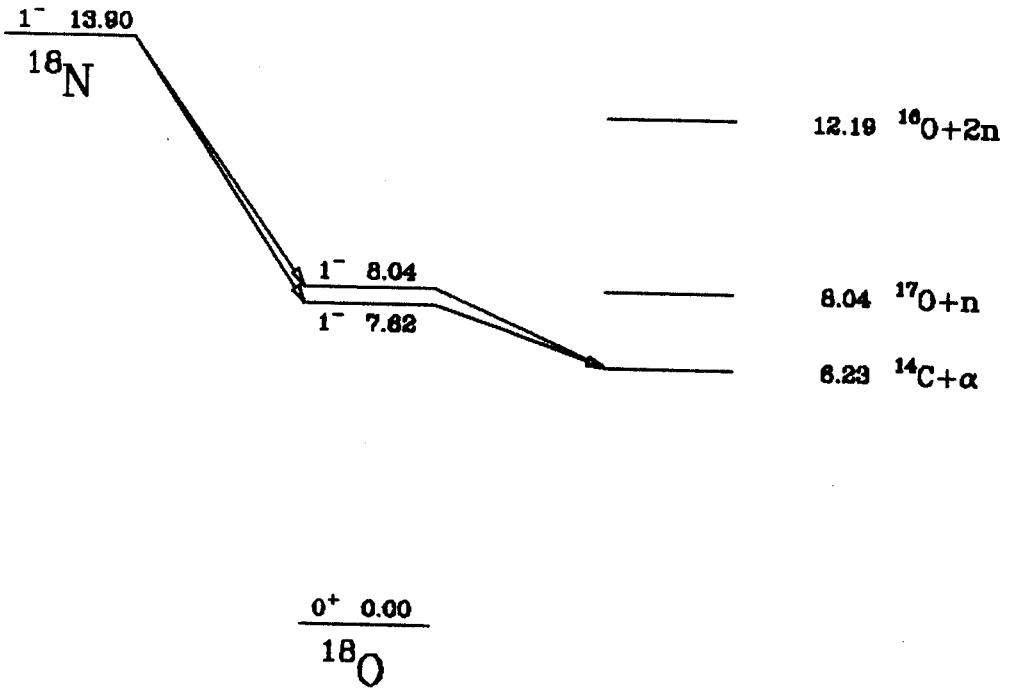

Figure 5.1 Partial Decay Scheme for ^{18}N beta delayed alpha emission. Information take from AJZENBERG-SELOVE87, WAPSTRA86, OLNESS82 and ZHAO89.

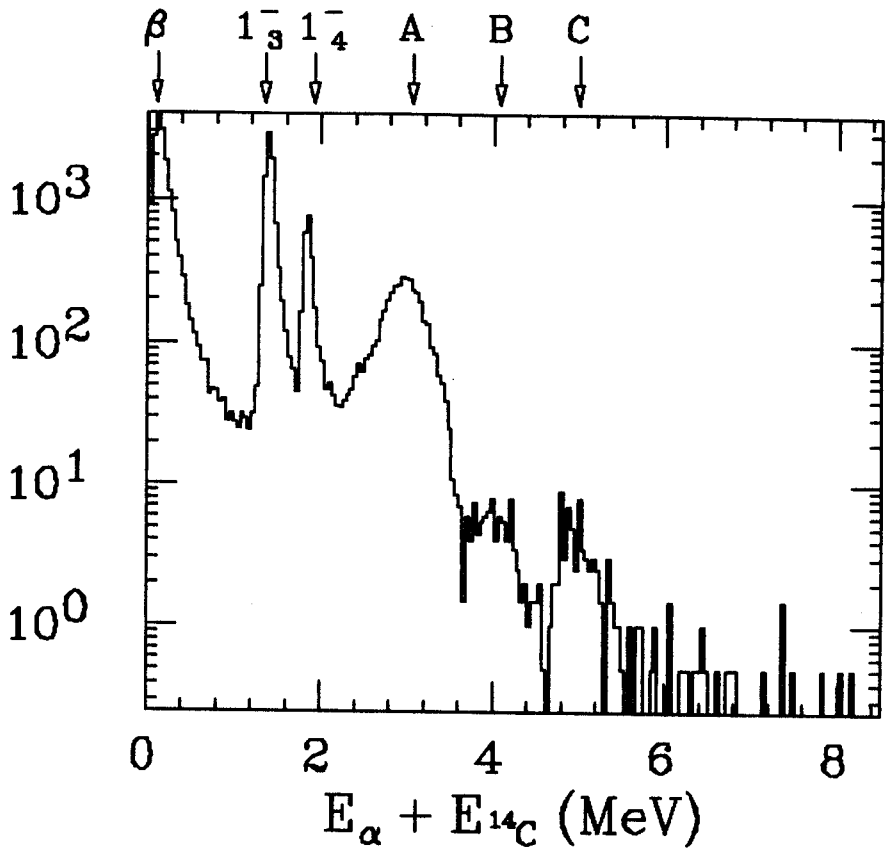

Figure 5.2 Histogram of energy recorded in a 50μm thick silicon detector during the 'Beam Off' periods following ^{18}N implantation. The assignment of each peak is indicated. ZHA089 suggest that the structure labeled A is actually a group of known but unresolved 1^- levels. The structures labeled B and C are likely to be 1^- or 2^- levels in ^{18}O which have not yet been identified.

activity the silicon detectors were inclined at an angle of 45° with respect to the axis of incidence. The entire detector assembly including the position sensitive proportional counter were kept in a helium atmosphere to minimize the number of ^{18}N which could stop in the air between detectors and introduce uncertainties in the efficiency. The beam was run in Fixed Cycle mode (Section VII.3.3.2). The beam was turned on for roughly one mean life of ^{18}N, and then off for the same period (during which time the decays were recorded).

Figure 5.2 shows a decay energy spectrum recorded in one of the silicon detectors. The large low-energy tail labeled ALTERNATE beta is produced by background and by beta decay to bound states. The beta from these decays occasionally passes through a large amount of silicon and therefore produces a large signal in the detector. Two peaks labeled 1_3^- and 1_4^- are clearly visible, confirming the predicted strong branches to these two levels. The results of this experiment and interpretation are summarized in ZHA089.

V.2 ^{13}O Decay:

The case of ^{13}O decay is potentially even more complicated than that of ^{9}C. As shown in Figure 5.3, ^{13}O is a candidate for beta delayed four body break-up. The half life and ground state branching ratios are also important for studying mirror asymmetry in beta decay, and for the potential of observing second class currents (WILKINSON71b, TOWNER72, WILKINSON74c, ASAHI89.

A very preliminary decay energy spectrum for ^{13}O recorded in a 400μm thick silicon detector is shown in Figure 5.4. Here again the lowest energy peak is due to background and beta decay to bound states.

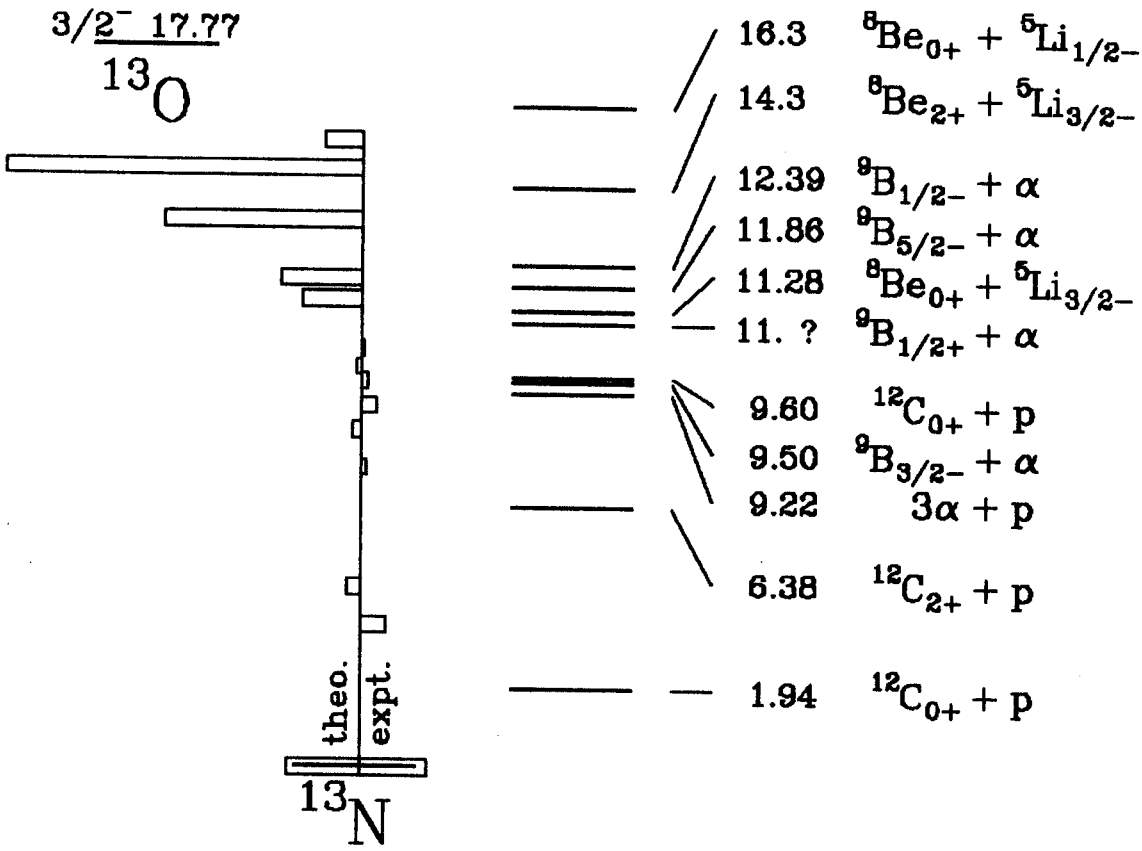

Figure 5.3 Decay scheme for ^{13}O delayed charged particle emission. Compare to ^{9}C in Figure 4.10

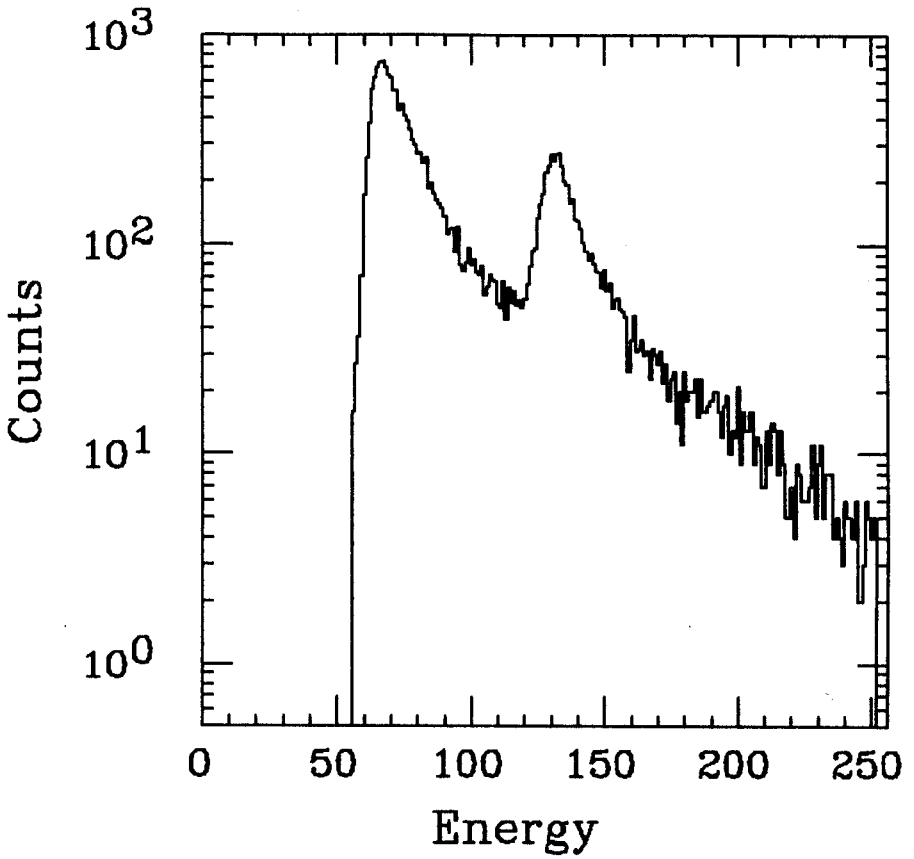

Figure 5.4 Preliminary decay energy spectrum for ^{13}O ions implanted in a 400μm thick silicon detector. The lowest peak is most likely due to beta decay to bound states where only the beta particle deposits ionization in the silicon.

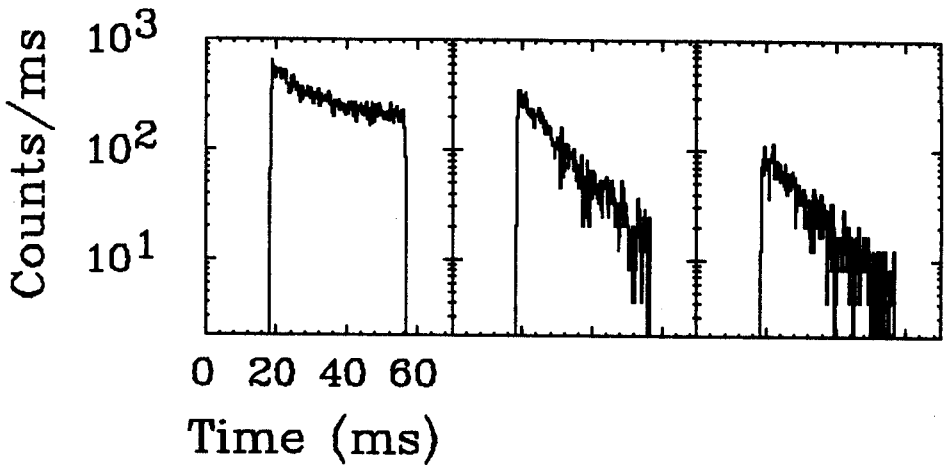

Figure 5.5 Beam off time spectra for the three peak structures in Figure 5.4 and for the highest energy part. Once a half life is established these curves can be used to determine the fraction of the area under each peak which is due to real ^{13}O decay.

The data was taken in the Fixed Cycle mode with the beam on time roughly 1 1/2 mean lives and the beam off roughly 2 mean lives. In Figure 5.5, time spectra for each of the three peak structures and for the high energy continuum are shown. Once a half-life is established from a thorough examination of all data from all runs, the exponential part of each curve can be extracted and thus the contribution from real ^{13}O decay in each of the energy bins can be measured. A summary of the shell model predictions using the 6-16TBME interaction, and measurements of ESTERL70 is shown in Figure 5.3.

SECTION VI

VI. The Michigan State Reaction Product Mass Separator (RPMS):

VI.1 E × B Recoil Isotope Separation (RIS):

A Recoil Mass Separator uses electric and/or magnetic fields to separate isotopes which are moving at a velocity imparted by the nuclear reaction. Since recoils from nuclear reactions are almost always stripped of at least some of their electrons, they carry a charge and thus may be manipulated by the fields. Reactions which produce nuclei far from stability often result in a spread in velocities; the separating device must therefore disperse in (for example) m/q while remaining achromatic in velocity. This can be done with the use of two forces whose effects have different dependence on the velocity of the ion.

In electromagnetic ion beam manipulation, the strength of the electric and magnetic fields are loosely analogous to the refractive index of the glass elements of an optical lens. There are differences though. The deflection of a beam by an electromagnetic field can depend both on the energy of a particle, and its mass to charge ratio (m/q). Below is a simple derivation of a device which can disperse particles in m/q, while cancelling the velocity dependent parts of the electric and magnetic forces.

Here it will be assumed that a parallel beam of particles is deflected by thin electric and magnetic devices superimposed in space. The fields are perpendicular so that the forces are parallel. Each particle is described by a mass m, charge q and forward momentum p_p. The forces will be in the transverse direction resulting in transverse momentum p_t. All calculations are carried out in the non-relativistic

limit and for small deflections, such that $p_p = mv$.

The forces are,

Magnetic Terms: Electric Terms:

$$F_B = \frac{dp_{tB}}{dt} = qvB, \qquad F_E = \frac{dp_{tE}}{dt} = qE. \qquad [6.1]$$

If the duration of the impulse $\Delta t = \frac{L}{v}$, where L is the length of the device, then the resulting impulse Δp_t is given by,

$$\Delta p_{tB} = \frac{dp_{tB}}{dt}\Delta t = qvBL_B\frac{1}{v}, \qquad \Delta p_{tE} = \frac{dp_{tE}}{dt}\Delta t = qEL_E\frac{1}{v} \qquad [6.2]$$

This impulse deflects the particle by an angle θ, (small angle approximation)

$$\theta_B = \frac{\Delta p_{tB}}{p_p} = \frac{q}{mv}BL_B, \qquad \theta_E = \frac{\Delta p_{tE}}{p_p} = \frac{q}{mv^2}BL_B. \qquad [6.3]$$

Thus magnetic devices bend particles by an angle proportional to q/p, and electric by q/T, where T is the kinetic energy.

Now when the two fields are superimposed, the angle of deflection is just

$$\theta = \frac{q}{mv}BL_B + \frac{q}{mv^2}EL_E. \qquad [6.4]$$

It is clear that with static fields there can be no electromagnetic separation of particles of identical m/q, so we define $x = m/q$. Now consider a group of particles with a small spread in velocities and mass to charge ratios. Define

$$\delta_v = (v-v_o)/v_o \quad \text{and} \quad \delta_x = (x-x_o)/x_o. \qquad [6.5]$$

If Equation 6.4 is expanded to first order in δ_v and δ_x, then

$$\theta = \frac{1}{x_o v_o^2}\left[v_oBL_B(1-\delta_x-\delta_v) + EL_E(1-\delta_x-2\delta_v)\right]. \qquad [6.6]$$

Case 1: If $EL_E = -v_o BL_B$ then $O(\delta_x) \to 0$ and only $O(\delta_v)$ remains[5]. This device distinguishes particles of different velocities, independent to first order of their m/q. It was first described by Wien and is thus usually called a Wien filter. All particles with $v = v_o$ pass through undisturbed, and $\theta \sim \delta_v$.

Case 2: If the magnetic field is doubled so that $2EL_E = -v_o BL_B$, then $O(\delta_v) \to 0$ and $O(-\delta_x)$ remains. This provides separation in x, independent of velocity to first order. $\theta \sim (1-\delta_x)/2$ so that all particles of the same x are deflected by the same amount.

For an isotope separator to separate particles in such a way that once they come to rest they are physically separate, it needs to disperse them in position, not just angle. This can be accomplished with the addition of lenses which establish a point-to-parallel condition at the beginning of the device, and the reverse - parallel-to-point - at the end. With theta zero following the first lens, the final deflected position y at the end is just the sum of the products of the various angular dispersions and their distances from the final focus;

$$y = \sum_i \Delta y_i \sim \sum_i \theta_i d_i . \qquad [6.7]$$

VI.2 Design and Construction:

In the simple model of Section VI.1, a device which separates particles according to m/q - independent of velocity - can be built if the dispersion

$$D_i = \frac{\partial \Delta y_i}{\partial v} = d_i \frac{\partial \theta_i}{\partial v} \qquad [6.8]$$

5. $O(\delta)$ indicates terms of order δ.

due to the magnetic field is twice that of the electric field. When the RPMS was constructed, a velocity filter ($E = v_o B$) was available on loan from the Lawrence Berkeley Labs. It was used as a meson separator at the BEVALAC. The device consists of a set of electrostatic plates oriented one above the other, providing a vertical electric field. Coils are included to generate a horizontal magnetic field in the same volume. Since the plates are 5m long and are separated by only 10cm, the device is best utilized when the electric and magnetic forces almost cancel, and the particles pass straight between the plates without deflection. This condition is satisfied in Case 1 of Section VI.1, for a velocity filter. The angle of deflection is proportional to δ_v, and is zero for $v = v_o$ where $E = v_o B$. To make a mass separator at NSCL, a magnetic dipole was added, following the Wien filter, which provides a term proportional to $(1 - \delta_v - \delta_x)$. This cancels the velocity dispersion, and provides dispersion in mass-to-charge ratio. A magnetic quadrupole doublet near the front of the RPMS following the target provides a parallel beam for the Wien filter and dipole, and a second doublet refocuses the parallel envelopes of each m/q to different vertical positions after the dipole. The second quadrupole doublet and detector system are all mounted on a tail platform which pivots up from horizontal about the center of the dipole magnet. This allows the experimenter to move the detectors and intercept different m/q isotope groups, while the dipole field and Wien filter fields remain fixed. The RPMS is illustrated in Figure 6.1. More can be learned about the RPMS in NOLEN84 and the upcoming PhD thesis of HARKEWICZ.

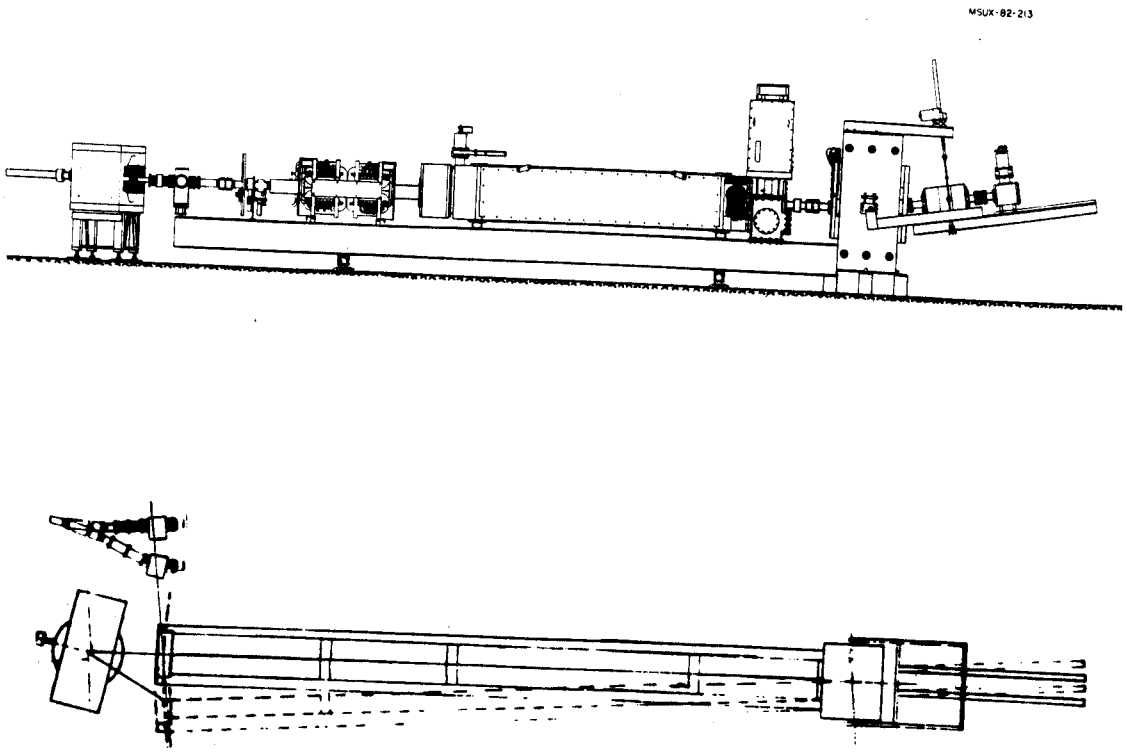

Figure 6.1 Illustration of the Reaction Product Mass Separator; a) side, and b) top. b) illustrates that changes in scattering angle are facilitated by only small rotations of the RPMS about the center of the Cornell magnet.

VI.2.1 Phase-Space Acceptance:

The RPMS is equipped with four selectable apertures to constrain the particles to certain envelopes. The three momentum dimensions are represented by velocity and vertical and horizontal scattering angle (phi, theta). The three spatial dimensions are represented by the vertical and horizontal position at the target plane, and position of the target location along the axis of the RPMS. This last dimension is essentially fixed for thin solid targets.[6]

The first device to limit the envelope of particles to be separated is called the 'half-aperture.' It is a thick block of metal whose top surface cuts across the center of the optical axis of the front of the RPMS, about 80 cm downstream from the target. This axis is the extension of the beam-line axis, passing through the center of the beam-spot on the target and through the axis of the first quadrupole doublet of the RPMS. The only particles which can pass by this half-aperture are in the upper half plane - only those with a vertical scattering angle greater than 0°.

The second device is the solid-angle defining aperture. There are five of these in a vertical ladder, roughly 120 cm from the target. The apertures define the shape of the envelope of the particles entering the

6. This was not the case when a gas target was used (GIL88). A chamber filled with Helium gas was used as a target, and was 10cm in length. In this case, the sixth element in phase space occupied by the reaction products was also extended. This could have a significant effect on the resolution of the RPMS, because the first quadrupole doublet will produce a parallel envelope within the RPMS only if the particles emerge from the focus; a point on the axis which is appropriate to their velocity.

first quadrupole doublet. One can choose either a small solid angle, which has limited phase-space and should provide better overall m/q resolution, or a large solid angle which accepts more phase space and thus gives a higher count-rate. Particles near 0° can be eliminated with an annular aperture, which blocks the center while allowing those particles scattered to larger angles to pass. Four apertures have been used to date: 4°×2°, 2°×1°, 2°×1/2°, and 1°×1/2°, (horizontal × vertical).

It is important to point out that there is a vertical offset in the axis of the RPMS between the first quadrupole doublet and the Wien filter. The center of the Wien filter is 2 inches above the axis of the doublet, so that it is coaxial with the center of the upper half-plane of the doublet. This offset, coupled with the half-aperture, makes use of the large 8 inch diameter of the first quadrupole doublet in order to reduce the effect of the chromatic aberration in the size of the final image at the end of the RPMS. For a fixed m/q dispersion, the size of the image determines the resolution of the device and thus its ability to separate isotopes with nearby m/q.

The third element is a pair of jaws between the Wien filter and Cornell magnet which move in the vertical direction. Since the envelope is parallel here, the vertical position of the particle is correlated not only with the velocity, but with the vertical scattering angle. Thus these jaws can not actually select a particular velocity, but can only impose a triangular envelope in velocity space.

Finally, the fourth device consists of a pair of horizontal and vertical slits, usually found directly in front of the detectors after

the last quadrupole doublet and the window separating the vacuum from atmosphere. The vertical slits are used to define the m/q distribution which passes into the detectors, and is the functional device in the physical separation of the isotopes. They are placed so that the center of each pair of slits corresponds the center of the detector, and also to the image of the isotope of the desired m/q. m/q is then adjusted by the motion of the entire tail of the RPMS. The vertical slits can be widened to allow more values of m/q to enter the detector while tuning up, then narrowed to allow only one isotope or a few isotopes to enter the detector when a decay measurement is underway.

VI.2.2 Scattering Angle:

Some experiments demand operation at a non-zero scattering angle - typically 2° to 5°. The scattering angle of the RPMS is defined as the angle between the optical axis of the RPMS and the direction that the beam would travel if it continued through the target. A scattering angle of 0° and a thin target would allow the beam to travel directly down the axis of the RPMS and possibly strike one of the electrostatic plates within the Wien filter.

The most trivial way to change the scattering angle is to pivot the entire RPMS about the target. However this would require the 12m length of the RPMS would subtend too much floor space. Instead, the RPMS is held fixed at one point (the center of the Cornell Dipole) about which it is rotated by a few degrees. An inflector magnet is introduced in the beam-line just before the target. The incoming angle of the beam, position of the magnet, and small back and forth motion of the RPMS are

chosen so that at a deflection of the beam by the inflector magnet of -15° allows the beam to strike the target at a scattering angle of 0°, and a deflection of +15° gives a scattering angle of slightly over 30°. A diagram of the RPMS as viewed from above is shown in Figure 6.1b.

VI.3 Beginning a Typical Experiment:

VI.3.1 Start-up Procedures:

The start-up procedure for an experiment with the RPMS is of a tedious and technical nature, and involves details specific to the RPMS in its present configuration. The RPMS is presently being reconfigured for Phase II operation at NSCL, and thus this information is not given here. The interested reader is directed to the future dissertation of HARKEWICZ, and to the RPMS users handbook to be completed in late 1990. The procedure outlined is designed to obtain some count rate of near-stability isotopes from a 'cold start,' without ever presenting the silicon detectors or position sensitive proportional counter with a high count-rate of particles that might damage them.

Once a variety of particles are reaching the telescope, one should try to identify the particles with the on-line analysis program - traditionally SARA. First, a two-dimensional histogram of ΔE (vertical) vs. E will give some indication of what particles are reaching the detectors. Identification can not be certain from just this histogram alone. Next, a one-dimensional histogram of the function PID (ΔE, E) (Section VIII.4.1) should be displayed and compared to the plot of ΔE - E. Small changes in the dipole current will bring different isotopes in and out of view this way, and one could in principal learn something about the

particle identification by trial and error. However, a simpler method exists.

A position-sensitive gas proportional counter should be used to measure the vertical position of the particles reaching the focal plane. The detector that has been used to date is described in CURTIN85 and ORMAND84. A new detector which can be operated in vacuum is under construction. See MIKOLAS88b and HARKEWICZ89. It is useful to monitor a two dimensional histogram of vertical position (Y) vs. PID (X). A map of all particle stable light isotopes which can be made by the fragmentation of a ^{22}Ne beam is shown in Figure 6.2 for reference.

Tuning of the RPMS continues with a histogram of vertical position vs. energy, gated on only one isotope. If the dipole is set too low, and is not completely cancelling the velocity dispersion of the Wien filter, the particles of higher velocity (and therefore energy) are below those of lower velocity. If the dipole is too high, the opposite case is true. When set correctly, the correlation between velocity an position is completely cancelled.

When the RPMS is tuned properly, isotopes should appear as small groups in a histogram of position vs. PID. However, it may not be immediately obvious <u>which</u> isotopes are being observed. One must 'move around' in m/q space and in velocity space to reach the desired m/q and optimize the yield. When moving in m/q space, it is helpful to remember the 'holes,' those isotopes which are not themselves stable, but the isotopes with one more and one less neutron are stable. Some of these are ^{5}He, ^{7}He, ^{10}Li, ^{8}Be, ^{13}Be, ^{9}B, ^{16}B, and ^{18}B.

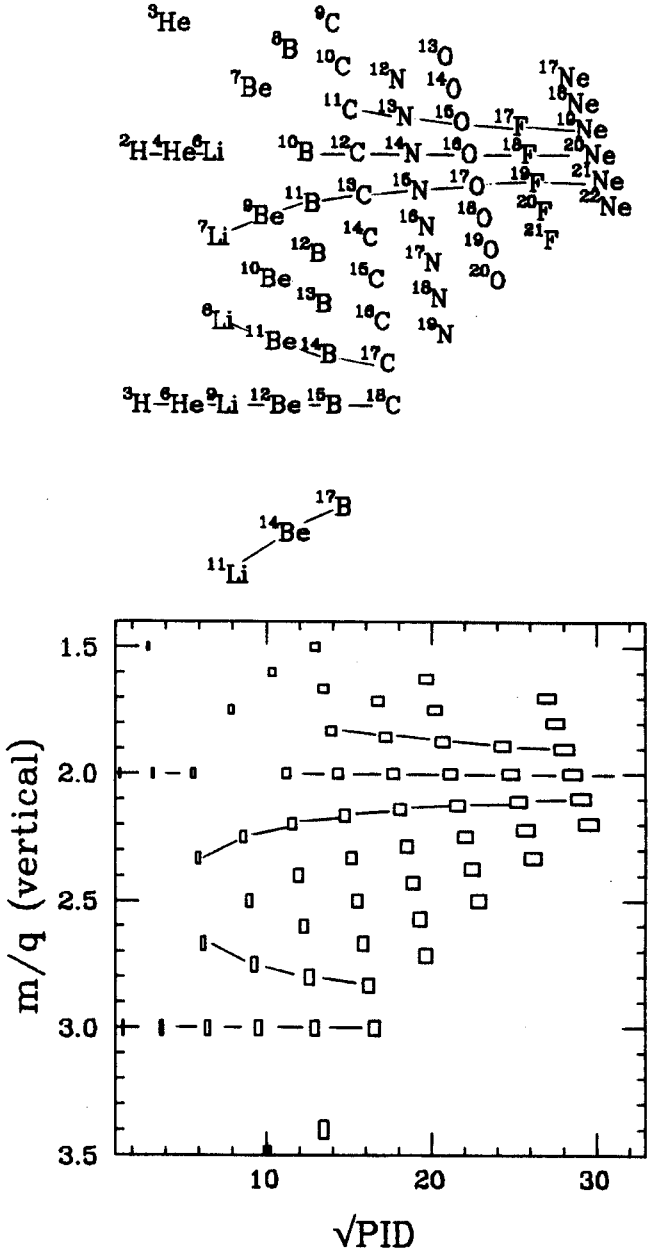

Figure 6.2. Schematic representation of a histogram of vertical position as a function of the square root of the Particle Identification function (PID.) The square root of PID is used for the horizontal axis in order to keep the groups more evenly spaced. The boxes represent typical resolutions in m/q and in PID.

VI.3.2 Tuning Up:

While an experiment begins with some initial settings, either from a previous run or from a calculation based on calibrations of the various settings of the components of the RPMS, simple scaling laws can be used to move from one set of settings to another. There are four quadrupole field strengths, two magnetic dipole fields and an electric dipole field, and the angle of the tail. Scattering angle, slit position and target height and angle are adjusted less frequently.

Once point-to-parallel-to-point conditions have been established, (somewhat different optical conditions may be used for special cases), the quadrupole magnets should be scaled as a unit, with their fields proportional to the magnetic rigidity, p/q. Thus they are linear in both v and m/q in the non-relativistic limit. The ratio of magnetic to electric fields in the velocity filter is varied only when changing velocities. The relation,

$$E = -v_0 B \qquad [6.9]$$

must be held, so that E/B is linear in velocity, and independent of m/q. In order to maintain zero dispersion in velocity, the field in the dipole must always follow the magnetic field in the velocity filter. It has been simplest experimentally to keep the power supplies for the high voltage field in the Wien filter fixed. They have usually been kept fixed at the highest voltage obtainable without sparking in order to maximize the dispersion. When this is the case, the two magnetic dipole fields must always be set in the same ratio, which is determined by the velocity. Changes in m/q are simply changes in the quadrupoles, and in the tail angle.

Non-relativistic scaling laws for three parameters - m/q, velocity, and dispersion - are discussed below. They are also summarized in Table 6.1 for quick reference. Here, B_c represents the field in the dipole (obtained from Cornell University), B_w and E_w are the magnetic and

VI.3.2.1 Scaling in m/q:

When the RPMS is functioning to separate isotopes, they are dispersed in position at the final focal plane with the smaller m/q isotopes deflected further up than the heavier ones. Simply moving the tail down will increase the value of m/q which can pass through the slits and enter the detectors.

However, when the m/q is increased the isotopes are also more rigid and therefore difficult to focus. Thus the quadrupoles must then be increased to maintain the same envelope within the Wien filter and dipole, and bring them back to a focus. Therefore the quadrupoles scale linearly with m/q and the tail angle inversely.

VI.3.2.2 Scaling in velocity:

From Equation 6.9 it is clear that there are two independent ways to change the center of the velocity band-pass of the RPMS - to vary E_w proportional to velocity, and to vary B_w and B_c together inversely to velocity. In order to maintain the same m/q at the same vertical position, only the second choice will work. Since

$$\theta_t \sim \frac{B_c}{(m/q)\, v} , \qquad [6.10]$$

B_c must decrease if m/q and θ are to remain constant while velocity decreases.

Table 6.1. Scaling Exponents[7] for RPMS Settings. Q_{20} through Q_{23} represent the four quadrupole magnets, B_c the Cornell Dipole, E_w and B_w the electric and magnetic fields in the Wein filter, and θ_{tail} the angle of the tail with respect to the axis of the Wein filter.

Device(s)	Parameter(s)	m/q	v	D
Quadrupoles	Q_{20}, Q_{21}, Q_{22}, Q_{23}	+1	+1	0
Tail Angle	θ_{tail}	-1	0	+1
Magnetic Dipoles	B_w, B_c	0	-1	+1
Electric Dipole	E_w	0	0	+1

7. For example, to scale the magnetic field in the Wien filter, B_w, from its previous value which produced $(m/q, v, D)_{old}$ settings to new settings which give $(m/q, v, D)_{new}$, use the relation:

$$\frac{Bw_{new}}{Bw_{old}} = \left(\frac{m/q_{new}}{m/q_{old}}\right)^{0} \times \left(\frac{v_{new}}{v_{old}}\right)^{-1} \times \left(\frac{D_{new}}{D_{old}}\right)^{+1},$$

As with m/q scaling described in the previous Section, the quadrupoles must also be varied with the magnetic rigidity and therefore velocity.

VI.3.2.3 Scaling in Dispersion:

Here the velocity and m/q are to remain fixed, and only the separation between various groups of m/q (and thus tail angle) is to be varied. This means that the quadrupoles are not varied.

With the relationship in Equation 6.9 maintained, there is still one degree of freedom. E_w , B_w , B_c, are varied together, proportional to dispersion D. When B_c is raised, and m/q and velocity are fixed, then the tail angle must also increase.

VI.4 Monochromation:

In both half-life determinations and beta-delayed charged particle spectroscopy the broadness of the distribution in ranges of the particles in the silicon detectors is often a limiting factor. The suppression of sensitivity to unwanted activity can be accomplished through the use of differential ranges described in Section VII.2.1. In delayed charged particle spectroscopy the detector usually must be much thinner than the spread in ranges of the isotope of interest in order to limit the contamination from the beta particle (Section VII.3.4). Both of these experimental situations can benefit greatly from a reduction in the spread of range distributions.

In order to compress the range distribution, the RPMS is first tuned to a momentum focus as described in Section VI.3.1. This gives a spot size for a given isotope of approximately 4 mm at the detector. The dipole current and tail angle are adjusted slowly together so that

the mv/q dispersion of the dipole is varied while the average m/q reaching the detector remains fixed. This 'detuning' introduces a mis-match between the velocity dispersion of the dipole and that of the Wien filter, and the particles with higher velocity end up above those with lower velocity. The image is now enlarged vertically, and the dipole should be de-tuned until the maximum aperture of the telescope is filled - typically 20 mm for a standard 300 mm^2 silicon surface barrier detector. The vertical vs. energy histogram will now show a clear correlation between position and energy, with a resolution of 4/20 or 20%. A graded absorber is then introduced having a thickness which increases with vertical position. The gradient of the thickness is chosen to compensate for the larger velocity (and range) of the ions entering the top of the absorber so that the velocity (and range) of those exiting are compressed before entering the silicon. This distribution is narrower, and can place those ions which would normally fill 250 μm of silicon into one detector only 50μm thick. The reduction of the spread in energies of the particles passing through the degrader is referred to as monochromation.

This was a particularly useful technique in the case of ^{8}He decay. The range of the ^{8}He fragments collected by the fragmentation of a ^{22}Ne beam by a target just thick enough to stop the beam is roughly 5 mm. The experiment required the thickness of the detectors to be under 50 μm, only a few percent of the spread in ranges of the ^{8}He's collected! While many detectors of 50 μm thickness could be placed in series, the efficiency could approach 50% only by careful monochromation of the ^{8}He's.

Since the compression is accomplished by a deliberate degradation of the m/q resolution, this technique is limited to very light isotopes, such as those of helium through Boron - where the distance in m/q space is large from one isotope to the next of a particular element. Ideally a self-contained system could be added to the RPMS following the m/q selection by slits at the focal plane. This then would prevent the momentum dispersion from degrading the m/q separation.

SECTION VII

VII. General Experimental Considerations:

There are at least three general questions which one must address when choosing experimental conditions at the target location. The first question is the choice of which target material will be used and what thickness it will be. The second question is which beam particle to use and at what kinetic energy. The third question is at what scattering angle will the fragments be collected. However, before these can be answered a brief discussion of the projectile fragmentation reaction is necessary.

VII.1. Projectile Fragmentation:

The dynamics of nuclear reactions are complex and beyond the scope of this dissertation. However with the goal of the optimization of a production rate of a given isotope in mind, it is helpful to consider a few qualitative features of projectile fragmentation. It is important to note that projectile fragmentation is ascribed to processes which take place at relativistic energies (many hundreds of MeV per nucleon) and that it is not obvious that they should occur at energies presently available here at NSCL (30 to 50 MeV per nucleon.) Review of experimental data representing projectile fragmentation at relativistic energies are given in GREINER75 and VIYOGI78, and at lower energy by CASKEY88. Theoretical discussions are given in GOLDHABER74, OLIVEIRA79, and MORRISSEY79, and reviews of fragmentation processes by GOLDHABER78, HUFNER85, FRIELANDER87 and LYNCH87. Reviews of reactions which lead to the production of nuclei far from stability can be found in WESTFALL79, WOODS85 and ROECKL88.

The process of projectile fragmentation shows several

characteristics which are distinct from other processes. The fragments of the beam nucleus continue to move forward with nearly the beam velocity. There is usually a spread in velocity and direction compared to the incident beam. This can be almost completely described by a Gaussian spread in momentum in all directions with the centroid at the beam momentum-per-nucleon. Often a slight shift to lower momentum in the lab is observed, and can be explained as a 'frictional' type of energy loss as bonds in both nuclei are broken.

The width of the distribution in momentum increases with the number of nucleons which are removed. In the model of GOLDHABER74, this spreading can be thought of as the sampling of the Fermi momentum of the individual nucleons. In the frame of the projectile with nucleon number A_p, the momentum of all of the nucleons sum to zero. If suddenly n nucleons are removed so that a fragment with nucleon number $A_f = A_p - n$ is produced, that fragment must have a recoil momentum -p, where,

$$p = \sum_{i=1}^{n} p_{fermi}(i). \qquad [7.1]$$

in order to maintain a total momentum of zero in this frame. In this approximation the momentum of each nucleon in a given direction is a Gaussian distribution and uncorrelated to the motion of all other nucleons, except that the total momentum of all nucleons in the nucleus sums to zero. Thus the distribution P of momentum in a given direction (longitudinal used here) is

$$P(p_z) = \frac{1}{\sigma\sqrt{2\pi}} e^{-\frac{p_z^2}{2\sigma^2}}. \qquad [7.2]$$

They show that for a simple situation where nucleons are suddenly removed at random, σ can be obtained from,

$$\sigma^2 = \sigma_0^2 \frac{A_f(A_p - A_f)}{A_p - 1}, \qquad [7.3]$$

where

$$\sigma_0^2 = \frac{\langle p_n^2 \rangle}{3} = \frac{p_{fermi}^2}{5}. \qquad [7.4]$$

A typical value for $\sigma_0^2 c^4$ which reproduces the fragmentation data at relativistic energies is 80 MeV. At lower energy the value which provides the best fit to the data is larger. This is most likely due to a breakdown of the model. In slower collisions other processes can occur which can absorb a significant amount of kinetic energy. CASKEY88 indicate that while values of $\sigma_0^2 c^4$ of 50 to 100 MeV reproduce the high-energy part of the spectrum, a long low energy tail seems to be generated by other processes. Rough examination of the published spectra indicates that a value for $\sigma_0^2 c^4$ of 100 MeV will reproduce the FWHM of the energy distribution of fragments where three nucleons are removed. This value will be used in all further calculations as a simple way of simulating a representative momentum distribution only.

The cross-section for a particular isotope is difficult to calculate, but as pointed out by WESTFALL79 and LYNCH87 it seems to be fairly independent of the particle which induces the fragmentation (the target nucleus in the case of projectile fragmentation.) Immediately after the fragmentation event the fragment cools and relaxes to

(nearly) some ground state configuration predominantly by the evaporation of nucleons and light nuclei (e.g. alpha particles). Far from stability, the separation energy of the type of nucleon in excess is usually much lower than that of the other type, and thus the evaporation tends to bring the fragment closer to the stability line. The measured yields of a given isotope are therefore quite removed from the primary yields of the fragmentation process.

It is important to stress that fragmentation is not necessarily the ideal name for the dominant processes which produces nuclei far from beta stability which continue close to the frame of the beam. Deeply in-elastic and particle transfer processes may significantly contribute to yields from reactions at 30 to 50 MeV per nucleon and no data exists at present which could clearly distinguish contributions from these processes. (See section VII.2.1)

VII.2 Target Parameters:

VII.2.1 Choice of Target Thickness:

There are two opposing factors which must be balanced when choosing a target thickness. First, the production rate of a given isotope in the target monotonically increases with target thickness until the beam has lost so much energy that it is below the threshold for the production of that isotope. Second, the energy loss of the fragments tends to spread them out in energy, since the lower energy fragments loose energy faster than the higher energy fragments. In order to better understand the yield of fragments from a thick target, a simulation routine was written which models the production and energy loss of

fragments in a given target. Simple assumptions are made wherever possible to reproduce the important behaviors of the various phenomena such as the spread in momentum from the reaction, energy loss in the reaction (friction), beam energy dependence of the cross-section, and energy loss of both the projectile and the fragment in a thick target.

In thick targets, the projectiles have a different velocity at each location in the target. When a fragment is produced, it continues to loose energy at a new rate until either it comes to rest in the target or leaves the target. The calculation provides for a loss of total kinetic energy of the projectile at the beginning of the fragmentation before nucleons are removed or momentum is transferred as a simple way of including losses to friction. In practice this is set to zero, as this seems to give general agreement with the data of CASKEY88.

The energy dependence of the cross-section is unknown. At relativistic energies it seems to be constant and fairly independent of entrance channel, however incidental information at lower energy indicates that the cross-section for nuclei far from stability significantly increases between 25 and 40 MeV per nucleon.

In order to simulate some sort of dependence of the production rate on beam energy a simple power-law parameterization of the production rate as a function of beam energy above some threshold,

$$\frac{dN(E)}{dE} \approx \begin{cases} \frac{1}{C}\left(E-E_{thresh}\right)^{q} & E > E_{thresh} \\ 0 & E \leq E_{thresh} \end{cases} \qquad [7.5]$$

where q is some exponent chosen to best represent whatever data might be available. q = 0 implies a rate independent of energy above threshold, while q = 1 implies a rate proportional to energy above threshold. C is a normalization constant given by,

$$C = \int_{E_{thresh}}^{E_{beam}} \frac{dN(E)}{dE}\, dE \qquad [7.6]$$

In this chapter E always represents the kinetic energy per nucleon. If the projectile remains in the target at all times when its energy is between E_{beam} and E_{thresh}, the probability is 100% that the simulation will deliver a fragment. The production rate N can then be scaled to a known cross-section at one or more energies when these become available.

For each event, a location in the target is chosen at random in order to reproduce the behavior as given in Equation 7.5. The beam momentum per nucleon is calculated at that point in the target through the simple range-energy relations,

$$R(E) = C_R \frac{A_p}{Z_p^2} E^p, \qquad [7.7]$$

$$E(X) = \left(\frac{[R(E_{beam})-X]\, Z_p^2}{A_p\, C_R}\right)^{1/p}, \qquad [7.8]$$

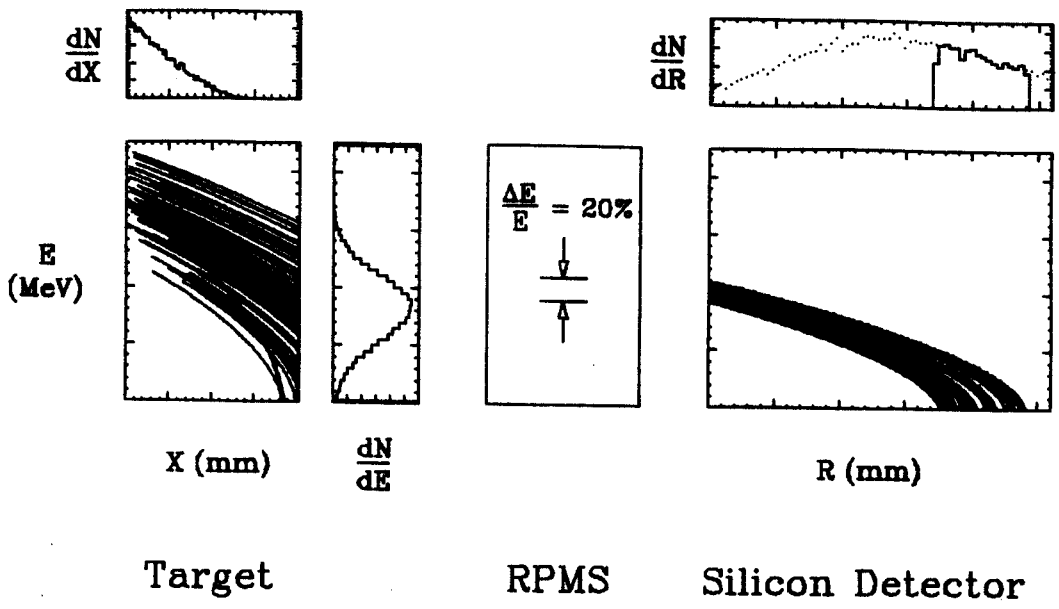

Figure 7.1 Illustration of various spectra generated by the Monte Carlo simulation discussed in the text. Rays represent the energy of fragments in the target and detector as a function of depth of penetration. Bold line represents the primary beam. dN/dX represents the rate of production per unit thickness in the target, dN/dE is the rate of emission per unit energy from the back of the target. R is implantation range in the silicon detector, and dN/dR is the rate of implantation per unit thickness in the silicon.

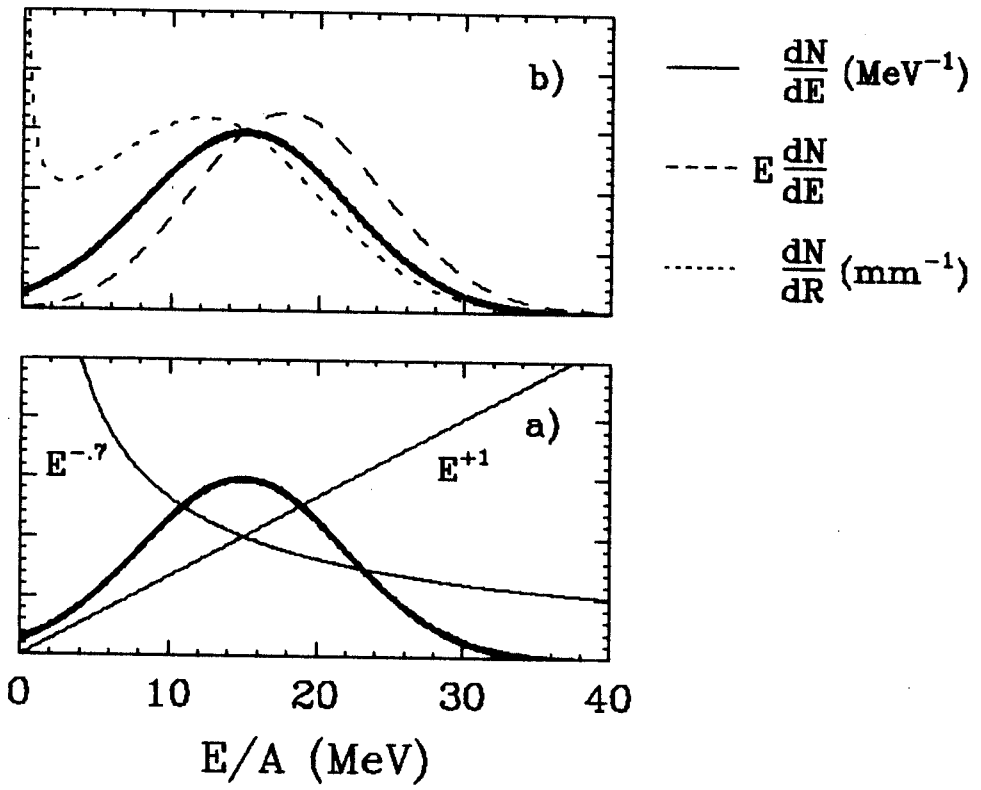

Figure 7.2 Simple illustration of various rates considered in the text. a) Gaussian distribution (bold) and two weighting functions E^{+1} and $E^{-0.7}$. b) Same Gaussian distribution and weighted distributions.

where C_R and p are chosen to reproduce tabulated or measured ranges over the region of interest. X is the depth in the target as measured from the front and E is always the kinetic energy per nucleon.

Once a location has been chosen, the fragment (A_f,Z_f) is introduced with a forward momentum as described by Equation 7.2, centered at the beam momentum per nucleon. The energy upon exiting the target, or location in the target at which the fragment stops are then determined from Equations 7.6 and 7.7.

A schematic representation of this process distributions of the beam and resulting fragments is shown in Figure 7.1 for a typical projectile fragmentation-like reaction near 35 MeV per nucleon. The lighter fragments with a smaller nuclear charge (Z) than that of the beam have a smaller energy loss per unit thickness (dE/dX), and therefore loose energy at a slower rate than does the beam. For the thinnest target the fragments leave the target with a velocity only slightly lower than the beam. However, as the thickness increases the beam loses energy more rapidly than the lower Z fragments, and soon is decelerated far below the velocity of the fragments. The RPMS has typically been run with a target just thick enough to stop the beam.

As illustrated in Figure 7.1, the RPMS has an acceptance window in energy of roughly 20%. The count rate at the detector following the RPMS is sensitive only to that part of the yield which is within this window. The size of the window is fixed in relative energy, not absolute. Therefore the yield per percent energy is more important than yield per MeV. The difference is illustrated in Figure 7.2. Here a simple Gaussian is used to represent the energy spectrum of fragments.

When the Gaussian is multiplied by the straight line shown in 7.2a, the resulting function E dN/dE [= dN/d(ln(E))] reaches a maximum at a slightly higher energy that does dN/dE itself. In order to maximize the count rate at the focal plane a device with a fixed relative energy band-pass such as the RPMS would be tuned above the peak yield in the energy (dN/dE) spectrum.

As discussed in later sections, beta-delayed particle spectroscopy often requires the implantation of the fragments in a thin silicon detector. Here thin means much narrower than the range distribution of the fragments at the focal plane after transmission by the RPMS. In this situation the count rate per unit range should be optimized. Using,

$$\frac{dN}{dR} = \left(\frac{dN}{dE}\right) / \left(\frac{dR}{dE}\right) , \qquad [7.9]$$

and Equation 7.7,

$$\frac{dN}{dR} = E^{1-p} \frac{dN}{dE}. \qquad [7.10]$$

A value of p near 1.7 is typical, and thus $E^{-0.7}$ and $E^{-0.7}$dN/dE are also included in Figures 7.2a and 7.2b respectively. Once again the distribution differs considerably from the original Gaussian, only this time the RPMS should be tuned LOWER than the location of the highest count rate in order to maximize the rate of implantation in a thin detector. The singularity at very low energy disappears if instead of plotting a differential quantity one integrates over a detector of finite thickness ΔR.

In Figure 7.3 a series of target thicknesses have been used to calculate the various count rates for two reactions. The outgoing energy of beam particles which do not undergo a reaction is illustrated

for comparison. In the left group neutron-rich fragments leave the target with half of the energy per nucleon of the original beam when the target is sufficiently thick to stop the beam. In the right group neutron deficient fragments slow down quicker than the primary beam and fail to emerge from a target which is thick enough to stop the beam. In Figure 7.4 the results of these simulations are summarized. For each reaction, location of the peak of each of the three distributions are given in the lower graphs while the heights of the peaks are shown in the upper graphs. It is clear that the count rate per MeV, and per percent energy are optimized with targets which are slightly less than half as thick as the range of the beam, while the count rate per unit final range implanted in silicon is fairly flat and shows a gradual maximum at a target thickness near the range of the beam. It is also clear that targets just thick enough to stop the beam produce a rate which are within a factor of two of the optimal rate.

While a certain count rate may be optimal with a thinner target, it is often helpful to stop the beam in the target for other reasons. If it passes beyond this point, it can activate other components of the RPMS (make them radioactive) and it can scatter from the plates of the Wien filter and other surfaces within the RPMS, so that a small fraction of scattered beam and induced secondary particles reach the detectors without proper trajectories. However for some reactions such as $^{16}O \rightarrow {}^{13}O$, $^{12}C \rightarrow {}^{9}C$, the fragments have a shorter range than the primary beam and therefore both must be allowed to pass through the target. The beam which passes through the target may still be

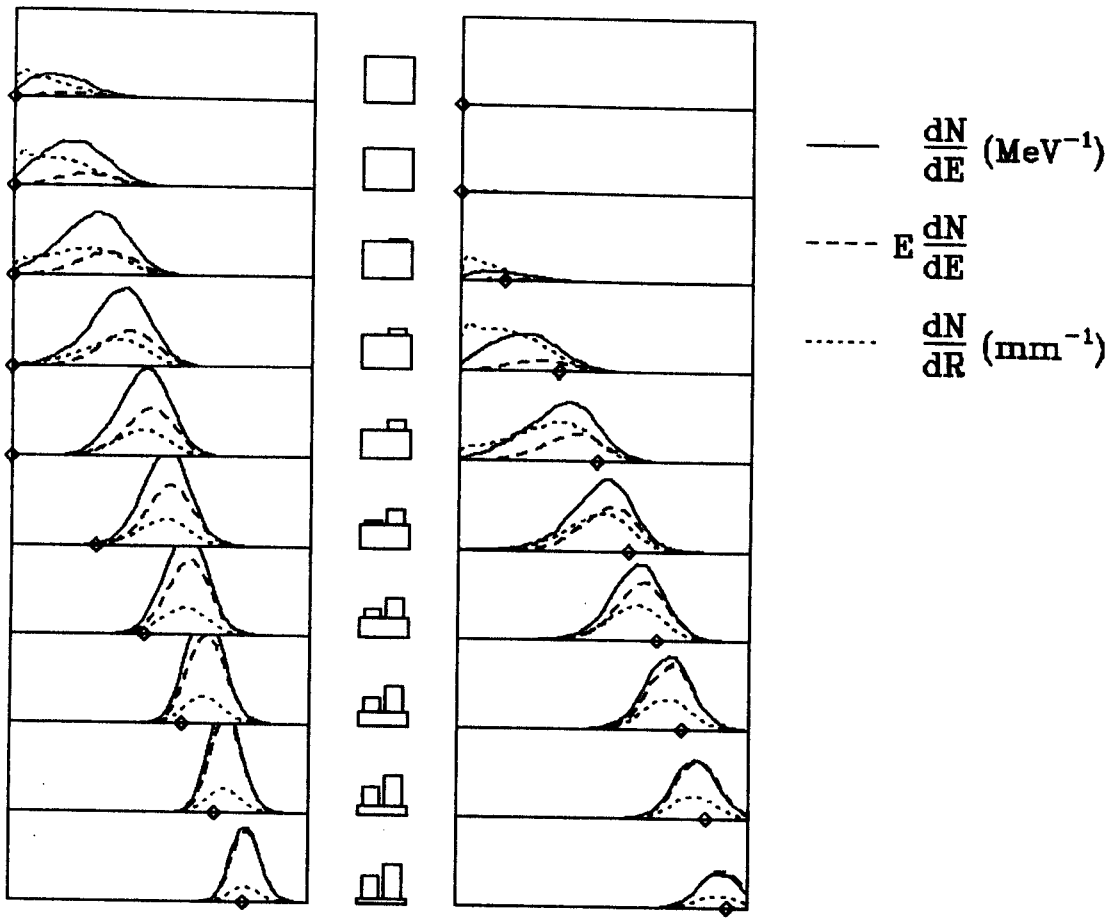

Figure 7.3 Series of simulations of distributions of fragments as a for increasingly thick targets. Left and right groups correspond to the two reactions shown in Figure 7.4 (next page). In the center column, the wide rectangle of variable height represents the target thickness, while the two narrow rectangles behind the target represent the (fixed) range of the beam with respect to the target thickness. When the target rectangle just covers the narrow rectangle, the target is just thick enough to stop the beam. The diamonds represent the remaining energy of the beam after passing through target. Target are multiples of 0.0025 inch thick Ta.

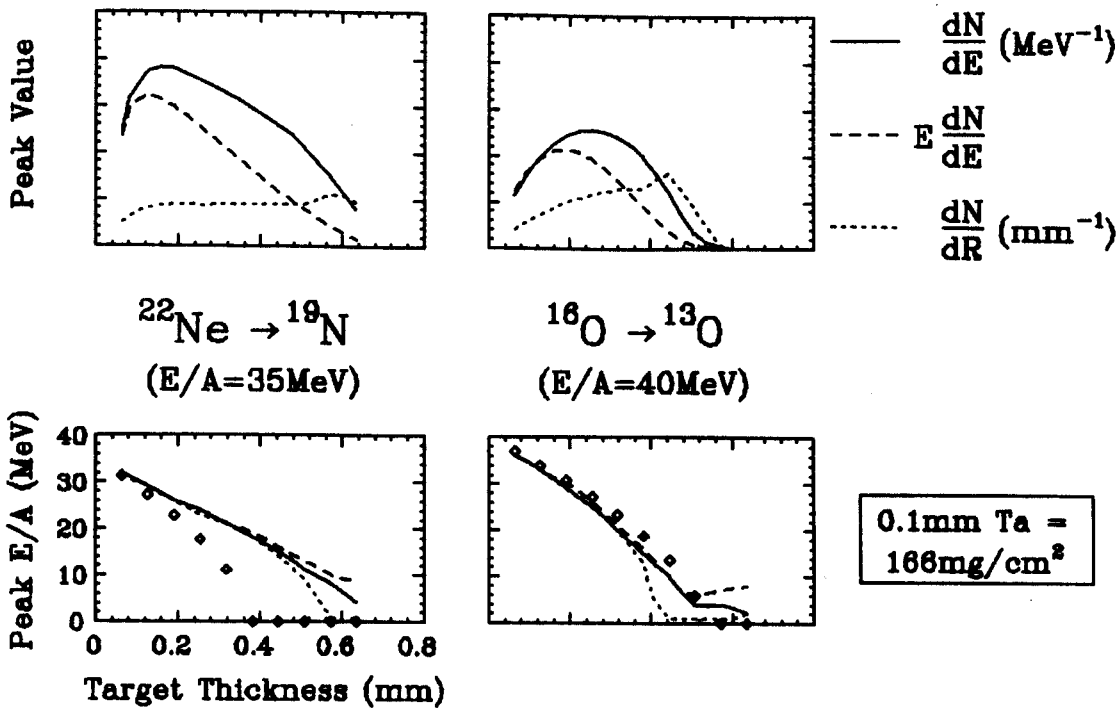

Figure 7.4 Peak heights and peak locations for those distributions in Figure 7.3 (previous page) as a function of target thickness. As stated in the text, E is kinetic energy per nucleon.

prevented from entering the RPMS by moving away from a scattering angle of 0°.

VII.2.2 Scattering Angle:

While operation at a scattering angle (Section II.1.2) of 0° is usually desirable, (the fragmentation yield is most likely a maximum here), it is sometimes necessary to use a thinner target. One can then take advantage of the angular spread of fragments from the reaction to help separate the primary beam from the fragments of interest. While this is very dependent on initial and final energies and the number of protons and neutrons removed, it is safe to say that the distribution at 35 MeV per nucleon is fairly flat over many degrees, and for more violent collisions and heavier target nuclei may extend past 5° before a significant drop in cross-section is observed. If the scattering angle of the RPMS is moved away from 0° the beam can be prevented from entering the RPMS while the rate of fragments entering may remain nearly constant.

The angular distribution of beam particles leaving the target is a function of two things, the divergence of the beam striking the target and the scattering of the beam within the target. The divergence of the beam is physically limited by the ratio of the 10 cm diameter aperture of the last quadrapole of the beam-line before the target to the roughly 2.5m distance between it and the target. Thus the half-angle of the incident cone can be no more than 1°.

The scattering of the beam within the target is a statistical process. Multiple small-angle (large impact parameter) coulomb scattering with the nuclei in the target can scatter a small fraction of

the nuclei many degrees. Since multiple coulomb scattering is statistical in nature, the RMS spread should behave like the square-root of the target thickness. On the other hand, the shape of the distribution due to occasional large-angle scattering from single small-impact-parameter collisions is independent of the target thickness, while it's intensity varies linearly with thickness. While this process is difficult to model explicitly because of the statistical nature of the process and uncertainties in the exact screening effects of the atomic electrons upon the nuclear coulomb potential, it can be estimated by,

$$\theta_{rms} = \frac{14.1\ MeV}{\beta\ pc^2} Z_{inc} \sqrt{L/L_R}\ [1 + \frac{1}{9} \log_{10}(L/L_R)], \qquad [7.11]$$

where Z_{inc} is the charge of the incident particle, p is its forward momentum and L/L_R is the thickness of the foil in radiation lengths. Equation 7.11 was taken from the Partice Properties Data Booklet, AGUILAR-BENITEZ88. For Be, Si and Ta the radiation length is 35.3, 9.36 and 0.41 cm respectively, others can be found in various compilations. The equations,

$$pc^2 = A \sqrt{E^2 + 1863\ E}\ , \qquad [7.12]$$

and

$$\beta = \frac{pc^2}{E_{tot}} \qquad [7.13]$$

are helpful. Here E_{tot} is the total energy of the particle

$$E_{tot} = A\ (931.5 + E), \qquad [7.14]$$

and as always E is the kinetic energy per nucleon.

For a typical target of thickness 0".015 used to stop a ^{22}Ne beam at 35 MeV per nucleon, the multiple scattering in the target

redistributes ^{19}N fragments produced in the front of the target by an RMS angle of 0.035 rad, or about 2°. For reference, the grazing angle is about 7°.

In a recent experiment where ^{16}O beam nuclei with a kinetic energy of 40 MeV per nucleon were fragmented into ^{13}O, thin targets were needed to allow the ^{13}O fragments to pass through the target. Operation at a scattering angle of 2° was possible with a Beryllium target (Z=4, $\theta_{grazing}$=0.6° lab), but the rate of scattered ^{16}O was too high for scattering angles below 5.5° when a tantalum target (Z=73, $\theta_{grazing}$=6.4° lab) was tested.

The yield of exotic isotopes from the projectile fragmentation reaction fills a cone with a half angle of at least 3° for E/A = 35 MeV ^{22}Ne on Ta even before scattering through a thick target. Since most of the primary beam leaves the target within a much smaller cone the goal of increasing the scattering angle of the RPMS is to avoid the high rate of beam particles with trajectories near 0°. The apertures of the RPMS are typically larger in horizontal angle than vertical. Since the scattered beam, and to a lesser extent the fragments drop in yield at larger angles, more solid angle can be obtained if the scattering angle is chosen in the vertical direction, where the width of the aperture is narrower.

A small permanent magnet dipole has been built, to be placed just before the target of the RPMS. The effect is a vertical downward deflection of the beam, and since the magnet is placed very close to the target, the deflection in angle involves little physical displacement of the beam-spot on the target. Since the acceptance of the RPMS is typically a factor of four smaller in the vertical direction than

the horizontal and extends from 0° only upward, a 1° downward deflection is sufficient to keep the primary beam out of the Wien filter, while maintaining most of the aperture of the RPMS illuminated by the roughly 3° cone of the reaction. A photograph of the completed assembly can be found in MIKOLAS88b.

The magnet provides a nearly flat field of 6 kG over a volume 2.0 inch tall, by 0.6 inch wide, by 2.1 inch long. This would result in a 1° deflection of a fully stripped beam of ^{22}Ne at E/A = 35 MeV. This can be calculated from the convenient formula

$$qB\rho = \frac{A}{299.9}\sqrt{E^2 + 2Em_o c^2}\ , \qquad [7.15]$$

when q is the charge state of the ion, B is the magnetic field in Tesla, ρ is the radius of curvature of the orbit in meters, E is the kinetic energy per nucleon in MeV, and $m_o c^2$ is the equivalent energy of the rest-mass in MeV. The constant 299.9 is actually the speed of light c in m/s times 10^{-6}.

VII.2.3 Target Material:

The choice of the target material itself is important for the production of nuclei far from stability. One trivial parameter is the melting point. Tin and Copper targets were eliminated as choices because of local melting from the 10-30 w of power that the beam deposited as it stopped in the target. This power can be quickly obtained as the product of the beam current (as measured by a charge integrator on a faraday cup or target) and the effective beam voltage (the DC voltage that would be necessary to accelerate the particles to their present energy). The equivalent voltage of a beam is just E/A * m/q, 35 * 22/7 ≈ 110 MV for the beam mentioned above.

From a reaction standpoint the mass of the nucleus and 'neutron-richness' also seem to play a role. A heavy nucleus such as Ni or Ta seems to be more effective in removing many nucleons from the beam than a light nucleus such as Be. This effect seems to be strong enough to offset the larger number of Be nuclei that can be put into a target of a given thickness with respect to the energy loss of the beam. (i.e. Be has more nuclei for a given number of electrons and therefore for a given energy loss). A large N/Z ratio of the target seems also to be important for the production of the most neutron-rich fragments. There is no clear rule. Using a beam of ^{22}Ne at E/A = 60 MeV, DUFOUR87 report that ^{17}B was produced by a tantalum (Z=73, N=108) target at a much higher rate than with a Beryllium (Z=4, N=5) target. However, ^{18}C and ^{19}C were produced at a higher rate with the Beryllium target. It is important to note that while both ^{17}B and ^{18}C can be produced by simply removing nucleons from the ^{22}Ne beam, ^{19}C can be produced only by accepting a neutron from the target. Since projectile fragmentation targets are extremely thick compared to traditional targets, it is possible that a fragment may undergo a second nuclear reaction in the target before leaving. Thus the ^{22}Ne may loose three nucleons in the first reaction and become ^{19}N, then pass a second nucleus and exchange a pion somewhere else in the target, becoming ^{19}C.

It is not clear what conclusions could be drawn from the results just mentioned, except that the choice of target is difficult, and should be made during the experiment!

III.3 Half Life Determinations:

Half-lives of many light neutron-rich isotopes have been measured with the RPMS at NSCL (SAMUEL88, CURTIN86). We have used the same

technique as WESTFALL80 to measure the half-life of projectile fragments. Once an isotope of interest is identified in a silicon detector telescope, the beam is shut off and the gain of the silicon detector preamplifiers is raised. That projectile fragments have such a long range - much longer that the recoils from target fragmentation or fusion - is an important element of this technique. The detectors can be quite thick, sometimes many mm of silicon. This is important since the beta particle is approximately minimum-ionizing, and loses only 0.5 MeV per mm in silicon.

Now that an atom has been identified and is known to lie within a given silicon detector, and the time of the arrival is recorded, it can be directly linked to any 'decay' event corresponding to a beta decay within that detector.

Four points are now discussed that must be considered both when designing a particular half-life experiment, and when analyzing the data afterward. First is the choice of detector thicknesses. Next are sources of background events. Third is the functional form of decay curves fitted to the data under different conditions, and fourth is techniques for fitting these curves to the data.

VII.3.1 Choice of Detector Thicknesses:

There are a few considerations involved in the choice of detector thickness. The sensitivity of a detector to minimum-ionizing beta activity is proportional to the distance that a beta travels in the silicon. Therefore thicker detectors give bigger signals. However, thicker detectors will tend to stop other isotopes which might contaminate the decay curve. Thin detectors, on the other hand, have the

advantage that they allow separation of activity beyond m/q, on the basis of range (see below).

There is no combination of electric and magnetic fields that will separate two isotopes of the same m/q. However, interaction with matter will allow such separation. For example, if the RPMS is tuned to m/q = 3, the isotopes ^{3}H, ^{6}He, ^{9}Li, ^{12}Be, ^{15}B and ^{18}C will all pass through with approximately the same distribution in velocity. Using Equation 7.7, it can be shown that the range of fragments vary roughly as $(A/Z^2)\cdot(E/A)^{1.7}$, or $(A/Z^2)\cdot v^{3.4}$. Thus for fixed m/q and a velocity window of 10%, two species with a difference in Z greater than about 30% will not overlap in range. In other words, one isotope will completely stop in one volume of silicon, while the other will stop completely in a distinctly separate volume. This method has separated ^{13}B and ^{18}N which are only 1% different in m/q and otherwise difficult to completely separate with the RPMS. It would also help reduce the rate of one of the pair of ^{12}Be and ^{15}B with respect to the other. These have nearly identical half-lives and identical m/q.

The measurement of the half-life of ^{19}N serves as a good example. The large flux of ^{8}Li, ^{11}Be and ^{14}B (m/q = 2.67, 2.75, 2.8 respectively) which "leaked through" the RPMS when measuring the half-life of ^{19}N (m/q = 2.71) mostly passed through the detector which was used for decay studies because of the difference between the ranges of these particles and that of ^{19}N (SAMUEL88a). A simulation of the vertical position and range (longitudinal position) distribution of these isotopes is shown in Figure 7.5. This separation was very helpful. However, the decrease in the thickness meant a smaller signal produced by the beta in the silicon. A trigger efficiency of 50% was

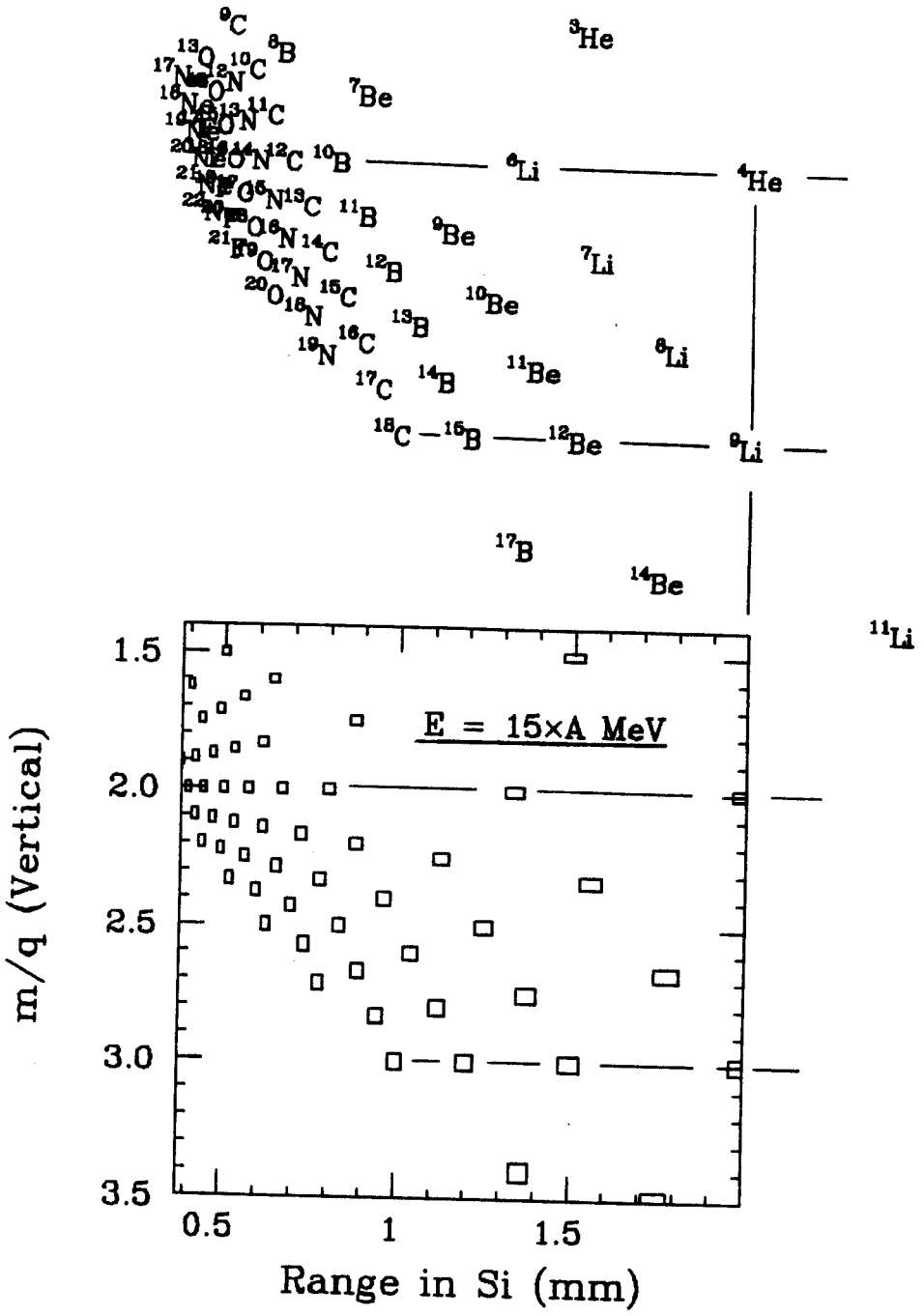

Figure 7.5 Illustration of the spatial separation of fragments at the focal plane of the RPMS. The vertical axis corresponds to vertical position at the location of the detectors, which is inversely proportional to the mass to charge ratio m/q. The horizontal axis corresponds to implantation depth in the silicon detector(s)

obtained in this experiment for detection of the beta decay.

VII.3.2 Background Problems:

There have been at least four sources of signals that resemble beta-decays of the isotope of interest, but are in fact of other origin and must be identified and in most cases eliminated before good half-lives can be extracted. Three of these; daughter and other residual activity, cosmic rays, and thermal neutron-induces activity result in actual ionizing events in the silicon. The fourth, electronic noise, originates in the amplification and transmission of signals from the experimental vault to the data-U.

To illustrate the sensitivity to background, consider a hypothetical situation with a fixed number of atoms and a fixed rate of background (e.g. 1000 atoms initially and 1 count per second of background. It is always easier to measure the half-life accurately when it is short. If the half-life is 1000 seconds, there will be over 3000 background counts in the time that it takes for 900 of the atoms to decay. However, if the half-life is short, say 1 second, then there will only be 3 or 4 counts due to background before 900 decays have occurred.

If the atoms are not produced at once, but spread out in time, then the situation gets worse. If the rate of production is much less than one atom per half-life, then the sensitivity to background is roughly one thousand times worse! So, if the half-life is one second, then 3 or 4 counts of background will contaminate the decay of each atom, and if the half-life is 1000 seconds, then the hopeless situation

of over 3000 background counts per real decay eliminates the possibility of measuring the half-life!

VII.3.2.1 Daughter Activity:

When a nucleus is said to be far from stability, this almost always means that two or more sequential beta decays are necessary for it to reach stability. Since the decay energy and therefore the decay rate tends to increase with distance from stability, the half-lives of the daughters are almost always much longer than the initial isotope produced. For example, while the half-lives of ^{17}B and ^{19}N are 5 and 250 mS respectively, the first daughter half-lives (^{17}C and ^{19}O) are 30 and 100 times longer. For the very short-lived activities, a single atom will usually decay before the next is produced, and therefore the beam is shut off after each ion is detected and does not resume until many (usually five or six) half-lives of the atom have passed and it has had sufficient chance to decay. However, the period that the beam is shut off is often short compared to the half-life of the daughter activity produced by the first decay, and therefore a build-up of daughter activity in the detector may occur. One solution is to reduce the beam intensity and therefore production rate to keep the decay spectrum clean, however this would lead to a dramatic drop in the number of decays observed and consequently a drop in the statistical integrity of the data. This problem is discussed in more detail in Section VII.2.3.3, and experimental solutions are described in Section VIII.5 and VIII.6.

VII.3.2.2 Cosmic Rays:

Cosmic ray muons are a second source of ionizing background activity in the silicon detectors. These have a flux of about one or two

counts per second per cm^3. See AGUILAR-BENITEZ88 for a more complete breakdown of cosmic ray rates, energies and angular distributions. The muons are the decay products of high-energy pions, which are themselves produced by the collision of very high energy cosmic ray protons with the nuclei of atmospheric atoms many kilometers above the surface of the earth. Since the muons stop in many meters of earth, they are not isotropic, but instead are from only the upper hemisphere, predominantly within 45° of the zenith. Since the muons are moving relativistically, and are approximately minimum ionizing, the distribution of energy losses in a detector is proportional to the distribution of path-lengths. The muons will generate signals not very different from a source of minimum ionizing beta particles from implanted activity, and therefore have a very strong probability of generating background at a rate of the order of one count per second. Because of their high average energy, a muon will rarely come to rest within any given detector system of reasonable size. It would instead pass right through, losing about 1.5 MeV for every g/cm^2 areal density. If a 'box' made of some material capable of detecting muons is placed around the silicon, the muon signal in the silicon can be rejected based on a coincidence with this 'anti' detector.

VII.3.2.3 Thermal Neutrons:

While cosmic rays have no structure in time, a third source of ionizing background in silicon detectors at the focal plane of the RPMS has posed a significant problem to the determination of only the shortest of half-lives. Figure 2 of SAMUEL88 shows an accumulated time spectrum of beta-like events in the first 50 ms following the arrival of the (relatively) long lived isotope ^6He ($t_{1/2}$=800 ms). After the

ion arrives the cyclotron beam is shut off within 40 μs. In addition to the flat background plus slow decay of ^{6}He there is a very rapidly decaying component within the first 10 ms after the beam is shut off. This component can be fit with an exponential function with a 'half-life' of 4 ± 1 ms. CURTIN86 has attributed the time structure of this component to the diffusion and absorbtion of thermal neutrons within the experimental vault. Since the target (the source of the neutrons) is about 15m from the detectors and the velocity of a neutron with a kinetic energy of 0.025 eV (roughly kT at STP) is about 2 m/ms, this explanation is plausible[8]. A similar problem has been encountered at GANIL, where the drift spaces are larger and the 'half-life' of the background is 6 ms. They have adopted the same explanation.

The mechanism by which the neutrons induce ionizing signals in the silicon is not clear. Thermal neutron capture is possible. The ^{6}Li in the lithium-drifted silicon detectors has a cross-section for capture of thermal neutrons resulting in the emission of an alpha particle of about 1000 barns. However these should show up as a peak in the energy spectrum of the silicon detector of about 4.75 MeV, which has not been observed so far. The experiment of SAMUEL88a made use of only surface barrier detectors without lithium doping, and still the 4 ms 'activity' was present. More likely, the neutron is captured by a silicon nucleus (cross section of the order of 0.1 barn) or other material nearby, and a high-energy (5 to 8 MeV) gamma ray is emitted. These photons can

8. The only other reasonable explanations are fast-neutron induced 4ms beta or isomeric gamma decay (E_γ > 0.5 MeV) in the vault. It is not likely that either of these processes could be so prolific.

produce a small shower of lower energy e^+e^- pairs and $e^-\gamma$ Compton pairs, and can then easily give a broad low-energy distribution.

The short time-structure and high multiplicity (one count for every eight beam-off periods[9]) interferes with half-life determinations less than about 20 ms, but does not significantly affect the longer-lived activities if the first 20 ms of the data is ignored. See SAMUEL88.

VII.3.2.4 Electrical Noise:

A fourth source of background counts is not related to ionization in the silicon, but instead is electronic in origin. The elimination of this problem is not simple, and has required extensive tests and modification of the original techniques of Curtin and Westfall. Most of these modifications are in the electronic set-up of the experiment, and will be described in Section VIII.3. The only points that can be made involving the physical environment of the detectors is their shielding to electromagnetic radiation, both 'RF' (60 Hz through 1 GHz) and visible light, and grounding.

The silicon detectors are photo-sensitive. Visible photons from fluorescent room lights produce electron-hole pairs in the detector - a reverse biased diode) and induce a complex 120Hz modulation. This results in huge signals from the pre-amplifier. The solution here is

9. This represents the rate of "4 ms" events in a silicon surface barrier detector of 0.6 mm thickness and an area of 300 mm^2, with a constant fraction discriminator threshold of roughly 0.5 MeV (as determined by a ^{207}Bi electron conversion source). The detector was surrounded by roughly 300g of Aluminum as a detector holder. The average beam intensity was about 200μA of E/A = 35 MeV $^{22}Ne^{+7}$, impinging on a tantalum target thick enough to stop the beam - roughly 0.015 inches.

obvious - light shielding is necessary. It does not however, have to be as complete as one would need for an active device with multiplication such as a photo-multiplier tube.

The silicon detectors are also effectively large-area bare capacitors hooked to an extremely sensitive charge amplifier. Any stray electric or magnetic fields will induce the motion of charges and therefore big signals from the preamp. Good results have been obtained with a Faraday cage in the form of an aluminum detector holder and thin aluminized mylar windows. Attention should be paid to skin depth. While the preamplifier system is not so sensitive to the low frequency components of induced currents, they are typically intense at NSCL, and not necessarily shielded by the thin metalized window. The use of a thick metal collimator and the placement of detectors far from the hole inside the 'cage' will help shield at all frequencies to which the system is sensitive (except light), since the hole will be much smaller than a quarter wave-length.

The gas proportional counters for position detection are also quite sensitive to induced fields. A sheet of aluminum foil or other thin conductive material between the gas detector and beam-line ground such as the m/q slits dramatically reduces induced 60Hz noise. One should take care that particles of interest pass through unimpeded.

VII.3.3 Decay Curves:

VII.3.3.1 One Atom at a Time Operation:

If one atom, or an instantaneously produced group of atoms were to decay to a stable daughter with a decay rate λ, then the rate of change of the number of atoms, and the total number atoms at time t respectively are

$$\frac{dN}{dt} = -\lambda N, \qquad N = N_0 e^{-\lambda t}; \quad t \geq 0. \tag{7.16}$$

The instantaneous rate of decay is then

$$r(t) = -\frac{dN}{dt} = \lambda N = \lambda N_0 e^{-\lambda t}. \tag{7.17}$$

If this decay is recorded as a function of time one would measure

$$R(t) = \varepsilon r(t), \tag{7.18}$$

where ε is the efficiency for detecting decays. In this notation, R represents the experimentally observed count-rate, while r represents the actual decay rate.

Now, if m atoms are produced at known but different times t_i,

$$r(t) = \lambda \sum_{i=1}^{m} e^{-\lambda(t-t_i)} \theta(t-t_i), \tag{7.19}$$

where θ is the step function to insure that only those atoms which have already arrived before time t are counted. In the limit of a very large number of atoms, the rate of arrival can be written as a continuous function A(t) and the decay rate is just the convolution

$$r(t) = \lambda \int_{-\infty}^{t} dt' \, e^{-\lambda(t-t')} A(t'). \tag{7.20}$$

For very exotic species, the half-lives tend to be very short (large λ) and the times between arrivals tend to be long (many times $1/\lambda$). The cyclotron is then shut off after each arrival, and the decay of the single atom is observed. The arrival time of all atoms are recorded, so that a complete history can be reconstructed. For such a sparse time-structure, only the most recent previous ion (nearest neighbor) correction is usually necessary. The decay rate after the arrival of atom N is then

$$r(t, t \geq t_N) = \lambda e^{-\lambda(t-t_N)} + \lambda e^{-\lambda(t-(t_N - t_{Non} - t_{off}))}, \tag{7.21}$$

where t_{Non} represents how much beam-on time was needed produce the N^{th} atom after the end of the $N-1^{\underline{th}}$ cycle, and t_{off} is the length of the time that the beam is off after the arrival of any atom. Simplified, this gives

$$r(t,t\geq t_N) = \lambda e^{-\lambda(t-t_N)} \left(1 + e^{-\lambda(t_{Non}+t_{off})}\right). \qquad [7.22]$$

Now the data usually consists of hundreds or thousands of such iterations, and an average decay curve can be built up by summing the decay curves following the arrival of each atom, making all the previous atoms the history of the detector at that point. If, during the beam-on periods, atoms are produced at an instantaneous rate λ_p, then the distribution of t_{on}'s is just given by the interval distribution

$$P(t_{on}) = \lambda_p e^{-\lambda_p t_{on}}, \qquad [7.23]$$

when the production rate is stable in time[10].

If Equation 7.23 applies, then the measured decay rate with its nearest-neighbor correction can be averaged over all possible values of t_{on},

$$r(t) = \lambda e^{-\lambda t} \left(1 + \int_0^\infty dt_{on}\, e^{-\lambda(t_{on}+t_{off})}\, \lambda_p e^{-\lambda_p t_{on}}\right), \qquad [7.24]$$

which becomes,

$$r(t) = \lambda e^{-\lambda t} \left(1 + \frac{\lambda_p}{\lambda+\lambda_p} e^{-\lambda t_{off}}\right). \qquad [7.25]$$

So, for example if the off period is three half-lives, and the atoms are produced on the average one every half-life (when the beam is

10. The production rate could vary due to fluctuations in beam current, drift in beam-line and RPMS elements, and changes in target thickness due to sputtering, evaporation and softening. It is therefore better to determine $P(t_{on})$ directly from the data if possible.

on), then when an atom arrives, there is a 5% chance that the atom from the previous cycle is still there.

If only the decay rate of a single isotope were to be determined, (this is equivalent to a half-live measurement of a pure source with no daughter activity) then this carry-over would not have any significant effect. However, there is usually more than one isotope passing through the m/q defining slits and reaching the detectors. It is then important to understand how much of once species is contaminating the decay spectrum associated with the another. For instance, any determination of the half-lives of ^{12}Be, ^{15}B and ^{18}C (all m/q = 3 with $t_{1/2}$ ~ 22ms, 10ms, and 70ms respectively, from CURTIN86 and MUELER88 will require the understanding of how each species contaminates the decay curves of the others.

The experimental decay spectra are usually generated for each isotope. This is done by summing together the distributions of all of the decay events directly associated with (following the arrival of) each type of atom. If the atom of type i has just arrived in the detector, then

$$R(t) = \varepsilon_i r_i(t) + \sum_{j=1}^{m} \left(\frac{\lambda_{pj}}{\lambda_{pt}}\right) \varepsilon_j r_j(t) e^{-\lambda_j t_{off}} \lambda_{pt} \times$$

$$\int_0^{\infty} dt'_{on}\, e^{-\lambda_j t'_{on}}\, e^{-\lambda_{pt} t'_{on}}$$

$$= \varepsilon_i r_i(t) + \sum_{j=1}^{m} \left(\frac{\varepsilon_j \lambda_{pj}}{\lambda_{pt}+\lambda_j}\right) \varepsilon_j r_j(t) e^{-\lambda_j t_{off}}, \qquad [7.26]$$

where m is the total number of types of atoms, ε_j is the efficiency, λ_j is the decay rate, λ_{pj} is the partial rate of production of the $j^{\underline{th}}$

type of atom, λ_{pt} is the total rate of production of all atoms, such that

$$\lambda_{pt} = \sum_{i=1}^{m} \lambda_{pi}, \qquad [7.27]$$

and

$$r_j(t) = \lambda_j e^{-\lambda_j t}. \qquad [7.28]$$

The efficiencies ε could be different for different species for two reasons, their range distributions in the silicon can differ (Section VII.3.1), as can the energy loss and multiple scattering of the beta. See Section VII.4.4.

If the beam-off time t_{off} is made to be different for each isotope, (see Section VIII.5), then the subscript j can be added to t_{off}.

VII.3.3.2 Fixed Cycle Operation:

When the species is produced at a rate much higher than the decay rate, it is not efficient any more to turn off the beam each time an atom arrives. In this cases, it is better to have switch the beam on and off continuously at a fixed rate.

This was the case for a recent experiment to study the beta-delayed alpha emission from ^{16}N (see Section V), where the half life is near 1 second and the production rate near 20 atoms per second. The experimental cycle was divided into four periods. The first was the beam-on period, next a short wait, then a beam-off period during which the decay of ^{16}N was studied, then a second wait period. These will be referred to as t_{on}, w_1, t_{off}, and w_2 , and were set to 1.0, 0.05, 1.0 and 0.10 seconds respectively. The total cycle period t_c is just the sum of these four periods.

In this experiment, the absolute time of arrival of each ^{18}N atom was recorded, as well as the time of each decay (see Section VIII.1). For the branching ratio to be determined, it was first necessary to count the number of alpha decays detected, and the number of ^{18}N atoms collected during a given run. However, the ratio of these two numbers is not yet the branching ratio, since some decays occur when the beam is on, and therefore go undetected. This ratio must be divided by the efficiency for detecting an event to obtain a branching ratio. The efficiency can contain many terms related to experimental conditions, but the term representing the fraction of the decays that occur during a beam-off period dominated, and is derived below.

If ^{18}N nuclei were produced in only a single beam-on period, then one can easily show that Equation 7.20 gives

$$r_s(t) = \lambda e^{-\lambda t} e^{-\lambda w_1} \int_0^{t_{on}} dt' \, A(t') e^{-\lambda(t_{on}-t')}, \qquad [7.29]$$

where r_s is the decay rate of the group of atoms produces in a single beam-on pulse. If instead ^{18}N is produced in an infinite number of previous beam-on periods, then an extension of Equation 3.29 gives

$$r_\infty(t) = r_s(t) \sum_{a=0}^{\infty} e^{-a\lambda t_c},$$

$$= \frac{r_s(t)}{1-e^{-\lambda t_c}} . \qquad [7.30]$$

If A(t) is nearly constant in time within the beam-on period, then the integral in Equation 7.29 can be evaluated. Then, if r_∞ is itself integrated over the beam-off period, the efficiency for detecting the alpha particles becomes

$$E_{cyc} = \int_0^{t_{off}} dt'\, r_\infty(t') = \frac{e^{-\lambda w_1}\,(1-e^{-\lambda t_{off}})(1-e^{-\lambda t_{on}})}{(1-e^{-\lambda t_c})}\,. \qquad [7.31]$$

VII.3.3.3 Daughter Activity:

In Equation 7.26 a correction was shown to be necessary if an experiment intended to determine the half-life of an isotope can not absolutely differentiate decay signals from the isotope of interest from those of other isotopes implanted. As pointed out in section VII.3.2.1, the decay of a nucleus which is far from stability is usually followed by the decay of one or more daughter nuclei. So it is now also important to consider the effects of daughter activity, since this will create an extension of the distribution of counts beyond what one would expect for a simple decay, and will usually make the measured half-life too long if not properly taken into account. See below.

If a source of parent nuclei is created at time t=0, then the rate of decay of the parent is

$$r_1(t) = \lambda_1\, e^{-\lambda_1 t}\,. \qquad [7.32]$$

The rate of decay of the daughter nucleus (the "grow in" curve) is just the convolution

$$r_2(t) = \lambda_2 \int_0^t dt'\; \lambda_1\, e^{-\lambda_1 t'}\, e^{-\lambda_2 (t-t')}\,,$$

$$= \frac{\lambda_1\,\lambda_2}{\lambda_1 - \lambda_2}\,\left(e^{-\lambda_2 t} - e^{-\lambda_1 t} \right). \qquad [7.33]$$

If the daughter has in turn a daughter of its own, then a second convolution of r_2 with the tertiary decay rate gives r_3,

$$r_3(t) = \lambda_3 \frac{\lambda_1\,\lambda_2}{\lambda_1 - \lambda_2} \int_0^t dt' \left(e^{-\lambda_2 t'} - e^{-\lambda_1 t'}\right) e^{-\lambda_3 (t-t')}\,,$$

$$= \frac{\lambda_1\lambda_2\lambda_3}{(\lambda_1-\lambda_2)} \left[\frac{1}{\lambda_2-\lambda_3}\left(e^{-\lambda_3 t} - e^{-\lambda_2 t}\right) - \frac{1}{\lambda_1-\lambda_3}\left(e^{-\lambda_3 t} - e^{-\lambda_1 t}\right) \right]. \qquad [7.34]$$

The decay rate of the parent r_1 is a maximum at t=0, and has a slope equal to $-\lambda_1$. Both r_2 and r_3 are 0 at t=0, but while r_2 has a positive slope at t=0, the slope of r_3 is zero at t=0.

Equation [7.34] can be easily generalized to the situation where there is more than one daughter activity following the decay of a parent, and each of these daughter nuclei will themselves be followed by more than one tertiary decay. The decay rates, per atom, are

$$r_1(t) = \lambda_1 e^{-\lambda_1 t},$$

$$r_{2i}(t) = \frac{\lambda_1\lambda_{2i}}{\lambda_1-\lambda_{2i}}\left(e^{-\lambda_{2i}t} - e^{-\lambda_1 t} \right),$$

$$r_{3ij}(t) = \frac{\lambda_1\lambda_{2i}\lambda_{3ij}}{\lambda_1 - \lambda_{2i}}\left[\frac{1}{\lambda_{2i}-\lambda_{3ij}}\left(e^{-\lambda_{3ij}t} - e^{-\lambda_{2i}t}\right) - \frac{1}{\lambda_1-\lambda_{3ij}}\left(e^{-\lambda_{3ij}t} - e^{-\lambda_1 t}\right) \right]. \qquad [7.35]$$

The rate of events recorded in the experiment following the production of a single parent nucleus R(t), is then

$$R(t) = \varepsilon_1 r_1(t) + \sum_{i=1}^{m_1} \omega_{2i} \left(\varepsilon_{2i} r_{2i}(t) + \sum_{j=1}^{m_{2i}} \omega_{3ij}\varepsilon_{3ij} r_{3ij}(t)\right), \qquad [7.38]$$

where ω_{2i} is the fraction of beta decays of the parent which result in nucleus i as a daughter, ω_{3ij} is the fraction of beta decays of nucleus i which result in nucleus j as a tertiary product, ε_1, ε_{2i}, and ε_{3ij} are the appropriate efficiencies for detecting a decay, and m_1 and m_{2i} are the number of daughters and of tertiary products considered for each of those daughters, respectively.

The decay of the isotopes ^{12}Be and ^{17}B serve as good examples to explore experimental problems associated with daughter activity. In the case of ^{12}Be with a half-life of roughly 0.022 seconds, the

daughter ^{12}B has a nearly identical half-life of 0.020 seconds. Since both have a decay energy of about 12 MeV, their decays should look similar in the silicon detector and therefore be difficult to discriminate. A simple fit to a decay curve containing events from both ^{12}Be and its daughter activity will always give a half-life longer than the correct value for ^{12}Be. CURTIN86 approached this problem by requiring two pulses to occur within a preset time interval, and then assigning the first recorded pulse to the decay of ^{12}Be and the second to that of ^{12}B. While this method could slightly bias the extracted value for the half-life, it was successful in separating the two activities. A more sophisticated method with which to treat the order of the pulses is discussed in section VII.3.4.3.

The decay of ^{17}B is even more complex. The beta decay of ^{17}B will not always be followed by the decay of ^{17}C. Since the decay energy of ^{17}B is so great, it can populate levels in ^{17}C which emit a neutron, leaving ^{16}C. There is then ^{16}C activity associated with ^{17}B decay. ^{17}B can also feed very high-lying levels in ^{17}C which are unbound to two or more neutron emission. The decay of these levels can then produce ^{16}C, ^{15}C, ^{14}C and ^{13}C by beta-delayed one, two, three or four neutron emission. Most of these daughter nuclei are radioactive, and some are themselves beta-delayed neutron emitters. Thus the decays of ^{17}C, ^{17}N, ^{16}C, ^{16}N, ^{15}C, and even ^{14}C can sometimes follow ^{17}B decay. Values for half-lives and delayed neutron probabilities relevant to the decay of ^{17}B have been taken from various experimental results and shell model calculations. Since they were compiled for illustrative purposes only, they are not given here.

The half-life of ^{17}B was first measured by SAMUEL88. In this experiment, the rate of production of ^{17}B was low enough (less than 100 atoms per hour) so that there was little interference from the daughter decays in the decay curve of ^{17}B. At higher production rates however, the buildup of these activities would have caused a significant problem for the analysis.

In Figure 7.6, the total beta-decay rate probability from a single atom of ^{17}B produced at time t=0 is shown. The individual components of ^{17}B, secondary and tertiary products are illustrated, as well as the total rate of all isotopes together. Figure 7.7 shows the same information, but has been extended to a much longer time scale to better show the decay of the longer lived products.

In Figure 7.8, the simulated decay spectrum of ^{17}B and its products has been generated for a production rate of 100 atoms per second for a period sufficiently long (more than one minute) so that the decay of the products is fully equilibrated with the production rate of ^{17}B (one approximately every two half-lives.) The primary (^{17}B only) and total decay rates for this case is compared to those of a single atom of ^{17}B as calculated for Figures 7.6 and 7.7. While the total decay rate rapidly departs from that of ^{17}B alone in the high production rate case, the total decay rate associated with the single atom closely follows that of ^{17}B alone for many half-lives.

From Figure 7.8, one can conclude that if this build-up is allowed to occur, it would be nearly impossible to obtain an accurate half-life without detailed information on the delayed-neutron emission probabilities and half-lives of the many isotopes involved, and their detection efficiencies. Thus the full production rate is useless in

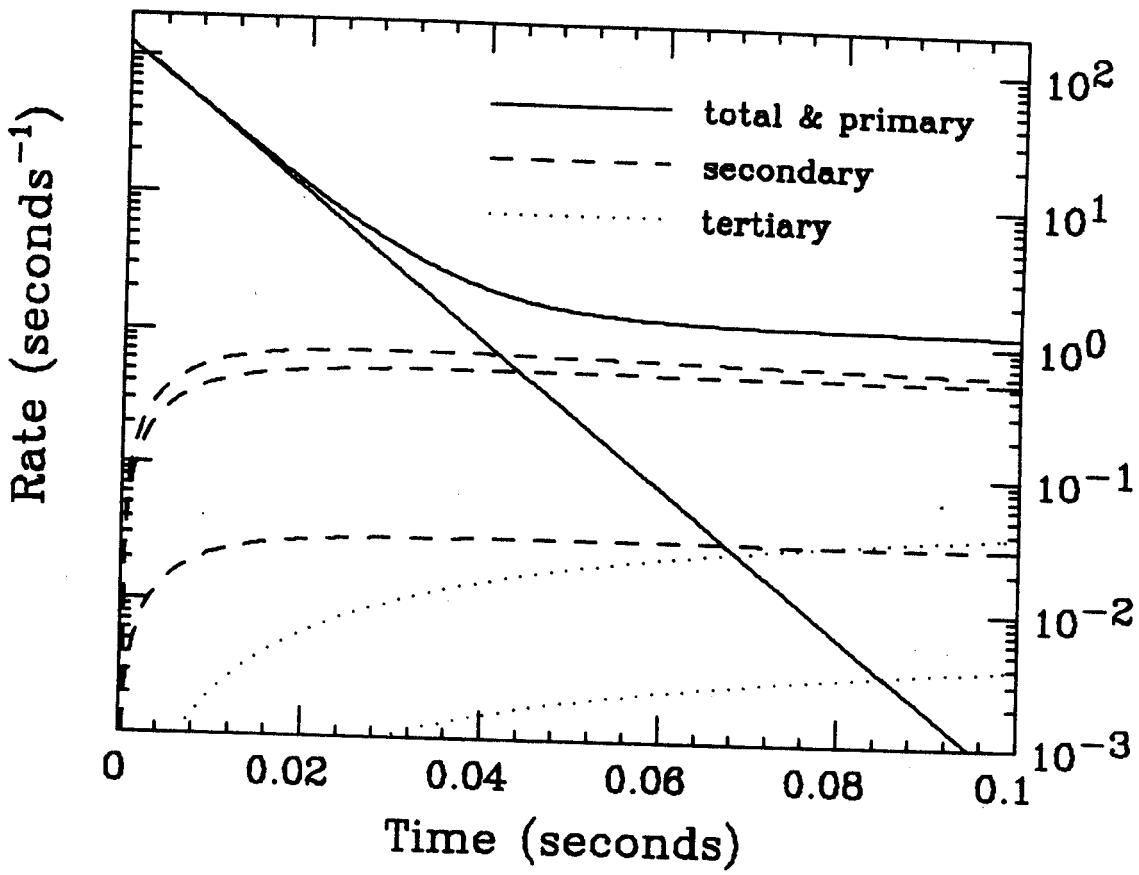

Figure 7.6 Decay rates of the various components from an initially pure source of ^{17}B, including ^{17}B, ^{17}C, ^{17}N, ^{16}C, ^{16}N and ^{15}C activity. See text for details.

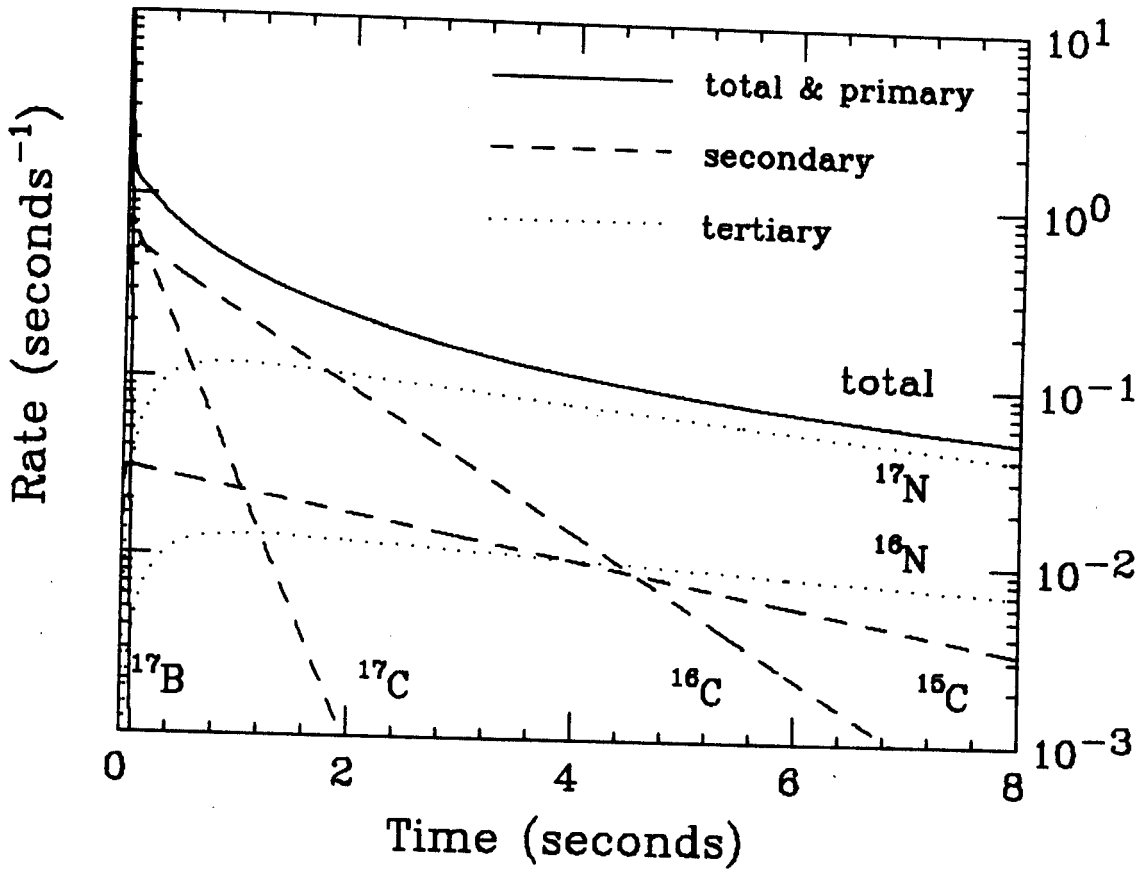

Figure 7.7 Same as Figure 7.6, but shown on a compressed time scale.

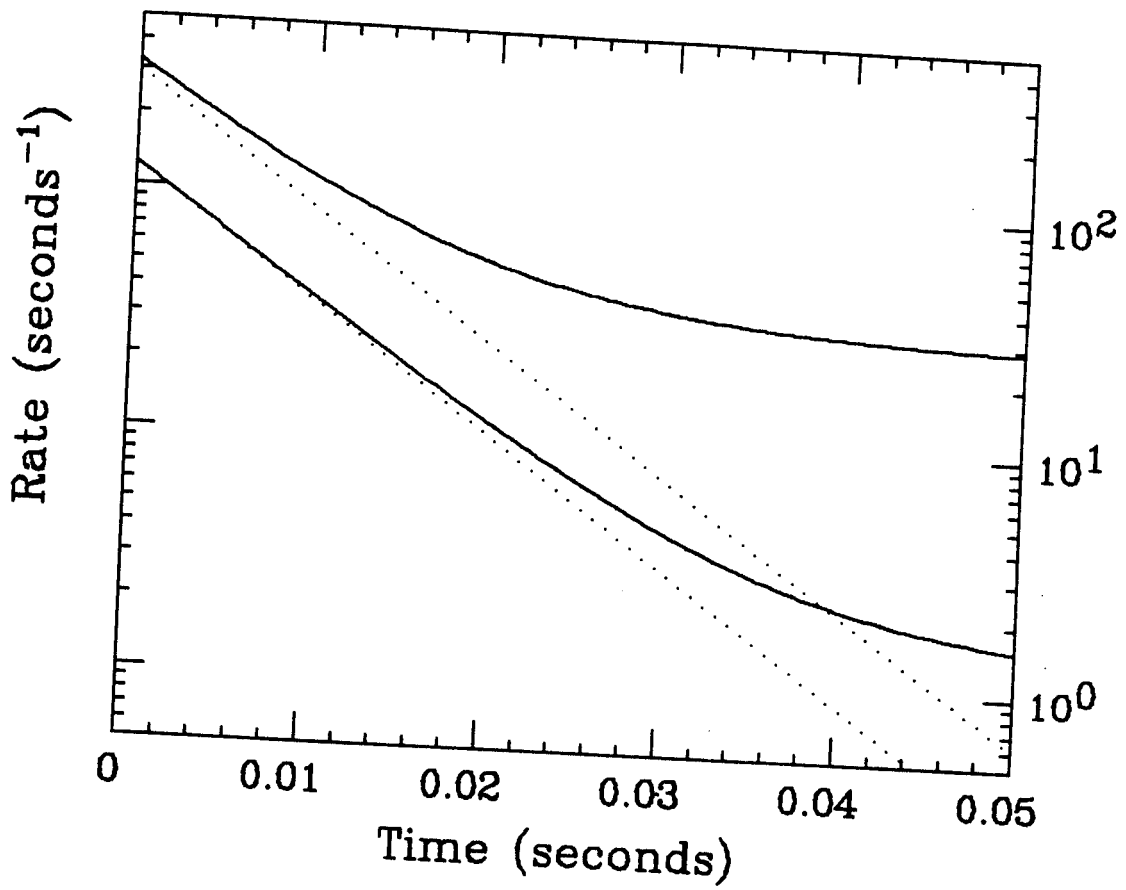

Figure 7.8 Primary ^{17}B decay rate and total decay rate for two sources of ^{17}B. The lower curves represent an initially pure source of ^{17}B. The upper curves represents an initially equilibrated source with a ^{17}B production rate of 100 per second. The total decay rate of the initially equilibrated source deviates strongly from a the decay rate of ^{17}B itself, and illustrates the difficulty in extraction of a correct half-life when the production rate is too large!

this situation, and the beam intensity and thus the total number of decays observed would have to be greatly reduced to insure the accuracy of the measurement. While it is conceivable that one might try to extract delayed-neutron probabilities by building up a 'source' of daughter activity for a long period (long with respect to the half-life of ^{17}B itself, but not to that of the daughter activity) and careful measurement of the exact shape of the slow component of the decay spectrum, it would be difficult in practice for many reasons, not the least of which is the large number of free parameters involved.

When one requires the activity to stop within the actual device used to detect the beta particle, then little can be done to avoid the daughter build-up except for limiting the count rate. For certain cases, if the maximum energy of the beta particle from the daughter activity is low enough then the detection system may be made immune to these decays by simply raising the electronic threshold above this energy. CURTIN86 successfully used this technique to remove ^{6}He activity from the decay spectrum when measuring half-lives near m/q = 3.0. The decay energy of ^{6}He is only 3.5 MeV, and most beta particles are less than 2 MeV. All other activities near m/q=3 have decay energies above 10 MeV. The thickness of the detector used (5mm) insured that most high-energy betas could loose more than 2 MeV in the silicon, and thus would produce signals above the threshold.

However, if one allows the activity to come to rest in something other that the detector itself, and this 'catcher' can be periodically removed and a new catcher put in place of it, then one can avoid build-up of unwanted activity. A device has been constructed to accomplish this. A wheel of thin plastic with a circumference of nearly a meter

is mounted on a fast DC torque motor, and can be moved under computer control. The wheel is placed such that one part of its perimeter is sandwitched between two silicon detectors. Once an atoms passes through the first detector and comes to rest within the wheel, it is rotated to a beta detector. As this occurs, a clean section of the wheel is moved into place to catch the next atom. This device is discussed in detail in section VIII.6.

VII.3.4 Fitting Procedures:

In order to understand the decay data, one fits an appropriate theoretical time distribution to the data. The theoretical distribution will most likely have at least one free parameter that can be adjusted until the fit is considered optimum. For example, if one has a source of atoms for which a half life is required, a distribution something like one of the expressions for R(t) above is used, or perhaps something as simple as $N_o \exp(-\lambda t) + b$, with N_o, λ, and b (a constant background term), as adjustable parameters.

It is not always such a simple task to compare two sets of parameters, and determine which is the 'better' fit in order to converge on the 'best' fit. We will use the definition that the better fit is the one which has more probability of having generated the data. Thus the best fit is the set of parameters which has the most probability of having generated the data, of all available choices in parameter space which are physically meaningful. If the experiment were to be carried out many many times, the data would become smooth (an exact exponential plus constant in this example) and the best fit determined to arbitrarily good accuracy if the fitting function represents the actual physical phenomena responsible for the data. However, statistical

variation will cause each data-set to differ from the smooth function. The best fit is the one which requires the least amount of statistical variation to account for the difference between the fit and the data. This can now be defined mathematically.

In order to calculate which of two functions is more likely to have generated the data, the set p_i is defined as the distribution of probability of the measured values y_i about a particular trial "best" value $y(x_i)$,

$$p_i = f(y_i, y(x_i)), \qquad [7.37]$$

where x_i is the $i^{\underline{th}}$ value of the independent variable of a measurement (the time associated with the $i^{\underline{th}}$ channel of a decay histogram for instance), y_i is the measured value at that channel (number of counts for instance), and $y(x_i)$ is the fitted function evaluated at that point.

VII.3.4.1 Least Squares:

Typically, for large number of counts where the normal distribution can be used,

$$f(y_i, y(x_i)) = \frac{1}{\sqrt{2\pi\sigma_i^2}} e^{-\frac{(y_i - y(x_i))^2}{2\sigma_i^2}}, \qquad [7.38]$$

where σ_i is the RMS deviation of y_i about the "right" value $y(x_i)$, and is usually taken for large $y(x_i)$ as

$$\sigma_i = \sqrt{y(x_i)}. \qquad [7.39]$$

It is convenient to assume that the fit is usually fairly good when a fitting routine is near convergence, so most people make the approximation that

$$\sigma_i = \sqrt{y_i}, \qquad [7.40]$$

and thus draw their error bars on the data. However, it is important to remember that the error bars actually belong on the theoretical function, not the data! The data is simply data points - measurements. One must express how the data can be explained by statistical deviations about the fitted value.[11]

The best fit is determined by maximizing the overall probability P that a function y(x) could have generated this data when the proper form of the statistical deviations is included, and

$$P = \prod_{i=1}^{N} p_i \ . \qquad [7.41]$$

The function y will contain some variable parameters α_j, (e.g. N_o, λ, b) that will be adjusted to maximize P. Thus the set of j equations,

$$\frac{\partial}{\partial \alpha_j} P = 0 \ , \qquad [7.42]$$

must be solved simultaneously. Since the logarithm function is monotonic and P is presumably greater than zero, we may also maximize ln(P). If we use the normal distribution Equation 7.38 with the approximation of Equation 7.40, we can simply minimize (note sign change)

$$-\ln(P) = \sum_{i=1}^{N} \frac{(y_i - y(x_i))^2}{2\sigma_i^2} . \qquad [7.43]$$

If we let all the σ_i's have the same value, they can be omitted, and the requirement for the least-squares fit becomes just,

11. If you don't believe this, consider the result that for a normal probability distribution, the probabilities for measuring 1100 and 900 when the most likely value is 1000 are equal, while the probability of measuring 1000 when the most likely value is 1100 is greater than when the most likely value is 900.

$$\frac{\partial}{\partial \alpha_j} \sum_{i=1}^{N} (y_i - y(x_i))^2 = 0. \qquad [7.44]$$

Equation 7.43 and 7.44 represent the standard Least Squares technique. For many situations, the functional form of y(x) can be included explicitly, the derivatives taken, and the resulting simultaneous equations solved analytically. Alternatively, numerical techniques can be used.

VII.3.4.2 Maximum Likelihood:

Now, if the data is sparse, so that the normal distribution may not be used (i.e. few or zero counts per channel) Equation 7.44] is no longer valid and should not be used. If the fluctuations about the functional form of the fit are truly statistical, then one must use the Poisson distribution:

$$f(y_i, y(x_i)) = \frac{y(x_i)^{y_i} \; e^{-y(x_i)}}{(y_i)!} \; . \qquad [7.45]$$

If one takes the log of P, then differentiates with respect to the parameters α_j of y (Equations 7.37, 7.41 and 7.42), then dropping the terms with vanishing derivatives the more generally useful condition of Maximum Likelihood is obtained:

$$\frac{\partial}{\partial \alpha_j} \sum_{i=1}^{N} (y_i \ln(y(x_i)) - y(x_i)) = 0. \qquad [7.46]$$

VII.3.4.3 Use of All Available Information:

When one tries to extract information from data at the limits of statistical accuracy, it is important to use all of the information at hand. For instance if the decay of many isotopes are measured simultaneously one should not include independent backgrounds to the fitting functions for each of the isotopes, but instead couple the fits together such that the same background us used throughout. Negative

backgrounds and efficiencies greater than 1.0 should be excluded from the fitted parameter space since they are unphysical. However, while one might be tempted to impose the additional requirement that the area of the fitted function over the interval which overlaps with the data equal the total number of counts in the decay curve, this is usually rigorously imposed by the fitting technique itself. In most cases, Least-Squares and Maximum Likelihood automatically require this agreement and it should not be separately imposed.

There is one source of information that has been avoided here up to this point. It is the event-by-event ordering of the recorded decays following each ion. In our examples we have discarded a wealth of information by summing the event structure associated with each ion into a single histogram. The possibility for recovering additional information by maintaining the ordering of the decay events can be illustrated through the example of ^{12}Be decay.

Consider a simple model of an ideal experiment in which the half-life and delayed-neutron emission probability (P_n) of ^{12}Be is to be determined. The efficiency of the detection of the decay of both ^{12}Be and ^{12}B is in this example 100%, and there are no sources of background. The ^{12}Be ions are the only ions to reach the detector, and they are widely spaced in time so that the beam can be shut off for each ^{12}Be ion separately with no nearest-neighbor contamination. A histogram of the times of all decay events following the arrival of a ^{12}Be ion represents the sum of the decay rates of ^{12}Be and ^{12}B, and is obtained from Equations 7.36,

$$R(t) = r_1(t) + \omega_2 r_2(t), \qquad [7.47]$$

where r_1 and r_2 are the decay rates of ^{12}Be and ^{12}B respectively as described in Equations 7.32 and 7.33, and ω_2 is the delayed neutron probability P_n of ^{12}Be.

Under the conditions discussed above, a histogram of the times of the first decay event following the arrival of a ^{12}Be ion represents a pure decay curve of ^{12}Be only - the first term in Equation 7.47. However, a histogram of the times of the second decay event following the arrival of a ^{12}Be ion does not represent a pure exponential decay curve of ^{12}B, but instead represents a grow-in curve typical of a daughter (the second term in Equation 7.47). If instead the times between the first and second decay events are histogrammed, one is avoiding the convolution used to derive Equation 7.36, and the distribution should be that of a simple exponential decay curve of the daughter ^{12}B, whose normalization gives directly the value of P_n. This technique reduces the fitting requirement from one data set and three unknowns ($\lambda_{^{12}Be}$, $\lambda_{^{12}B}$, ω), to two data sets; the first with only one unknown ($\lambda_{^{12}Be}$) and the second with the two remaining unknown values ($\lambda_{^{12}B}$, ω). Since the reliability of a fit rapidly decreases with increasing number of fitted parameters, the reduction of the problem to two independent fits with fewer parameters should be a much more reliable way to obtain the half-life and delayed neutron probability of ^{12}Be.

This method is more difficult to apply in practice, since the ideal constraints in the above example are not usually applicable. There is normally a non-unity efficiency (50-90%), a non-zero and even time-dependant background, and sometimes even other longer-lived activity present in the detectors from previous cycles. The last problem

can sometimes be solved by using a partial data set. Regions (in time) of the data immediately following the arrival of a longer-lived species can simply be ignored for many half-lives of the ion. The structure of the background-plus-longer-lived activity component can be derived from the decay curves following the arrival of very long-lived or stable isotopes, or following a randomly generated trigger not associated with any heavy ion. See section VIII.2.5.

However, the worst problem here is the non-unity efficiency. This results in the miss-assignment of counts, and the addition of two more parameters - the efficiency for each of the two isotopes. Whereas in the simple example above the first count could always be associated with the decay of ^{12}Be and the second to that of ^{12}B, in the realistic situation both the first and second counts can be from any of the three sources; ^{12}Be decay, ^{12}B decay, or background. If the low count-rate restriction still applies, one may impose the conditions that if the first event is indeed the decay of ^{12}Be then the second count can be only ^{12}B decay or background, and if the first event is the decay of ^{12}B then the second count can only be background.

In this situation, the proper form for the theoretical distribution for the histogram of the first counts, second counts, third counts and so forth is difficult to calculate. In the limit of high efficiency (>90%) one might derive an expression which contains only first-order corrections to the that which is used for the ideal case discussed above. Thus if high efficiency can be obtained, the mother-daughter structure of the decay sequence may be preserved, increasing the reliability of the fitting procedure by reducing the number of fitted parameters, or at least the number of strongly-weighted

parameters in each fit. The high-efficiency requirement should be imposed on all future detector designs lacking other gating devices (such as gamma-ray or delayed proton or neutron tagging).

A further discussion of the use of all available information can be found in LYONS89a, b.

VII.3.4.4 Finite Channel Size:

It is important to remember that the decays are discrete in time, and not a continuous, smooth distribution. One does not actually measure the function R(t), but instead an array of integers representing the number of counts per channel; y_i. Counts-per-channel really represents an integral of the rate over the channel size, not the instantaneous rate at a fixed time, and there is only an approximate correspondence

$$R(i\Delta t) \approx R_i = \frac{1}{\Delta t}\int_{(i-1)\Delta t}^{i\Delta t} R(t')\,dt' \,. \qquad [7.48]$$

In the special case of $R(t) = N_o e^{-\lambda t}$ a pure exponential, the relationship between the two quantities in Equation 7.48 is simply $e^{\lambda\Delta t}$, and can be absorbed into N_o if the absolute normalization is not important. However, if any other function is used, even by the addition of only a constant term to the exponential, then the relationship becomes more complex. It is critical for the experimenter to determine for the particular nature of the data under analysis whether this effect is indeed significant or can safely be ignored. However this correction will most likely become important only when there are only a few channels per half-life or when the function is very non-exponential. More precisely, the derivative R'(t) should always be much smaller than $R(t)/\Delta t$.

VII.3.4.5 Uncertainties in the Fitted Parameters:

In addition to the extraction of the most likely values for the fitted parameters, any fitting procedure must also evaluate the certainty with which these values may be taken and used to interpret the underlying physics addressed by the experiment. This certainty is usually evaluated by calculating how far each of the fitted parameters may be altered before the agreement between the function and the data is degraded by a specified amount. Within the framework of the Least-Squares procedure, the agreement between the fitting function and the data points can be evaluated quantitatively by means of the normal probability distribution associated with each data point. This method is usually called the chi-squared method. With it, one can state exactly how good a fit is by stating how likely it would be for a second identical experiment (with data presumably differing from the data of the first experiment only in the manner described by the distribution f of Equation 7.37) to produce data less likely to have been generated by the fitted parameters.

In the Maximum Likelihood formalism however, there is no simple interpretation of the actual value of the log-Likelihood function (section VII.3.4.2), other than the fact that the maximum value is obtained when the fitted parameters are those most likely to have generated the data. While any other set of parameters give smaller values, the significance of the size of the decrease in terms of how much less probable it is for these values to have generated the data is not immediately evident.

In either case it is important not only to vary each of the parameters independently, but also in groups. The surface in parameter

space defined either by the sum of the squares (Equation 7.43) or of the Likelihood function (the summation term of Equation 3.46) may be curved in such a way that a long trough of near-extremum values may extend in a direction which is not parallel to any axis. Thus while the second derivative with respect to any one axis such as $\partial^2/\partial\lambda^2$ and $\partial^2/\partial\epsilon^2$ may be large, suggesting a well defined minimum, another such as $\partial^2/\partial\xi^2$, where $\lambda=a\xi$, $\epsilon=b\xi$, may be very small. In other words, coupled changes between two or more parameters may provide fits nearly as good as the best fit. This would imply uncertainties in the fitted parameters are much larger than if the parameters were varied independently.

Any fitting routine is usually based upon variations in the parameters (the physics) while keeping the data fixed. In reality, it is the physics which is constant, and the data which varies from experiment to experiment. The difference is in most cases subtle, but can be significant.

A technique to understand the actual uncertainties in a fit, independent of the statistical distribution used to generate the fitting conditions has been developed by SAMUEL88a. With the assumption that the data and its statistical deviations are indeed described by the fitting function and the distribution f respectively, the method determines the actual probability distribution of fitted parameters for a given set of "actual" parameters. The method uses a Monte-Carlo simulation to generate a large ensemble of simulated experimental data. The ensemble represents a independent simulations of many atoms, and of all background processes included in the fitting function. For example, if one obtains from an initial fit a half-life, efficiency and

background rate, these three values are used to generate a large ensemble of simulated decay spectra. The fitting routine is used to generate a set of parameters for each member of the ensemble. For each of the parameters the distribution of fitted values represents what one might call the response function of the routine. The distribution should peak at the "correct" value used to generate the ensemble, and the width of the distribution represents the uncertainty. Thus true confidence limits can be set on each of the parameters, and one need not explicitly address the coupling between parameters.

VII.4 Beta-Delayed Charged Particle Measurements:

The emission of nuclear particles from a nucleus following beta decay was discussed in Sections III through V. The sum of the kinetic energies of the delayed particle and of the recoil represent the total decay energy, and thus the excitation energy of the state populated by beta decay, minus the threshold energy for this break-up. A careful measurement of the energy deposited in the silicon after beta-decay will give a spectrum with peaks which can be identified with the break-up of states populated by the beta decay. For example, the decay diagram for ^{18}N is shown in Figure 5.1, and the delayed alpha spectrum of Zhao89 is shown in Figure 5.2. Two peaks in the spectrum can be directly associated with the breakup of the third and fourth 1^- levels in ^{18}O.

Implantation of delayed charged particle emitters within silicon offers some advantages over other techniques where the activity remains in the target or is attached to a passive surface such as a rotating wheel or tape. One advantage is the ability to count how many ions were implanted, and another is the nearly full 4π Sr solid angle for

detection of the emitted charged particle. However, both of these advantages are slightly less than perfectly implemented, and there are many experimental considerations involved in producing a spectrum with good branching ratio information, energy resolution and energy calibration. These are discussed below.

VII.4.1 Normalization:

The connection between the number of counts in a peak such as those in Figure 5.2, and an actual experimental branching ratio depends on a number of factors. The efficiency for fixed cycle operation as discussed in section VII.3.3.2 will be addressed here. We will use the simple definition of extracted branching ratio:

$$BR = \frac{\text{Counts in Decay Peak / EFF (Decay Counting)}}{\text{Counts of ions / EFF (ion Counting)}}, \quad [7.49]$$

where EFF is the overall efficiency for the conditions in the subscript. This efficiency can be broken down into components which must be individually determined, then multiplied together to obtain the total efficiency.

The first efficiency is associated with fraction of the time that the system is in a "beam-off" mode so that decays can be observed. This cycle efficiency EFF_{cyc} is usually less than 50% and is given by Equation 7.31.

The time-structure of the dead-time of the data aquisition system must also be determined. Since the atoms produced at the beginning of a beam-on period are less likely to decay in the beam-off period than those produced at the end of the beam-on cycle, the dead-time at the end of the beam-on period must carry a higher weight than that near the

beginning. Also the beam-off dead-time at the beginning of the period is more important than that at the end. It is actually difficult to measure accurately the dead time at each instant in time. Instead, the average dead-time can be determined both for beam-on and for beam-off. A very close approximation to the time dependence of the dead-time would then be to distribute the dead-time within a period as the instantaneous count-rate within the period. Thus since most decays are observed at the beginning of the beam-off period, this is where most of the dead-time should occur. While this is obviously an approximation, if the dead-time correction is small (less than 5% for instance) then this approximation should give correct the count-rate for dead time to better than 1%.

While most ions come to rest within the active volumes of the silicon detectors, a small fraction will end up stopping in the front and back dead-layers of the detectors. In this case some of the ionization does not result in collected charge. Some will also stop in any air which might be between the detectors, unless of course the detectors are operated in vacuum. The distribution of particles throughout the various materials depends on many factors, but is typically uniform per unit areal density when the detectors are thin (50μm). One must estimate the efficiency with which the ions have been counted in each detector. It is always difficult to determine whether an ion comes to rest in the very back of one detector, or the dead-layer of the front of the following detector. One must measure or estimate the thicknesses of the dead-layers and extrapolate from the range distributions within the detectors. In the case of delayed alpha activity from ^{18}N, the range of alpha particles is short. However for

^{18}N which come to rest near either face of the silicon, there is a chance that the alpha will be emitted toward the face and escape without depositing all of its energy within the silicon. This efficiency will vary dramatically with distance to the face. ZHA089 have used a Monte-Carlo simulation to understand the loss of counts form the peak in the alpha spectrum from this mechanism. Distortions of the peak-shape by the escape of particles are discussed in section VII.4.5.

If the stopping of ions within the air between detectors poses a problem to the experiment such as background and uncertainties in the efficiency, one can replace the atmosphere near the detectors with an equal pressure of helium. This can be accomplished by simply placing a large plastic bag around the detectors leaving two openings for the helium. A small flow of helium gas into one opening, and an equal flow of excess helium out of the other passage will maintain a density one roughly eight that of normal air, solving 87% of the problem of absorbtion in air with 1% of the trouble of a vacuum system.

VII.4.2 Energy Calibration:

One must also determine the relationship between the energy loss in the silicon and a given pulse height transmitted to the ADC in the acquisition system. In air, or even Helium, alpha sources placed near the silicon will loose too much energy in the gas and not produce pulses of accurately known energy in the silicon. Most alpha sources available will emit alpha particles only in the region of 5 to 8 MeV, while delayed charged particles can be emitted over a much broader range. The ground-state breakup of ^{9}B following ^{9}C beta decay releases only 0.3 MeV, while the decay of the T=0, T=1 doublet in ^{8}Be following the decay of ^{8}B can releases over 16 MeV. Table 7.1 contains a list of

potential calibration decays of light isotope which if periodically implanted in the detectors throughout an experiment can provide an internal calibration. However, before the calibration is assumed to represent the limits of the precision in energy of the detector and electronics, one must consider recoil effects from the beta and neutrino emission, and any pulse-height defect. The recoil problem is addressed in WARBURTON87, and the pulse-height defect is discussed in section VII.4.3.

As an alternative or supplement to internal calibration of the experiment one may use calibrated capacitors. The quantity of charge collected from a given amount of energy deposited in silicon is well know and is a natural property of silicon. By charging a capacitor of known capacitance to a measured voltage one can inject a known amount of charge into the silicon detector pre-amplifier. Since the average energy loss resulting in the production of an electron-hole pair is nearly a constant of the material at the 1% level (See section III.3.3), capacitors used for such a purpose are usually calibrated in MeV per Volt. The response is dependant on many parameters in the electronics, such as shaping time of the amplifier and capacitance of the detector itself. Long, high count-rate experiments may change the capacitance of the silicon detector from radiation damage and alter the energy calibration. It is therefore good practice if possible to continuously check the calibration for experiments which require a high degree of accuracy in the energy measurements.

Table 7.1 Some useful narrow beta delayed charged particle lines of known summed charged particle energies which might be incorporated in an energy calibration. Not listed is the isotope ^{9}Li. The beta delayed 2α + neutron decay channel of the 5/2^{-} level in ^{9}Be at 2.34 MeV produces a broad charged particle energy spectrum which collapses to a narrow peak if the neutron energy is detected and added. This state also decays through n + ^{8}Be, giving a narrow neutron energy peak. ^{16}C decay also provides narrow neutron lines for calibration of neutron detectors. The nucleus ^{16}N is a candidate for narrow neutron lines - see ZHAO89.

Parent Isotope	Decay Channel	Sum Energy (MeV)	Half life (sec)	Branch (%)	Reference(s)
^{11}Be	^{7}Li + α	1.21	11.8	2.5	ALBURGER81 and MILLENER82
	^{7}Li* + α	0.73		0.4	
^{8}B	2α	16.76	0.77	small	WARBURTON86
^{12}B	3α	0.38	0.020	1.5	BARNES73
^{9}C	2α + p	0.28 2.64 12.1 ?	0.13	60 17	MIKOLAS88a
^{12}N	3α	0.38	0.011	2.7	SCHWALM66
^{18}N	^{14}C + α	1.39 1.81	0.90	6.8 1.8	ZHAO89, OLNES82
^{13}O	^{12}C + p	1.57	0.008	11	ESTERL70 and ASAHI89

VII.4.3 Pulse Height Defect:

There are several effects which can decrease the peak height associated with a given amount of energy deposited in the silicon. These are grouped together under the term pulse height defect. The most important effect related to delayed charged particle spectroscopy in light nuclei implanted within silicon is that of energy loss of the delayed particle and recoiling nucleus by non-ionizing processes. When ^{18}N decays to alpha-unbound levels in ^{18}O for instance, the decay of the excited state result in an alpha particle and a recoiling ^{14}C nucleus. They share the break up energy, in the ratio of approximately 14/18 to 4/18. Thus when the third 1^- level in the daughter ^{18}O breaks up giving 1.3 MeV to the particles, the ^{14}C nucleus carries less than 0.3 MeV. It is moving so slow that a significant fraction of its energy loss will be to non-ionizing process such as elastic atomic scattering from silicon atoms which can knock the atoms out of the lattice. This process dissipates a large amount of energy without the production of an electron-hole pair.

Energy loss to non-ionizing processes can result in a signal of perhaps 1.2 MeV instead of 1.3, and could result in the misidentification of a level in some cases. For protons and alphas, the defect will be of the order of a few keV but for heavier particles the defect rapidly increases. For example, when heavy ($A \approx 200$) alpha emitters are implanted within silicon, the alpha particle is the only to cause ionization; the energy of the recoil is ignored, as it loses essentially none of its energy to ionization.

Even for the energy loss which does produce ionization there are effects which can prevent this charge from being properly collected and

from properly contributing to the height of the resulting pulse to the ADC. For slow, highly ionizing particles the density of electrons and holes in the silicon is much greater than for fast, less-ionizing particles. Once the electrons and holes begin to separate they produce a space-charge which cancels the electric field imposed by the bias of the detector. This prevents further separation of the holes and electrons until the space-charge is reduced by collection of the few charges which have been moved to the outside edges of the cloud. This has two effects on the pulse height. The first effect results from a change in the rise and decay times of the charge pulse from the detector. The amplifier is usually adjusted to have a response in frequency space that is peaked at one frequency, and drops off to zero at lower and higher frequency. Thus any change in the peak shape will also change the power and/or phase spectrum at the input of the amplifier and will usually change the output amplitude. This is analogous to the changes in gain observed when the capacitance of the detector is altered by radiation damage.

The second effect of the high charge density resulting from highly ionizing particles is that of recombination. The longer that the electrons and holes occupy the same volume of silicon, the more chance there is for the destructive recombination of an electron-hole pair into phonons, and a resulting decrease in the pulse height at the ADC.

Thus in performing delayed charged-particle spectroscopy where energies must be accurately measured, many effects must be considered when comparing calibration standards or calibrated capacitors to decays where heavier recoils deposit a fraction of the energy with low velocity and high ionization density.

VII.4.4 Line Shape Distortion from Beta Energy Loss:

In section VII.3.1, the energy loss of the beta particle in the silicon was the source of information for the experiment, and the discussion centered around how to maximize this signal. Here, the energy loss of the beta is a contaminant and must be minimized. While the contribution can never be completely removed when the activity lies within the active volume of the silicon, there are many ways to reduce the energy loss or subtract it afterwards during analysis of the data.

The spectrum of energy loss from a source of beta activity within a silicon detector of finite thickness is difficult to calculate. The decay produced betas of all energies between zero and the full available energy. Each energy beta will have different energy-loss and multiple scattering behavior. However for most decays the energy loss of a beta in silicon can be fairly well approximated as 0.5 MeV per mm (1.5 MeV/g/cm^2). If one ignores the possibility of polarization or alignment from the heavy ion reaction being maintained in the silicon resulting in an angular distribution of the betas with respect to the orientation of the silicon wafer (a fairly safe assumption but not guaranteed), then the betas can be assumed to be emitted isotropically. With the angle θ defined as the angle between the normal to the surface of the detector and the direction of the beta, isotropic emission can be expressed as

$$\frac{d^2P}{d\cos\theta\, d\phi} = \frac{-1}{4\pi} . \qquad [7.50]$$

With

$$\frac{dP}{d\phi} = \frac{1}{2\pi}, \qquad [7.51]$$

Equation 7.50 can be integrated over ϕ, giving

$$\frac{dP}{d\cos\theta} = \frac{-1}{2} . \qquad [7.52]$$

When the beta emitted from a point a distance L_o from the surface of the detector passes through that surface, it has traveled a distance L and deposited and energy E in, where

$$L = \frac{L_o}{\cos\theta} \text{ , and } E = \frac{dE}{dX} L \text{ .} \qquad [7.53]$$

Using the chain rule, the expression for the probability of energy loss is

$$\frac{dP}{dE} = \frac{dP}{d\cos\theta} \frac{d\cos\theta}{dL} \frac{dL}{dE} \text{ .} \qquad [7.54]$$

Through substitution, one can obtain

$$\frac{dP}{dE} = \frac{L_o}{2L^2} \left(\frac{dE}{dX}\right)^{-1} \text{ .} \qquad [7.45]$$

When expressed as a function of energy only, and the physical limits are included, the final result is

$$\frac{dP}{dE} = \begin{cases} \frac{E_o}{2E^2} & E \geq E_o \\ 0 & E < E_o \end{cases} \text{ .} \qquad [7.46]$$

The integral of Equation [7.46] gives a total probability of 0.5 for leaving each of the surfaces. In an actual experiment, the beta emitters can be distributed at all values of L_o from zero to the full thickness of the detector. This distribution must be taken into account before the actual distortion of the line-shape is simulated.

There are two important differences in the degradation of the line-shape between the beta energy-loss mechanism, and simple Gaussian noise. The first is that the beta energy loss shifts the peak to higher energy by a constant offset depending on the range distribution of the ions and the thickness of the detector, while the simple noise will not alter the peak position in a linear system. The centroid of a line-shape generated from Equation 7.45 can not be defined mathematically, since the energy-weighted integral diverges. However, in

practice a centroid will be finite. The maximum amount of energy that a beta can actually deposit in the silicon is determined by a combination of the maximum energy of the beta itself, the diameter of the silicon (we have assumed an infinite slab) and the irreversible scattering of the beta out of the detector before it loses all of its energy.

The second important difference is the interference with higher energy weak peaks by a lower energy strong peak. Thinner detectors will decrease the high-energy tailing from the beta energy loss, but the increased capacitance will broaden the symmetric Gaussian lineshape from the electronic noise of the detector system. Monochromation of the ions (see section VI.3) will greatly increase the number of ions which stop in a detector which has been chosen for its thinness.

The shape of the energy loss spectrum of the electrons is dependent on the details of the range distribution of the ions. Figure 7.9 shows a simulation for a source at two positions in the detector, one source is in the center and the other is implanted at a depth of only 10% of the thickness of the detector. For a given beta energy threshold, these two sources would have different efficiencies for triggering an event in a half-life experiment.

Techniques to measure and subtract the beta energy loss, or to limit it to a well defined set of energies are discussed in section VII.4.6.

VII.4.5 Line Shape Distortions from Escaped Charged Particles:

In the case of ^{18}N the range of the alphas in silicon was small compared to the thickness of the detectors used, and the escape of the alphas before losing their total energy was a small effect on the

spectrum and required only a small correction to the area of the peaks in the data analysis. In other cases much longer range particles are emitted and require thicker detectors to contain and record the full energy.

In the case of ^{9}C beta-delayed protons of almost 11 MeV were expected. These have a range of roughly one millimeter in silicon. This is close to the total range of the incoming ^{9}C ions from the RPMS! If 100% containment were to be achieved a detector well over 2mm thick would be required. However with this thickness the degradation of the spectrum from the beta energy loss would be absolutely unacceptable. A compromise was reached and ^{9}C ions were implanted in both a 0.4 mm thick detector and a 1mm detector.

As can be seen in Figure 4.3, the shape of the energy loss spectrum for high energy protons-Bragg curve results in the bimodal distribution of energies deposited in the silicon. This is a particularly troublesome distribution, as it causes a second peak to appear which has nothing to do with the decay of a second excited state in the daughter. In Figure 4.3 the actual recorded spectrum of delayed particles from ^{9}C is also shown. A peak at 12 MeV is evident. It contains counts from at least three different decay mechanisms which produce two alpha particles and a proton with combined energies of 12 MeV, but shared in very different ways. See section IV for a discussion of the decay of ^{9}C and distribution of energy between the the three particles.

VII.4.6 Multi-Element Detector Systems, Coincidences:

In sections VII.4.4 and VII.4.5 above, the difficulties associated with choosing the correct thickness of a detector are outlined. With

the addition of two more silicon detectors directly in front and behind the detector containing the decay events both problems can be addressed.

Mikolas88a describe a technique to subtract the energy loss of the beta event by event by measuring the energy loss in a parallel detector. The detector arrangement is shown in that reference. During analysis of the data, the presence of a signal in E1, E2 and E3 are all required after a ^{9}C ion comes to rest in E1. Since a signal is observed in E3, the beta must pass completely through E2. The distance from the ^{9}C position to the back surface of E1 can be determined from the range-energy relationship for the incoming ^{9}C event. If one assumes that the dE/dX and direction of the beta is constant then through the use of similar triangles, one can show

$$\Delta E1 = \frac{T_{E1} - R}{T_{E2}} \times \Delta E2, \qquad [7.57]$$

where $\Delta E1$ and $\Delta E2$ are the energy loss of the beta particle in E1 and E2, T_{E1} and T_{E2} are the thicknesses of the two detectors, and R is the range of the ^{9}C ion measured from the front of the detector. If for each decay event the value of $\Delta E1$ is subtracted from the energy recorded in E1, then the long tail of the beta energy distribution can be suppressed. As shown in MIKOLAS88a the spectrum recorded in E1 near 3 MeV is shown without any modification. Also shown is the subtracted spectrum. While it contains only a small fraction of the total number of counts, the narrow state at 2.36 MeV is better separated from the underlying broad state, which is nearly invisible in the raw data. Part of the suppression comes simply from restricting the direction that the beta particle travels. In order to reach E3 it must leave E1

close to the normal of the detector. This would truncate the tail to some maximum energy in a simple model. While the determination of the energy loss in E2, and the scaled subtraction from the energy in E1 further improves the peak shape, any method to restrict just the direction of the beta will significantly improve the resolution of a beta-delayed charged particle experiment.

Multi-element detector arrays can also be used to gain more information on high energy particles which can leave the silicon in which the decay originates. The efficiency of a proton leaving one detector and entering the next is difficult to accurately determine and is usually of the order of only 20%. This may however aid in the identification of the particle decay modes of a state. In the case of ^{9}C decay, very few events were recorded where more than 2 MeV was deposited in each detector and the sum was near 12 MeV. This implies that the state at 12 MeV emits a high-energy and thus long range proton capable of entering another detector at best a small fraction of the time. This is consistent with other observations of this state, as described in Section IV.

APPENDICES

APPENDIX A

BETA DECAY BRANCHING RATIOS OF ^{9}C TO LOW LYING STATES IN ^{9}B

Reprinted from: Physical Review C, Vol. 37, No. 2, February 1988

Branching ratios of ^{9}C to low lying states in ^{9}B

D. Mikolas, B. A. Brown, W. Benenson, L. H. Harwood, E. Kashy, J. A. Nolen, Jr., B. Sherrill, J. Stevenson, J. S. Winfield, and Z. Q. Xie

R. Sherr

PHYSICAL REVIEW C VOLUME 37, NUMBER 2 FEBRUARY 1988

Branching ratios of ^{9}C to low lying states in ^{9}B

D. Mikolas, B. A. Brown, W. Benenson, L. H. Harwood, E. Kashy, J. A. Nolen, Jr., B. Sherrill, J. Stevenson, J. S. Winfield, and Z. Q. Xie
Department of Physics and Astronomy and National Superconducting Cyclotron Laboratory, Michigan State University, East Lansing, Michigan 48824

R. Sherr
Department of Physics, Princeton University, Princeton, New Jersey 08540
(Received 7 May 1987)

We report the first observation of the beta decay of ^{9}C to the ground state and to two low-lying excited states of ^{9}B. Branching ratios to these states were measured, and a previously reported branch to a level near 12 MeV was confirmed. The branching ratio to the $J^\pi = \frac{3}{2}^-$ ground state is 60 ± 10 %, and the branching ratios to the narrow $\frac{5}{2}^-$ level at 2.36 MeV and to the broad $\frac{1}{2}^-$ level near 2.9 MeV are 17 ± 6 % and 11 ± 5 %, respectively. Because of the three-body nature of the ^{9}B decay, the ^{9}C ions were implanted in the active volume of silicon detectors, and the total decay energies of the states in ^{9}B were directly measured. We compare these results to shell model calculations, to the analog decay of ^{9}Li to ^{9}Be, and to the ^{9}Be(p,n)^{9}B reaction. The comparison to ^{9}Li decay indicates an asymmetry in the beta-decay matrix elements to the $\frac{5}{2}^-$ level larger than any such asymmetry previously observed.

I. INTRODUCTION

The beta-delayed proton precursors with $T_z = -\frac{3}{2}$, $A = 4n + 1$ ($n = 2, 3, \ldots,$) have been extensively studied, and delayed proton activity from every member of this group from ^{9}C to ^{61}Ge has been measured.[1,2] Most delayed proton spectra from these nuclei show a complicated structure with many peaks, reflecting transitions to discrete narrow levels. In the case of ^{9}C, (see Fig. 1) the delayed proton spectrum is dominated by a continuum of proton energies.[3,4] In addition, the data below about 3 MeV of Refs. 3 and 4 were contaminated by electron pileup.[5] This prevented the measurement of most of the experimental beta decay strength to ^{9}B, which is expected to lie below this experimental cutoff. Furthermore, the ^{9}C beta-delayed proton spectrum is difficult to interpret itself, because unknown fractions of the decay energy are carried away by the two alpha particles. The decay of the ground state of ^{9}B generates a proton with a kinetic energy of only 0.16 MeV,[6] and the first negative-parity excited state ($\frac{5}{2}^-$ at 2.360 MeV), while it is relatively narrow, decays less than 1% of the time by proton emission to the ground state of ^{8}Be.[7] It instead decays mainly through broad intermediate states leading to a continuum of proton energies.

The problem of the spread in proton energies becomes worse for the higher excitation energies. More decay channels (which can involve excited states in the intermediate fragment) become energetically allowed, and enough phase space becomes available for many of these channels to be populated with significant probability. In this case the proton energy spectrum does not directly reflect the excitation spectrum in ^{9}B, since all paths involve decays to three particles (2α + p). Even for a fixed excitation in ^{9}B, different particle decay channels which involve states in ^{8}Be and ^{5}Li will generate different proton spectra that can be quite broad. The breakup of the ^{9}B nucleus promptly into three particles is also possible. Therefore, to measure the branching of ^{9}C decay requires a method that detects the population and excitation energies of the ^{9}B levels directly, independent of the decay modes of these states.

In the present experiment, we used the technique of implantation of the delayed particle precursor, ^{9}C, within a silicon detector. This method was first used by Chen *et al.*[8] to investigate the decay of ^{9}Li, the mirror nucleus of ^{9}C. In that experiment, the excited states of ^{9}Be decayed to 2α + n, but only the sum of the two α particle energies was measured. The delayed neutron energy spectrum was recorded in a separate experiment.[8] The excitation energy spectrum in the ^{9}Be nucleus could be inferred from the data only with the use of specific assumptions about the particle decay for each state. The implantation technique was also used by Barnes and Nichols[9] to make a precise measurement of the β-delayed breakup of the second excited state of ^{12}C into three α particles. In this case, as in the case of ^{9}B decay, all the decay particles are charged, and as long as they are completely contained in the silicon, the total decay energy of the nucleus is measured, independently of the decay mode.

The energy deposited in the detector in which both the ^{9}C nucleus decays and the ^{9}B decay fragments stop is the sum of the excitation energy of the ^{9}B nucleus, of the ground state breakup energy of ^{9}B (0.28 MeV), and of a small contribution from the energy loss of the beta particle. Because of the low energies of the alpha particles and the proton, the fraction of the energy loss to nonionizing processes in the silicon must be considered, since these processes will not contribute to the measured ener-

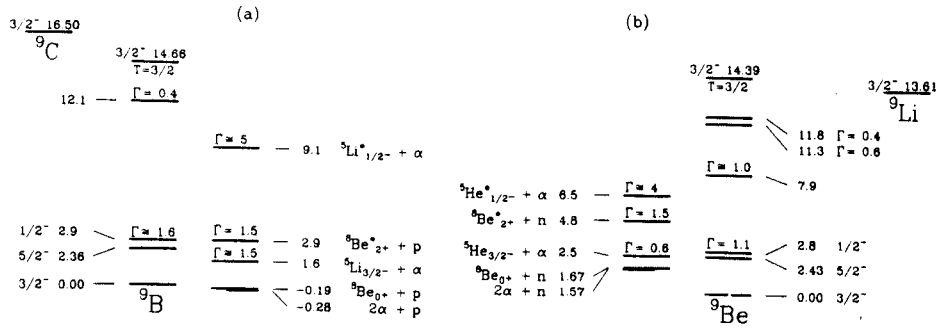

FIG. 1. Relative mass and excitation energies of known and presumed $\frac{1}{2}^-$, $\frac{3}{2}^-$, and $\frac{5}{2}^-$ levels, relevant to beta decay in mass 9, and particle decay thresholds of those levels. All energies in (a) are relative to the ground state mass of ^{9}B (atomic mass excess 12.4158±0.001 MeV) and those in (b) are relative to the ground state of ^{9}Be (11.3477±0.0004). All ground state masses are taken from Wapstra *et al.* (Ref. 58). Energies and widths of excited states are all from Ajzenberg-Selove (Ref. 6), except those of the 2.9 and 12.1 MeV levels in ^{9}B, which are discussed in the present work.

gy in the silicon. We estimate that this pulse height defect should lie between 2 and 8 keV per particle[10,11] (depending on the lab energy of each), and results in only a slight broadening of the peaks that will not significantly affect the following analysis. Since the direction of the particles with respect to the silicon crystal axes cannot be controlled, large pulse height anomalies are possible for particles which channel in the silicon lattice. We assume that the probability of emission of a particle in a direction sufficiently close to any channeling axis is small.

We have expanded upon this technique by using a multidetector telescope. This provides a way to subtract the contribution of the beta particle from the spectrum and thus allows the use of thicker detectors to contain the charged particle energy. It also provides a simple way to check on the containment of charged particles and a potential method to distinguish different decay modes.

The delayed proton data of Hardy *et al.*[3] and Esterl *et al.*[4] contain peaks at roughly 9 and 12 MeV center-of-mass energy, based on the proton decay to the ground state of ^{8}Be. These could originate from the decay of two different states in ^{9}B, or a single state at 12 MeV which proton decays to both the ground state and first excited state of ^{8}Be (as suggested by the authors). Since our technique measures the excitation in the ^{9}B nucleus directly, there can be no ambiguity of this type. The implantation technique also allows the number of nuclei imbedded in the silicon to be counted, which permits absolute branching ratio measurements.

In the following section, we will describe the experimental procedure of obtaining the beta-delayed charged-particle spectra for ^{9}C decay. In Sec. III we outline the details of the analysis of the data, and methods and assumptions used in obtaining the branching ratios. In Secs. IV and V we discuss previously published data on the beta decay of ^{9}Li and the ^{9}Be(p,n)^{9}B reaction, respectively. In Sec. VI, shell model calculations of beta-decay rates of ^{9}C and ^{9}Li, the ^{9}Be(p,n)^{9}B relative cross sections, and the beta-delayed particle decay modes in the mass 9 system are presented. We discuss the connections between all of these data and calculations in Sec. VII, and conclude with suggestions for further experiments in Sec. VIII.

II. EXPERIMENT

A 91 mg/cm^2 Ni target was bombarded by an $E/A=35$ MeV $^{12}C^{4+}$ beam from the $K=500$ cyclotron at the National Superconducting Cyclotron Laboratory. The Reaction Product Mass Separator (RPMS) (Refs. 12 and 13) was used to separate ^{9}C fragments from the other reaction products emerging at a scattering angle of 3°.

A thin kapton window separated the vacuum of the RPMS from the focal plane, which is in air. The focal plane of the RPMS was equipped with slits to select particles of a given mass/charge ratio (m/q), a position-sensitive proportional counter, and a four element silicon detector telescope. The telescope is schematically illustrated in Fig. 2. It consisted of two 400 μm thick surface barrier detectors and two lithium drifted silicon detectors with thicknesses of 1 and 5 mm. These will be referred to as ΔE, $E1$, $E2$, and $E3$, respectively. The energy response of the electronics was measured to 5% accuracy by means of a calibrated pulser.

Approximately 6000 ^{9}C ions stopped in $E1$, and 4000 in $E2$ in 12 h of data taking with an average beam current of 60 nA. Ions were identified by their energy loss in each detector. The identification was verified by an m/q determination from focal plane position. Other ions which stopped in the detectors were mostly ^{8}B nuclei or scattered beam particles ($\sim$2000 and $\sim$5000 events, respectively). The implanation depth profile of the ^{9}C ions in the silicon was adjusted by means of aluminum absorbers in front of the defining slits so that any variation in the containment of high energy protons could be explored. The range distribution of ^{9}C ions calculated from the total energy measurement is also illustrated in Fig. 2.

The cyclotron beam was turned off within 40 μs of the arrival of an ion (by means of a fast phase shifter in the

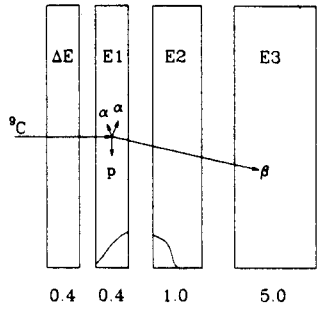

FIG. 2. A schematic diagram of the silicon detector telescope used at the RPMS focal plane. A ^{9}C ion is identified in the telescope, and comes to rest in $E1$ or $E2$. When ^{9}C decays, the β particles, with energies distributed between 0 and 15.5 MeV, usually leave the silicon detector in which the decay occurs, and sometimes enter other elements. The daughter nucleus, ^{9}B, always breaks up into two α particles and a proton. The implanted ^{9}C range distribution is indicated in the bottom of $E1$ and $E2$. The thicknesses of the detectors in mm are indicated under each element.

rf transmitter of one of the three "dees" of the cyclotron), and the gain of the silicon detector preamplifiers increased by a factor of 10 for a 480 ms period, approximately four half-lives of ^{9}C. The detection of an ion in the focal plane telescope will be referred to as a "beam-on" event, and all events during the following 480 ms period as "beam-off" events. After the beam was turned off and the preamplifiers allowed to stabilize (16 ms), a beam-off event was triggered by signals above a discriminator level, set near 200 keV, from any one of the last three silicon detectors. A scaler module that counted

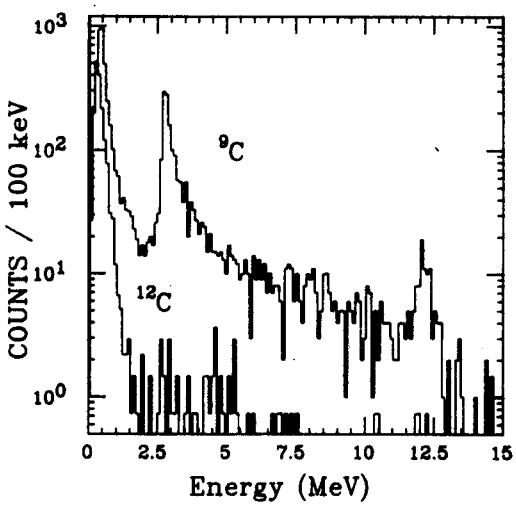

FIG. 3. The beam-off energy spectra associated with ^{9}C and ^{12}C ions recorded in $E1$. The spectrum associated with ^{12}C has been normalized to the same number of beam-on events as the ^{9}C spectrum.

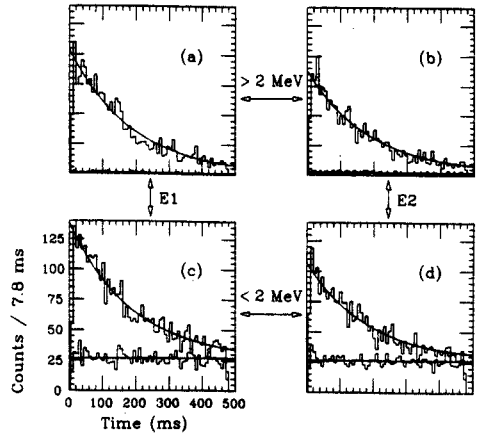

FIG. 4. Time spectra of beam-off events after the arrival of ^{9}C ions in $E1$ and in $E2$, in which the signal in that detector was above or below 2.0 MeV. For each of the four combinations, a histogram of events following the arrival of a ^{12}C is also included, to illustrate the background rate. The smooth curves are not direct fits to these data. They are described in Sec. III.

pulses from a 262 kHz quartz oscillator was cleared by a beam-on event, and was read but not cleared for the subsequent beam-off events. Thus the time between the beam-on event and each of the following beam-off events could be determined. The data were recorded event by event on magnetic tape. Each beam-on event could be directly matched with the set of subsequent beam-off events during off-line analysis.

III. ANALYSIS

The energy spectrum of beam-off events for which a ^{9}C ion stopped in $E1$ is shown in Fig. 3. The beam-off spectrum associated with ^{12}C ions, normalized to the same number of beam-on events, is also included in the figure. The ^{12}C spectrum was used to define the background spectrum. Sources of background include residual beta activity within and near the silicon detectors and electrical noise.

Time spectra of events in each detector associated with ^{9}C or ^{12}C are shown in Figs. 4(a)–4(d). The events are further divided into groups of those for which the beam-off signal in the detector of interest was above and those for which it was below 2 MeV. The area of the corresponding regions in the decay spectra in $E1$ and $E2$, associated with ^{9}C and ^{12}C, above and below 2 MeV were used to generate constant-background and exponential-plus-constant-background curves, and these results are superimposed on the data in Fig. 4. The area of the appropriate region from the normalized ^{12}C associated energy spectrum, shown in Fig. 3, is used for the constant background measurement, while the difference between the areas from the ^{9}C and the normalized ^{12}C spectrum is used to determine the coefficient of the exponential decay. The previously-measured half-life[4,6,14]

of 126.5±1.0 ms is used throughout this analysis. As can be seen in Fig. 4, the agreement is good. This indicates that the background is indeed independent of time, and that the separate contributions to the energy spectra from ^{9}C and background have been determined correctly.

The efficiency of the system for the detection of the decay of ^{9}C nuclei was 87% in $E1$ and 94% in $E2$, after correction for finite counting time and dead time. The missing decays are ascribed to the decay of ^{9}B in its ground state, where the total energy released was small, and near the thresholds of the constant fraction discriminators used in the experiment.

The $E2$ detector is much thicker than $E1$, and most of the ^{9}C ions that entered it came to rest close to its front surface. The beta particles leaving $E2$ through the front traversed only a few hundred microns of silicon, while those leaving the back, a minimum of 800 μm. This makes the peaks in $E2$ (not shown) broader than their counterparts in $E1$ (Fig. 3) by shifting half of the events higher in energy by about 300 keV on average. If our description of the threshold problem is correct, about half of the counts in $E2$ associated with the decay to the ground state should then lie well above the threshold level of the constant fraction discriminator, in a region where the efficiency problem should not occur. This would make the number of undetected decays in $E2$ roughly half of that in $E1$, which conforms with the measured efficiencies, and supports the conclusion that the missing counts are associated with the ground state branch.

Shell model calculations (discussed in Sec. VI) indicate that the decay of ^{9}C should most often populate the three lowest negative parity states in ^{9}B (including the ground state) with roughly equal Gamow-Teller strength. (See Table I.) However, of these three levels, only the ground state and one excited state branch are evident in Fig. 3. While the ground state[15] and first $\frac{5}{2}^-$ level[7] in ^{9}B are narrow, it is reasonable to believe that the first $\frac{1}{2}^-$ level in ^{9}B is broad. As discussed in Sec. V, there is evidence for this broad state near 2.7 MeV in the ^{9}Be(p,n)^{9}B spectrum. In the mirror nucleus ^{9}Be, the level near 2.9 MeV has a width of roughly 1.0 MeV. (See Table II for both nuclei.) The decay of ^{9}C to a level in ^{9}B with a width of 1.5 MeV would be obscured in our spectrum by the beta energy loss associated with the nearby $\frac{5}{2}^-$ state. Two techniques described below were developed to reduce this effect in order to search for this broad level.

A simulation of the beta energy-loss spectrum was generated by a Monte Carlo routine based on the relation[9]

$$P(E)\delta E = \begin{cases} \dfrac{E_0}{E^2}\delta E, & E \geq E_0 \\ 0, & E < E_0 , \end{cases} \tag{1}$$

where $E_0 = D(dE/dX)_\beta$, and D is the distance from each implanted ion to the face of the silicon detector from which the beta particle will emerge, as calculated from the beam-on energy of the implanted ion. An effective $(dE/dX)_\beta$ of 0.5 MeV/mm in Si was found to fit the energy loss in $E1$ and $E2$ from decays in $E1$. This value is about 30% larger than that for a minimum ionizing particle in Si, but, as determined by Barnes and Nichols,[9] a larger value is expected due to multiple Coulomb scattering in the finite thickness of the detector. The distribution was further broadened to take into account the variability in the pulse height defect associated with the distribution of energies of the three particles, an intrinsic 100 keV resolution of the silicon detec-

TABLE I. Measured and predicted Gamow-Teller beta decay strengths to the lowest $\frac{3}{2}^-$, $\frac{5}{2}^-$, and $\frac{1}{2}^-$ states in mass 9. (BR) denotes branching ratio.

Reference	$\frac{3}{2}^-$ (ground state) BR (%)	B(GT)[a]	$\frac{5}{2}^-$ BR (%)	B(GT)[a]	$\frac{1}{2}^-$ BR (%)	B(GT)[a]
		^{9}C experimental				
This work	60±10	0.033±0.006	17±6	0.020±0.007	11±5	0.016±0.007
		$A=9$ shell model calculations				
(6–16) 2BME (Ref. 35)		0.035		0.030		0.016
Millener (Ref. 36)		0.046		0.028		0.020
Kumar (Ref. 37)		0.014		0.066		0.010
(8–16) POT (Ref. 35)		0.086		0.039		0.080
		^{9}Li experimental				
Nefkens *et al.* (Ref. 57)	60±10	0.036±0.006				
Macefield *et al.*[b,c] (Ref. 21)			33±5	0.051±0.008	17±5	0.032±0.009
Chen *et al.*[b] (Ref. 8)	$65.0^{+2.7}_{-2.4}$	0.039±0.002	$32.0^{+2.7}_{-3.7}$	$0.049^{+0.004}_{-0.006}$	$3.0^{+2.7}_{-0.3}$	$0.006^{+0.005}_{-0.001}$
Björnstad *et al.* (Ref. 26)	50±4	0.030±0.002				
Langevin *et al.*[b] (Ref. 27)	50.5±5	0.030±0.002	34±4	0.052±0.006	10±2	0.019±0.004

[a] B(GT) values are calculated from Eqs. (3) and (4) of Sec. III.
[b] See Table II for the assumed particle decay branches of these states used by each author to extract a measured branching ratio.
[c] The listed branching ratios have been adjusted from the published values for a ground state branch of 50% as described in the text. The B(GT) values are calculated (see footnote a) based on the adjusted branching ratio.

tor and associated electronics, and the width of the particular state.

The solid line in Fig. 5 shows the simulation of the peak shapes for the branches to the ground state and $\frac{5}{2}^-$ level, with about 2450 and 900 decays, respectively, in $E1$. The difference between the ^{9}C decay data (after background subtraction) and the simulation is shown in the inset. While the subtraction leaves almost 0 counts in the vicinity of the ground state decay, a broad residual yield near 3 MeV is clearly evident. This gives a ratio of strengths between the decay to the $\frac{5}{2}^-$ state, and of the decay to the energy range of 2.0 and 4.4 MeV in the subtracted spectrum (not including the $\frac{5}{2}^-$ state) of 1.9. This broad distribution probably represents the population of the $\frac{1}{2}^-$ level in ^{9}B discussed above.

To confirm the presence of the broad level, and to better separate the strength from that of the $\frac{5}{2}^-$ level, a corrected energy spectrum of ^{9}C decay in $E1$ was generated. This was accomplished by modifying the off-line analysis code to require the beta particle to pass from $E1$ through $E2$ and into $E3$. In this case the effective energy loss of each beta in a detector with a thickness of 1 mm was measured for each event by the signal in $E2$. The contribution of the beta to be subtracted from the $E1$ signal for each event is scaled from the energy loss in $E2$ for that event by

$$\Delta E1_\beta = \frac{(400\mu - \text{Range})}{1\text{ mm}} E2 , \quad (2)$$

The corrected $E1$ spectrum is histogrammed, and is shown in Fig. 6 after background subtraction (the background was generated by applying the same process to the ^{12}C data). Here the broad state clearly shows up. The lack of a similar structure above the ground state rules out any anomalous beta energy loss tail as the source of the broad distribution. These data suggest that the $\frac{5}{2}^-$ level is populated 1.1 times as frequently as the $\frac{1}{2}^-$ level. In order to determine this ratio, we have assumed that the two peak channels near 2.5 MeV in Fig. 6 contain all of the $\frac{5}{2}^-$ strength, and that the contribution to these two channels from the decay of the $\frac{1}{2}^-$ level is equal to the sum of the two channels immediately above and below the two peak channels. Combining this with the previous value, we estimate that the true ratio of $\frac{5}{2}^-$ to $\frac{1}{2}^-$ branching is 1.5±0.5. The error bars are not statistical in origin, but were chosen to be consistent with both measurements, reflecting the uncertainty in the methods used to separate the strength to the $\frac{1}{2}^-$ from that of the $\frac{5}{2}^-$.

In order to obtain the actual branching ratio for the $\frac{5}{2}^-$ level, the number of counts used in the simulation of Fig. 6 are multiplied by a factor of 1.16 to correct for finite counting time and dead time, and then divided by 6116, the number of implanted ^{9}C ions. We have estimated the error in the resulting branching ratio based upon uncertainties in the subtraction of the simulated beta energy-loss spectrum. The branching ratio to the

TABLE II. Observed excitation energies, widths, and nucleon decay branching ratios to the ground state of ^{8}Be for the first three negative parity levels in ^{9}Be and ^{9}B.

J^π	Nucleus	E_x (MeV)	Γ (keV)	Fraction of decays to $^8\text{Be}_{\text{g.s.}}$ + nucleon (%)	Reference
$\frac{3}{2}^-$	^{9}Be	0.00	stable		
$\frac{3}{2}^-$	^{9}B	0.00	0.5±0.02		Teranishi and Furubayashi (Ref. 15)
$\frac{5}{2}^-$	^{9}Be	2.43	0.77±0.15		Ajzenberg-Selove (Ref. 6)
$\frac{5}{2}^-$	^{9}Be			≦10	Bodanski *et al.* (Ref. 59)
$\frac{5}{2}^-$	^{9}Be			13±3.0	Mösner *et al.* (Ref. 22)
$\frac{5}{2}^-$	^{9}Be			7.5±1.5	Christensen and Cocke (Ref. 60)
$\frac{5}{2}^-$	^{9}Be			6.4±0.12	Chen *et al.* (Ref. 8)
$\frac{5}{2}^-$	^{9}B	2.36	81±5		Ajzenberg-Selove (Ref. 6)
$\frac{5}{2}^-$	^{9}B			≦1.0	Wilkinson *et al.* (Ref. 7)
$\frac{1}{2}^-$	^{9}Be	3.0±0.1	1000±200	(100)[a]	Macefield *et al.* (Ref. 21)
$\frac{1}{2}^-$	^{9}Be	2.78±0.12	1100±120	(100)[a]	Chen *et al.* (Ref. 8)
$\frac{1}{2}^-$	^{9}Be	2.9±0.25	1000±250	≧72	Adloff *et al.* (Ref. 54)
$\frac{1}{2}^-$	^{9}Be			≈30	Langevin *et al.* (Ref. 27)
$\frac{1}{2}^-$	^{9}B	2.6±0.1	1650±100		Fazely *et al.* (Ref. 32)
$\frac{1}{2}^-$	^{9}B	2.75±0.3	3130±200		Pugh (Ref. 33)

[a]These values have not been measured. They are assumptions used in each of these references for the analysis of the beta-delayed neutron spectra. See Sec. IV.

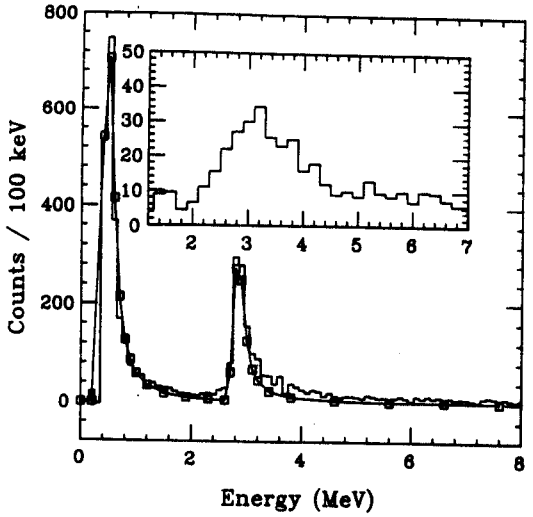

FIG. 5. The ^{9}C decay data recorded in $E1$ is shown in the figure as a histogram, and a simulated line shape for the ground state and narrow $\frac{5}{2}^-$ level is illustrated by the squares and solid line. Squares have been omitted from regions where the simulation is smooth. The simulation is subtracted from the data, and the difference is shown in the inset, where two channel averages are given.

$\frac{1}{2}^-$ level is found by scaling the branching ratio of the $\frac{5}{2}^-$ by a factor of $1/(1.5\pm0.5)$. The ground state branch is obtained in a similar manner to that of the $\frac{5}{2}^-$ level, except that an additional 14% is added to the resulting branching ratio to account for the less-than-unity efficiency of the constant fraction discriminator for the lowest amplitude pulses detected. The results are given in Table I. The beta-decay B(GT) values given in Table I are calculated using the following expressions:

$$ft = \frac{f(Q_B - E_x)t_{1/2}}{\text{branching ratio}} \tag{3}$$

and

$$B(\text{GT}) = \frac{6177\ \text{s}}{ft}\ . \tag{4}$$

The statistical rate function $f(Q_\beta - E_x)$ is calculated using the method of Wilkinson and Macefield.[16] No adjustments have been made for the widths of the states; the $\frac{1}{2}^-$ was treated as a narrow state at 2.9 MeV.

A peak near 12 MeV excitation in ^{9}B is evident in the spectra from both $E1$ (Fig. 3) and $E2$ (not shown). In contrast to the results of the delayed proton data,[3,4] no peak is observed near 9 MeV. The peak near 12 MeV in the present data is best described as a branch to a level with $E_x = 12.1\pm0.6$ MeV with a width of 400 ± 100 keV after broadening due to beta energy loss and resolution has been taken into account. The area under the peak within 800 keV of E_x represents 2.3 ± 0.5 % of the decay strength. The actual branch to this state may be larger, because additional strength to this state may be found far below the peak (i.e., up to ~25 FWHM units) in the present spectrum. This can be the result of two separate effects: one experimental—the escape of the highest-energy protons from the silicon; and one physical—a long low energy tail of the peak which can be understood as the effect of the Fermi statistical rate function on the low energy part of the Breit-Wigner distribution used to describe the state.[17,18] These effects depend greatly on the particle decay modes of the state, and will be dealt with in a forthcoming paper.[19] Thus, the above estimate of the fraction of the decay strength is only an experimental lower limit.

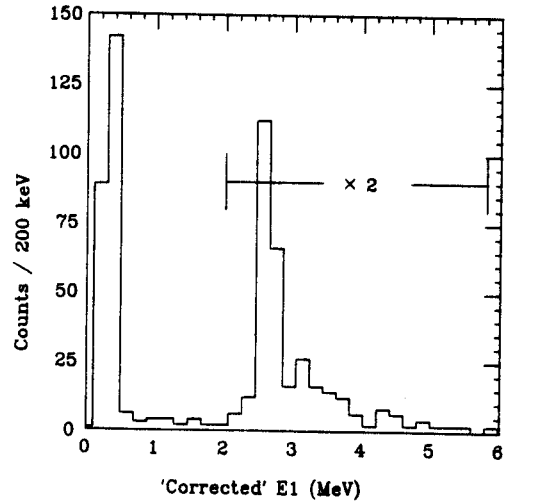

FIG. 6. The decay energy in $E1$ corrected for the β energy loss as described in the text. The data above 2.0 MeV have been multiplied by a factor of 2.

IV. THE BETA DECAY OF THE MIRROR NUCLEUS ^{9}Li

The beta decay branching ratios of ^{9}Li have been investigated by many groups, but the determination of the excitation spectrum in ^{9}Be following the beta decay of ^{9}Li has been complicated by uncertainties in the decay modes of the excited states in ^{9}Be. The particle decay of excited states of ^{9}Be always involves both charged and uncharged particles (2α + neutron). These require very different equipment for detection. Experiments have either measured energy spectra of single alpha particles, alpha-alpha coincidences, or neutron time-of-flight spectra. To extract structure and branching ratio information, the measured spectra were fit with calculated functions based on some model for the particle decay. Previously determined beta-decay branching ratios of ^{9}Li have been summarized in Table I. We have calculated the corresponding B(GT) values from these branching ratios in the same way as for ^{9}C decay (see Sec. III). A value of 0.177 s is used for the half-life of ^{9}Li.[20]

Both Chen *et al.*[8] and Macefield *et al.*[21] have studied the beta-delayed neutron time-of-flight spectrum to determine the beta decay branching ratios of ^{9}Li. Each group clearly identified three peaks in this spectrum.

They agree on the origin of each peak. The peak representing the highest energy neutrons was identified as the neutron decay of the broad $\frac{1}{2}^-$ state in ^{9}Be to the ground state of ^{8}Be. The intermediate energy peak was attributed to the small neutron-decay branch of the $\frac{5}{2}^-$ state to the ground state of ^{8}Be. The lowest energy peak was thought to result from the majority of the decays of the $\frac{5}{2}^-$ through broad intermediate states. This last particle decay branch, which resulted in neutrons with lower energy than the $^8\mathrm{Be}_{\mathrm{g.s.}}+\mathrm{n}$ channel, could be attributed to any one or combination of the following decay channels:

$$^9\mathrm{Be}^*_{5/2^-}\rightarrow\alpha+{}^5\mathrm{He}_{\mathrm{g.s.}},\quad {}^5\mathrm{He}_{\mathrm{g.s.}}\rightarrow\alpha+\mathrm{n}\ ;$$

$$^9\mathrm{Be}^*_{5/2^-}\rightarrow{}^8\mathrm{Be}^*_{2^+}+\mathrm{n},\quad {}^8\mathrm{Be}^*_{2^+}\rightarrow\alpha+\alpha\ ;$$

$$^9\mathrm{Be}^*_{5/2^-}\rightarrow\alpha+\alpha+\mathrm{n}\ \text{directly}\ .$$

Mösner *et al.*[22] have pointed out that the calculated phase-space population of the two alpha particles is quite similar in these three channels. It is possible that some insight could be gained into the structure and breakup dynamics of this level (and other levels in mass 9) through the use of three-body nuclear models. Based on the Born-Oppenheimer model of the H_2^+ molecule, three-body $\alpha+\alpha+\mathrm{n}$ calculations reproduce the level structure in ^{9}Be.[23,24] The beta-decay half-life of ^{6}He and the breakup of ^{6}Li* through sequential decay channels have been predicted with a three-body $\alpha+\mathrm{N}+\mathrm{N}$ calculation based on separable two-body potentials.[25]

In order to determine the absolute branching ratios, Chen *et al.*[8] and Macefield *et al.*[21] assume that all of the beta decay strength of ^{9}Li is to the first $\frac{3}{2}^-$, $\frac{5}{2}^-$, and $\frac{1}{2}^-$ levels. Further, they assume that the highest energy neutron group comes only from the decay of the $\frac{1}{2}^-$ level to the ground state of ^{8}Be, and that the $\frac{1}{2}^-$ level can decay only in this manner. They also assume that the decay of the $\frac{5}{2}^-$ level to the ground state of ^{8}Be is the sole source of counts in the intermediate energy neutron group.

While the authors assume that the two highest energy neutron groups result from the decay of the $\frac{5}{2}^-$ and $\frac{1}{2}^-$ levels to the ground state of ^{8}Be only, they have used different values for the ground state beta decay branch, and different values for the fraction of the neutron decays of the $\frac{5}{2}^-$ state that lead to $^8\mathrm{Be}_{\mathrm{g.s.}}$. Chen *et al.*[8] have determined the ^{9}Li ground state beta decay branching ratio to be 65% from a separate experiment, in which the beta-delayed 2α energy spectrum of ^{9}Li ions implanted in silicon was recorded. Macefield *et al.*[21] used a previously determined value of 75% from the beta-particle energy spectrum from ^{9}Li decay. Since Macefield *et al.* have not determined the ground-state branch themselves, but have relied on other measurements, we have adjusted their values to accommodate the more recent measurements for the ground state branching ratio of 50% by Björnstad *et al.*[26] and Langevin *et al.*[27] It is these adjusted values that are included in Table I.

Langevin *et al.*[27] determined the branching ratios of ^{9}Li to the excited states of ^{9}Be levels listed in Table I from the beta-delayed alpha-particle spectrum only. They allowed more freedom in the choice of the various particle decay branching ratios in their fit. Their beta-decay branching ratio measurements are also included in Table I, and their particle decay branching ratios are included in Table II.

All measurements of the fraction of the decays of the $\frac{5}{2}^-$ state in ^{9}Be that populate the ground state of ^{8}Be are in fairly good agreement, as shown in Table II. In a pure *p*-shell independent particle model this decay is explicitly forbidden, since it must proceed through nucleon decay with $l=2$. The description of this state must therefore include some admixture of higher orbitals. This issue has been addressed by Spencer *et al.*[28] and Henley and Kunz.[29] While Spencer *et al.*[28] only conclude that this fraction must be small, Henley and Kunz[29] predict that this value should lie between 5% and 20%, in agreement with the data. In the mirror system, the proton decay of the $\frac{5}{2}^-$ state in ^{9}B to the ground state of ^{8}Be has not been observed, and Wilkinson *et al.*[7] have set an upper limit on the branching ratio of 1% for this decay. This large asymmetry in the observed branching ratios does not necessarily imply a difference in the nuclear structure aspect of the decay. The data on the decay of the state in ^{9}Be suggest a partial width for the decay to the ground state of ^{8}Be of less than a tenth of a keV. Since the $\frac{5}{2}^-$ level in ^{9}B has a width of roughly 80 keV (more than 100 times larger than the total width in ^{9}Be), it appears that there is more phase space available for decays that do not lead to the ground state of ^{9}Be. Nyman *et al.*[17] have confirmed the narrowness of this level produced in the beta decay of ^{9}Li, and in an elegant experiment, measured the broadening of the delayed neutron peak due to the recoil of the excited ^{9}Be after beta decay.

Both Nyman *et al.*[17] and Langevin *et al.*[27] have found evidence for the population of at least one state near 12 MeV in ^{9}Be following the beta decay of ^{9}Li. In both of these experiments and in the present ^{9}C decay data (see Sec. III), modeling of the particle decay modes plays a strong role in the extraction of a value for the B(GT) for this state. Because of this complication, we defer quantitative comparison between these measurements to a future work.[19]

Langevin *et al.*[27] have fit the high-energy portion of the beta-delayed alpha particle spectrum from the decay of ^{9}Li with a calculation of the statistical three-body breakup of a previously reported level at 11.28 MeV. The choice of this excitation energy was somewhat arbitrary, in that this value was not determined from the data. Instead, it was chosen from a list of known states in ^{9}Be.[6] In their analysis, sequential decay through excited states in ^{8}Be and the ground and excited states of ^{5}Li were ignored, and the strength at lower excitation energies due to the distortion of the line shape by the roughly $(Q_\beta-E_x)^5$ dependence of the statistical rate function was not included.[17,18]

Once a fit was made to the calculated α particle spectrum of Langevin *et al.*,[27] based upon the statistical three-body decay of an undistorted level at 11.28 MeV, which was fitted to the recorded spectrum for the highest energy alpha particles and subtracted from the data, a small residual component remained. They have assigned these remaining counts to the beta decay of ^{9}Li to an additional, previously reported level in ^{9}Be, followed by an unspecified decay mode. They have assigned a branching ratio of 1.5±0.5 % to a level at 7.94 MeV.

Following an analysis of the high-energy beta-delayed alpha particles from ^{9}Li, Nyman *et al.*[17] propose that two levels in ^{9}Be near 12 MeV (those listed in Ajzenberg-Selove[6]) are both populated, and that these levels decay through the ^{5}He$_{g.s.}+\alpha$ channel. The effects of the penetrability of the alpha particle and the beta-decay phase-space factor are explicitly included in the fit. However, channels involving excited states of ^{5}He or ^{8}Be, or direct three-body breakup, are ignored.

V. THE ^{9}Be(p,n)^{9}B REACTION

Recently, there has been much effort to understand to what extent the (p,n) reaction cross section at small angles and high incident proton energies (>100 MeV) is proportional to Gamow-Teller strength. Reviews of this relationship can be found by Goodman *et al.*[30] and Taddeucci *et al.*[31] The Gamow-Teller component of the ^{9}Be(p,n)^{9}B reaction can populate the same levels in ^{9}B as the beta decay of ^{9}C. Since the initial state is now ^{9}Be instead of ^{9}C, and there is no $\beta^+\nu$ phase-space weighting, the observed intensities will be very different than for the case of ^{9}C decay.

Fazely *et al.*[32] and Pugh[33] report cross sections for the ^{9}Be(p,n)^{9}B reaction, and Pugh describes a detailed analysis of the data. Cross sections for those levels which peak at 0° are listed in Table III, and the reported parameters which describe the broad $\frac{1}{2}^-$ level are included in Table II. While this work represents the clearest indication of the broad $\frac{1}{2}^-$ level in ^{9}B besides the present ^{9}C decay data, there still remains a large uncertainty in the nature of this level. Fazely *et al.*[32] show a fit to the neutron spectrum at a small angle using a level at 2.6 MeV with a width of 1.65 MeV. However, the more complete analysis of the data by Pugh[33] indicates a larger width of about 3 MeV for this 2.6 MeV state. The increase may be related to the introduction of a narrow $\frac{1}{2}^+$ level at 2.71 MeV in the fit. It is not clear if more levels are contributing to the spectrum. Since beta decay involves only Gamow-Teller transitions, it populates fewer states. Therefore, widths extracted from these experiments are likely to be more reliable than from the ^{9}Be(p,n)^{9}B reaction.

We have estimated B(GT) values from the ^{9}Be(p,n)^{9}B reaction cross sections, and include the results in Table III. These estimates are based on three simple assumptions: (1) the cross section at 0° is directly proportional to B(GT) (except between analog states where there is an additional Fermi component), (2) the B(GT) value for the ground-state to ground-state transition is 1.00 (a value close to the four theoretical values—see the following section), and (3) 15% of the cross section of the ground-state to ground-state analog transition is due to the Fermi component [based on the distorted wave impulse approximation (DWIA) calculations presented in Ref. 33]. We have chosen the ground-state transition B(GT) as the best reference for normalization. These assumptions give a proportionality constant such that for all nonanalog transitions,

$$B(\mathrm{GT})=0.121\sigma(0^\circ)\,, \tag{5}$$

where σ is in units of mb/sr. This value is in agreement with the more thorough treatment of this relationship by Goodman *et al.*[30] and Taddeucci *et al.*[31]

VI. SHELL MODEL CALCULATIONS

We have calculated the level schemes of the $A=9$ system within the full p-shell model space using the shell-

TABLE III. Excitation energies, widths, and cross sections of those levels reported by Pugh (Ref. 33) whose cross section peaks at 0° in the ^{9}Be(p,n)^{9}B reaction. The B(GT) values are from Eq. (5).

E_x (MeV)	FWHM (MeV)	σ at 0.0° (mb/sr)	σ at 3.4° (mb/sr)	Deduced B(GT)
0.00	a	9.52 ±0.04	7.56 ±0.06	(1.000)[b]
2.36	a	2.09 ±0.04	1.68 ±0.06	0.253
2.71±0.1	0.71±0.1	2.83 ±0.36	2.10 ±0.34	(0.342)[c]
2.75±0.3	3.13±0.2	9.73 ±0.29	8.24 ±0.26	1.177
4.3 ±0.2	1.6 ±0.2	2.41 ±0.06	2.15 ±0.06	0.292
12.23±0.1	0.5 ±0.1	0.230±0.014	0.188±0.017	0.028
13.96±0.1	d	0.066±0.002	0.049±0.005	0.008
14.60±0.1	0.6 ±0.1	0.213±0.025	0.173±0.040	0.026

[a]The experimental widths of these peaks are used to define the experimental resolution (≈0.4 MeV FWHM).
[b]This value was fixed in order to find the proportionality constant in Eq. (5).
[c]The identity of this state is uncertain, but if it represents strength to a level separate from the broad $\frac{1}{2}^-$ at 2.75, it is not a $J^\pi=\frac{1}{2}^-$, $\frac{3}{2}^-$, or $\frac{5}{2}^-$ level, according to shell model predictions. This being the case, it would not be populated through the Gamow-Teller channel as discussed in the text, and thus a value for B(GT) would not be appropriate.
[d]The intrinsic width of the state could not be determined beyond the conclusion that it is small compared to the experimental resolution.

TABLE IV. Shell model predictions for the $A=9$ system. The beta-decay B(GT) values are for beta decay of ^{9}C or ^{9}Li, to the J^π state predicted to lie at E_x MeV in ^{9}B or ^{9}Be. All values in square brackets refer to powers of ten (i.e., $8.0[E^*-9]=8.0\times10^{-9}$). The spectroscopic factors for the allowed particle decay modes for the pure p-shell model are listed, and the resulting width (keV) given in parentheses to the right of the corresponding spectroscopic factor. The widths are calculated from Eq. (6) in the text. Predictions for four interactions are given in the following order: Cohen and Kurath (6–16) 2BME (Ref. 35), Millener (Ref. 36), Kumar (Ref. 37), and Cohen and Kurath (8–16) POT (Ref. 35).

J^π	E_x (MeV)	β-decay B(GT)	^{9}Be(p,n)^{9}B B(GT)	^{8}Be$_{0^+}$ + p $l=1$	^{8}Be$^*_{2^+}$ + p $l=1$	^{5}Li$_{3/2^-}+\alpha$ $l=0$	^{5}Li$_{3/2^-}+\alpha$ $l=2$	^{5}Li$^*_{1/2^-}+\alpha$ $l=0$	^{5}Li$^*_{1/2^-}+\alpha$ $l=2$	Total width (keV)
					Group (a)					
$\frac{3}{2}^-$	0.00	0.035	1.042	0.58 (2.1)	0.73	0.57	0.56		0.062	2.1
	0.00	0.046	0.994	0.57 (2.1)	0.75	0.55	0.58		0.048	2.1
	0.00	0.014	0.917	0.56 (2.0)	0.75	0.55	0.60		0.042	2.0
	0.00	0.086	0.972	0.57 (2.1)	0.78	0.55	0.56		0.054	2.1
$\frac{5}{2}^-$	2.64	0.030	0.233		1.15		0.98		0.14	
	3.03	0.028	0.285		1.13		0.99		0.13	
	2.43	0.066	0.234		1.12		0.95		0.10	
	2.95	0.039	0.291		1.16		0.98		0.19	
$\frac{1}{2}^-$	3.02	0.016	1.056	0.72 (4400)	0.46		0.57	0.65		4400
	2.75	0.020	1.052	0.72 (4400)	0.47		0.57	0.65		4400
	3.25	0.010	1.049	0.75 (4600)	0.42		0.55	0.63		4600
	1.79	0.080	1.028	0.77 (4700)	0.41		0.54	0.61		4700
					Group (b)					
$\frac{3}{2}^-$	5.09	0.005	0.391	0.049 (530)	1.15 (5000)	0.069 (360)	0.31 (780)		0.81	6700
	4.87	0.069	0.470	0.064 (690)	1.13 (4900)	0.092 (490)	0.26 (660)		0.84	6700
	5.49	0.014	0.488	0.053 (570)	1.13 (4900)	0.077 (410)	0.27 (680)		0.78	6600
	4.66	0.081	0.484	0.041 (440)	1.14 (5000)	0.082 (430)	0.26 (660)		0.79	6500
$\frac{5}{2}^-$	7.48	0.140	0.011		0.40 (3900)		0.0087 (49)		0.32	3900
	7.66	0.004	0.021		0.42 (4100)		0.0028 (16)		0.35	4100
	6.91	0.010	0.038		0.49 (4800)		0.0083 (47)		0.36	4800
	7.39	0.032	0.005		0.38 (3700)		0.0007 (4)		0.28	3700
					Group (c)					
$\frac{3}{2}^-$	9.93	1.88	0.062	0.0018 (38)	0.0013 (23)	0.0041 (49)	0.010 (100)		0.0003 (0.8)	210
	9.35	1.42	0.016	8.0[E-9] (0)	0.016 (280)	0.0007 (8)	0.028 (280)		0.018 (46)	610
	9.98	1.45	0.022	0.0016 (34)	0.0011 (19)	0.0029 (35)	0.0075 (75)		0.0003 (0.8)	160
	10.04	1.78	0.080	1.7[E-7] (0)	0.015 (260)	0.0013 (16),	0.039 (390)		0.022 (56)	730
$\frac{1}{2}^-$	11.50	0.10	0.049	0.0076 (160)	0.0073 (130)		0.0051 (51)	0.0058 (31)		370
	9.70	0.38	0.022	0.0007 (15)	0.0036 (63)		0.0020 (20)	0.0023 (12)		110
	8.10	0.45	0.025	0.0056 (120)	1.4[E-4] (2)		0.0065 (65)	0.0074 (39)		230
	11.02	0.25	0.038	0.0010 (21)	0.0052 (91)		0.0014 (14)	0.0016 (8)		130

TABLE IV. (*Continued*).

J^π	E_x (MeV)	β-decay B(GT)	^{9}Be(p,n)^{9}B B(GT)	^{8}Be$_{0^+}$ + p $l=1$	^{8}Be$^*_{2^+}$ + p $l=1$	^{5}Li$_{3/2^-}$ + α $l=0$	^{5}Li$_{3/2^-}$ + α $l=2$	^{5}Li$^*_{1/2^-}$ + α $l=0$	^{5}Li$^*_{1/2^-}$ + α $l=2$	Total width (keV)
$\frac{5}{2}^-$	11.61	2.32	0.024		0.028 (490)		0.0079 (79)		0.029 (74)	640
	9.80	2.48	0.000		0.0037 (65)		0.010 (100)		0.0048 (12)	180
	10.13	1.89	0.046		0.019 (330)		0.029 (290)		0.020 (51)	670
	10.87	2.66	0.000		0.0058 (100)		0.0038 (38)		0.0089 (23)	160
$\frac{1}{2}^-$	12.18	1.63	0.000	0.0005 (11)	0.0004 (7)		0.0032 (32)	0.0037 (20)		70
	13.03[a]	1.00	0.002	0.0014 (30)	0.006 (110)		0.011 (110)	0.012 (64)		310
	13.34[b]	1.19	0.019	3.3[E-5] (0.7)	0.0030 (52)		4.0[E-5] (0.4)	5.0[E-5] (0.3)		53
	12.04	1.42	0.017	0.0039 (82)	0.019 (330)		0.024 (240)	0.038 (200)		850

[a]Below this state the Millener (Ref. 36) interaction also predicts states at 11.98 MeV ($\frac{5}{2}^-$) and 12.40 MeV ($\frac{3}{2}^-$).

[b]Below this state the Kumar (Ref. 37) interaction also predicts states at 11.36 MeV ($\frac{5}{2}^-$), 12.04 MeV ($\frac{3}{2}^-$), and 12.24 MeV ($\frac{3}{2}^-$).

model code OXBASH.[34] Four interactions were considered, two of the original interactions of Cohen and Kurath,[35] i.e., the (6–16) 2BME and the (8–16) POT interactions, as well as the more recent interactions of Millener[36] and Kumar.[37] All of these are based upon a least-squares fit of the interaction parameters to some subset of the *p*-shell binding energies and energy levels.

Predicted excitation energies of $\frac{1}{2}^-$, $\frac{3}{2}^-$, and $\frac{5}{2}^-$ levels in ^{9}B and ^{9}Be, and B(GT) values for the population of these levels from the beta decay of ^{9}C and ^{9}Li, and from the ^{9}Be(p,n)^{9}B reaction are summarized in Tables IV and III, respectively. These theoretical B(GT) values are defined in Ref. 38 and include the $(g_A/g_V)^2$ factor. They have also been multiplied by a factor of 0.6 to take into account the empirical quenching observed for this operator.[38] Since binding energy and isospin mixing corrections have not been considered, the predicted excitation energies and beta-decay B(GT) values apply to both members of the mirror system.

Table IV contains calculated spectroscopic factors for all available two-body decay channels using each of the four *p*-shell interactions. Channels for which there can be no strength from a pure *p*-shell model have blank entries. The α-particle spectroscopic amplitudes were calculated using an SU(3) cluster for the α particle as described in Ref. 39, and were cross-checked against similar calculations provided by Millener.[40] We have calculated the partial widths based on the decay of these levels in ^{9}B. The resulting widths in keV are listed in parentheses to the right of the corresponding spectroscopic factors in Table IV. The widths are given by[41–44]

$$\Gamma_l = 2\theta_l^2 \gamma^2 P_l (E_x - Q) , \tag{6}$$

where θ_l^2 is the spectroscopic factor, P_l is the penetrability, E_x is the excitation energy of the ^{9}B nucleus, and γ^2 is the Wigner single particle reduced width given by

$$\gamma^2 = \frac{3}{2} \frac{(\hbar c)^2}{\mu R_0^2} . \tag{7}$$

Here μ is the reduced mass. The penetrabilities were calculated from the Coulomb wave functions using the method of Steed as described by Barnett.[45]

The channel radius R_0 was set to 4.0 fm for the ^{8}Be + p channels, and 4.5 fm for the ^{5}Li + α channels. The penetrabilities for the first three levels are calculated using the excitation energies of 0.00, 2.36, and 2.9 MeV, for the $\frac{3}{2}^-$, $\frac{5}{2}^-$, and $\frac{1}{2}^-$, levels, respectively. For the next two levels, the theoretical excitation energies for each prediction are used. All of the penetrabilities for the last four levels predicted to lie above 8 MeV are calculated, assuming the state is at an excitation energy of 12.1 MeV. Where calculated, the penetrabilities for the ^{8}Be$_{g.s.}$ + p, ^{8}Be$^*_{2^+}$ + p, ^{5}Li$_{g.s.}$ + α, and ^{5}Li$^*_{1/2^-}$ + α channels are calculated, assuming $Q = -0.19$, 2.7, 1.69, and 8.69 MeV, respectively. The last three values represent arbitrary effective centroids for the broad intermediate states in ^{8}Be and ^{5}Li.

For states above the Coulomb plus centrifugal barrier, which lies a few MeV above threshold for p and α emission from light nuclei, the penetrability represents

roughly the available phase space (e.g., $k^2dk \approx k\,dE \approx \sqrt{E}\,dE$, where k and E are the center-of-mass momentum and energy for the decay). Thus for a given spectroscopic factor, the widths of the states are only slowly varying functions of the actual binding energy of the state. Therefore, once above the Coulomb barrier, the widths for the mirror decays to ^{8}Be + p or n should be similar to each other, as should those for $\alpha + {}^5$Li or ^{5}He. Given the uncertainty in the calculated spectroscopic factors, it is not important at the moment to include the small differences between these unbound levels in mirror nuclei. Thus, the widths given for states above 4 MeV in ^{9}B can be treated as estimates of the widths of the same levels in ^{9}Be.

The major uncertainties in these width calculations are related to the approximations used in Eq. (6), and to the fact that the small spectroscopic factors will be sensitive to admixtures from configurations outside the p-shell model space. We believe that the former is responsible for the "factor of 4" discrepancy discussed in the following section. Equation (6) could be replaced with more complete models;[46] however, this treatment would be beyond the scope of the present work.

VII. DISCUSSION

The states in Table IV can be divided into three groups: (a) the lowest three states below 4 MeV which have small beta-decay B(GT) values but which dominate in the beta decay of ^{9}C and ^{9}Li because of the large Q value for the decay; (b) the next two states lying between 4 and 8 MeV which also have small beta-decay B(GT) values; and (c) the next few states above 8 MeV which have large beta-decay B(GT) values. We will use this division to organize our discussion.

A. Group (a): States below 4 MeV

The states in group (a) have small B(GT) values for beta decay; that is, small compared to the sum-rule value of $0.6(g_A/g_V)^2 3(Z-N)=8.5$. For these states, the original (6–16) 2BME interaction of Cohen and Kurath[35] appears to give the best overall agreement with experiment for both energy levels and beta decay B(GT) values. Indeed, these B(GT) values are in remarkably good agreement given the smallness of the values (see Table I). The states in group (a) have large spectroscopic factors for the allowed nucleon decays to the ground state and 2^+ states of ^{8}Be, and allowed α decays to the ground state of ^{5}Li (see Table IV). The calculated B(GT) values for the ^{9}Be(p,n)^{9}B reaction of Table IV also agree well with the experimental values of Table III.

While the two most recent measurements of the branching ratio for the ^{9}Li$\rightarrow{}^9$Be ground state beta decay yield B(GT) which agree favorably with the value for ^{9}C decay (see Table I), agreement between measurements for decays to the other two low-lying states is not as good. In the case of the $\frac{1}{2}^-$ level, the values for the ^{9}Li decay span a range of a factor of 5, with our value from ^{9}C decay close to the middle. In the case of the branch to the $\frac{5}{2}^-$ level, the three B(GT) values for ^{9}Li decay are all very close, while our value for the decay of ^{9}C is lower than these values by more than a factor of 2. If isospin is conserved, the wave functions for mirror levels, and thus the B(GT) values for mirror beta decays, should be identical. Deviations from mirror symmetry have been extensively investigated, and examples of asymmetry in beta decay have been identified.[47,48]

We define an asymmetry parameter,

$$\Delta=\sqrt{B(\mathrm{GT})_-}-\sqrt{B(\mathrm{GT})_+}\,, \tag{8}$$

as a way to express the absolute difference in the beta decay matrix elements. Previously the two largest absolute asymmetries observed in the p shell were found in the decays of ^{12}B and ^{12}N to the ground state of ^{12}C ($\Delta=0.043$),[49] and the decays of ^{13}B and ^{13}O in the ground states of ^{13}C and ^{13}N, respectively ($\Delta=0.076$).[50–52] As given, the data in Table I suggest a value $\Delta=0.09\pm0.03$ for the decay to the $\frac{5}{2}^-$ level. Towner[53] has demonstrated that most of the measured asymmetries can be fairly well accounted for by small differences in the radial wave functions of the mirror states. This difference is due to the Coulomb interaction, which introduces an asymmetry in the binding energies of the mirror nuclei. However, for the decay to the $\frac{5}{2}^-$ level in mass 9, Towner predicts a value for Δ of only 0.008, an order of magnitude smaller than observed.

Inconsistencies between the various measurements of B(GT) values for ^{9}Li beta decay shown in Table I and particle decay branching ratios in Table II cast doubt on the branching ratio measurements for the decay of ^{9}Li to the $\frac{5}{2}^-$ level in ^{9}Be. Each relies on some particular particle decay characteristic of the $\frac{5}{2}^-$ level that is not yet determined with suitable reliability. As an example, let us develop a possible explanation for the observed asymmetry between the B(GT) for the population of the $\frac{5}{2}^-$ level from ^{9}Li and ^{9}C decay, based on a misinterpretation of the beta-delayed particle spectra for ^{9}Li.

The shell model calculations shown in Table IV indicate that the $\frac{1}{2}^-$ level in ^{9}Be and ^{9}B has a large spectroscopic factor for the decay into both the ground state and first excited state of ^{8}Be. If the high-energy tail of this broad level neutron decays through the low energy tail of ^{8}Be$^*_{2+}$, these events could contaminate the intermediate energy peak in the delayed neutron spectrum discussed in Sec. IV, and as a result cause the branching ratio to the the $\frac{5}{2}^-$ level to be overestimated.

In order to be more quantitative, let us assume that the beta decay branching ratios of ^{9}Li to the $\frac{5}{2}^-$ and $\frac{1}{2}^-$ levels of ^{9}Be are both 15%. We will use 7% as the fraction of the decays of the narrow $\frac{5}{2}^-$ level to the ground state of ^{8}Be (consistent with previous experiments; see Table II). If 5% of the decays of the $\frac{1}{2}^-$ state populate the first 2^+ state of ^{8}Be instead of the ground state, and these lower energy neutrons are mistaken as neutrons from the decay of the $\frac{5}{2}^-$ level to the ground state of ^{8}Be, the inferred branching ratio to the $\frac{1}{2}^-$ level will be reduced slightly to about 14%. However, since the strength of the intermediate energy neutron group must

be multiplied by $1/0.07=14.3$ in order to obtain the branching ratio to the $\frac{5}{2}^-$ level, the inferred branching ratio to this state will be

$$14.3\times[(15\%\times0.07)+(15\%\times0.05)]=26\% \quad (9)$$

instead of 15%. Here, the first term represents the real branch to the $\frac{5}{2}^-$ level, and the second term represents the branch to the $\frac{1}{2}^-$ level that would be mistaken as additional population of the $\frac{5}{2}^-$ level.

While only an instructive example, this scenario is consistent with the known data. Adloff *et al.*[54] have given only an upper limit of 28% to the fraction of the decays of the $\frac{1}{2}^-$ level that do not decay to the ground state of ^{8}Be. (Langevin *et al.*[27] suggest a value for this fraction of 70%. However, this value is based in part on the branching ratio to the $\frac{1}{2}^-$ level of Chen *et al.*,[8] itself a factor of 5 lower than that of Macefield *et al.*[21]) The results listed in Table IV indicate a large spectroscopic factor for the decay of the $\frac{1}{2}^-$ level to the first excited state of ^{8}Be, and so one must expect some fraction of the decays of the high-energy part of the broad $\frac{1}{2}^-$ level to decay through this channel, despite the Coulomb plus $l=1$ centrifugal barrier.

A possible candidate for a fourth level belonging to group (a) has been reported by Esterl *et al.*[4] They observed a delayed proton group from the decay of ^{9}C that would correspond to a state in ^{9}B at 3.25±0.25 MeV with a width of 0.2±0.1 MeV, decaying by proton emission to the ground state of ^{8}Be. The narrow width of this peak precludes the assignment to the first $\frac{1}{2}^-$ level discussed above. Based on the nonobservation of the population of this narrow state in our data, we put an upper limit on the value of the ^{9}C beta decay B(GT) value of 0.004 [or a $\log(ft)\geqq6.2$]. It is difficult to tell whether or not the peak of Esterl *et al.* is consistent with this strength. The shell model calculations (see Table IV) do not leave room for any narrow $\frac{1}{2}^-$, $\frac{3}{2}^-$, or $\frac{5}{2}^-$ levels between the first $\frac{5}{2}^-$ level at 2.36 and the levels of group (c) predicted to lie above 9 MeV. This peak cannot be attributed to the nucleon decay of a level near 6 MeV to the first 2^+ state of ^{8}Be, since this state in ^{8}Be has a width of about 1.5 MeV, and the experimental peak has a width of only a fraction of an MeV. Thus, if this peak represents a state in ^{9}B, it most likely represents a first-forbidden transition to a level near 3.25 MeV with a width of 0.2±0.1 MeV.

B. Group (b): States between 4 and 8 MeV

We cannot identify any of the states in group (b) in the present experiment. This again is consistent with the shell-model calculations, which predict a small B(GT) value for the population of these states from beta decay. Both states in this group have strong spectroscopic factors for decay through the ^{8}Be$^*_{2+}$ + nucleon channel. While the $\frac{5}{2}^-$ level is predicted to decay nearly exclusively through this channel, the $\frac{3}{2}^-$ level is predicted to have some strength to the ^{8}Be$_{g.s.}$ + nucleon and mass $5+\alpha$ channels.

Pugh[33] has identified a state in ^{9}B at 4.3±0.2 MeV with a width of 1.6±0.2 MeV, populated in the ^{9}Be(p,n)^{9}B reaction. The cross section for this level peaks at 0°, and implies a value for B(GT) of about 0.29 (see Table III and Sec. V). This represents an excellent match for the $\frac{3}{2}^-$ state of group (b) predicted to lie near 5 MeV. The predicted widths of the $\frac{3}{2}^-$ and $\frac{1}{2}^-$ levels of group (a) are both about a factor of 4 greater than observed in ^{9}B (compare values for these widths given in Tables II and IV). If the predicted width of the $\frac{3}{2}^-$ level of group (b) is similarly reduced by a factor of 4, the agreement between the calculated position and width of this level and the level described by Pugh[33] is nearly perfect. Esterl *et al.*[4] have identified a peak in the delayed proton spectrum that could represent the proton decay of a level in ^{9}B at 4.0±0.3 MeV with a width of 1.0±0.2 MeV to the ground state of ^{8}Be. From the calculated partial widths listed in Table IV, we estimate that the $\frac{3}{2}^-$ level of group (b) will decay through this channel roughly 10% of the time. It is then reasonable to suspect that beta decay to this $\frac{3}{2}^-$ level followed by proton decay to the ground state of ^{8}Be may be the source of the proton peak described by Esterl *et al.*[4]

The population of this $\frac{3}{2}^-$ level from the decay of ^{9}C would be difficult to observe in our present data, due to its large width. However, if present, it would manifest itself as a broad peak to the higher energy side of the peak due to the $\frac{1}{2}^-$ level in Fig. 5. The lack of observation of such a structure in the present data sets an upper limit for the B(GT) of 0.007 [$\log(ft)=5.9$] for the beta decay strength to the state reported by Pugh.[33] This is consistent with the small predicted B(GT) values for the $\frac{3}{2}^-$ state of group (b) listed in Table IV.

The $\frac{5}{2}^-$ level near 7 MeV is predicted to decay almost exclusively through the ^{8}Be$^*_{2+}$ + nucleon. If we assume that the width is overpredicted by the same factor of 4 as discussed above, the width of this state is expected to be near 1 MeV. This level has small B(GT) values for population through both beta decay and the ^{9}Be(p,n) reaction. There is no evidence for such a level in the analysis of Pugh.[33] The same delayed proton peak of Esterl *et al.*[4] that we have associated with the $\frac{3}{2}^-$ level of group (b) (see above) cannot be attributed to the decay of the $\frac{5}{2}^-$ level to the first 2^+ state of ^{8}Be. This level is expected to have a width of at least 1 MeV, and the 2^+ state in ^{8}Be has a width of about 1.5 MeV. These two factors suggest that a delayed proton peak from this level should have a width in the lab of 2 MeV or more, in contrast to the observed width of 1.0 MeV observed by Esterl *et al.*[4]

Langevin *et al.*[27] observe a beta-decay branch of ^{9}Li to a broad level near 8 MeV. They have associated this strength with a reported level at 7.94 MeV in ^{9}Be (see Sec. IV). While this assignment is somewhat uncertain, their measured branching ratio of 1.5±0.5% implies a B(GT) of 0.06±0.02 [$\log(ft)\approx5.0\pm0.1$] at this energy. This value is consistent with the predicted B(GT) for the $\frac{5}{2}^-$ level of group (b).

C. Group (c): States above 8 MeV

All of the states in group (c) have large B(GT) values for population by beta decay, and small B(GT) for the ^{9}Be(p,n) reaction. They all have very small spectroscopic factors for all of the decay channels considered in Table IV. Because of their small predicted widths, they are all candidates for the sharp state we observe near 12 MeV. For all of the interactions the predicted excitation energies are too low by 2–3 MeV. However, this is not an uncommon problem with shell model calculations. We note that all of the calculations also underpredict the excitation energy of the lowest $\frac{3}{2}^-$ $T=\frac{3}{2}$ state, which lies experimentally at 14.7 MeV, by amounts of 1.39, 2.26, 2.41, and 1.05 MeV, for the (6–16) 2BME,[35] Millener,[36] Kumar,[37] and (8–16) POT (Ref. 35) interactions, respectively (this is the same ordering as in Tables I and IV).

Pugh[33] has reported three states that are candidates for these four predicted levels. All of the predicted and experimental B(GT) values for the ^{9}Be(p,n)^{9}B reaction are so small that their uncertainties allow for no unambiguous assignments of any one of the predicted levels to any one measured level.

Hardy *et al.*[3] and Esterl *et al.*[4] report peaks in the delayed proton spectrum near 9 MeV and 12 MeV in the center of mass. There are at least three different explanations for these peaks; that the decay of ^{9}C populates

(1) two levels in ^{9}B, the first level near 9 MeV with a width of 1.5 MeV, and the second is near 12 MeV with a width of 0.5 MeV—both levels at least occasionally proton decay to the ground state of ^{8}Be;

(2) two levels in ^{9}B near 12 MeV populated in the ratio of 1.5:1, the first level decaying to the 2^+ excited state of ^{8}Be, and the second level to the ground state;

(3) a single level in ^{9}B near 12 MeV, which proton decays to the broad 2^+ level in ^{8}Be at 3 MeV and to the ground state in the ratio of 1.5:1.

In all cases, the large continuum rising to the lower energy side of the two peaks can still be explained as the dominant decay of one (or both) level(s) through the $^5\mathrm{Li}_{g.s.}+\alpha$ channel, generating protons with energies lower than those from the ^{8}Be channels. This is the only decay mode observed by Nyman *et al.*[17] of one or more levels near 12 MeV in ^{9}Be populated from the beta decay of ^{9}Li.

In the present experiment, we observe only a narrow peak near 12 MeV and do not observe the broad 9 MeV peak. We therefore can rule out (1). In order for (2) to be consistent with the single narrow peak in our data, the two levels should have nearly identical excitation energies or very different beta-decay branching ratios. Explanation (3) seems the simplest way to explain the two sets of data, and we will adopt this.

In Sec. III we determined the single standard deviation lower limit of the branching ratio to the narrow level at 12.1±0.6 MeV as 1.8%. This value represents a value for the B(GT) of 0.6. The largest contribution to the uncertainty (and thus contributing to the smallness of the lower limit) results from the uncertainty in the measured excitation energy of the state in our experiment. If the state can be assigned the same excitation as that of Esterl *et al.*,[4] at 12.11±0.10 MeV, then the one standard deviation lower limit for the B(GT) becomes 1.1. Corrections for efficiency will further increase these lower limits for the B(GT).

Of the predicted levels in group (c), only the $\frac{3}{2}^-$, $\frac{5}{2}^-$, and second $\frac{1}{2}^-$ levels have predicted beta decay B(GT) values large enough to be consistent with the measured B(GT). If we assume that there is only one level near 12 MeV that is strongly populated by beta decay, and that it is responsible for both peaks in the delayed proton data, then we must rule out the predicted $\frac{5}{2}^-$ level, since it should have no significant branch to the ground state of ^{8}Be. This leaves us with only the $\frac{3}{2}^-$ and second $\frac{1}{2}^-$ levels of group (c) as candidates for the level populated by beta decay. If the underprediction of the excitation energies of these levels (as discussed in the beginning of this section) is taken into account, the agreement between the $\frac{1}{2}^-$ and the observed level at 12 MeV is complete, and the second $\frac{1}{2}^-$ level is too high by 2–3 MeV. While we cannot associate with certainty the 12.2±0.1 MeV level observed by Pugh[33] with the level observed in beta decay, the observed strength in the ^{9}Be(p,n)^{9}B reaction is consistent with the predicted value for the $\frac{3}{2}^-$ level.

The level populated strongly near 12 MeV is clearly a part of the giant Gamow-Teller resonance. If indeed it turns out to be a $\frac{1}{2}^-$ level, this level might be described as the "antianalog" state. This term describes the level (or group of nearby levels) which have structure similar to that of the analog state itself, but have the isospin of the ground state. This strong transition can be compared to the strong beta decay of ^{12}N and ^{12}B to the 12.7 MeV $J^\pi=1^+$ $T=0$ level in ^{12}C, with a B(GT) of about 2.0 [$\log(ft)\approx 3.5$].[55,56] This level lies 2.4 MeV below the $J^\pi=1^+$, $T=1$ analog state in ^{12}C. Assuming that our narrow state has a $J^\pi=\frac{3}{2}^-$, $T=\frac{1}{2}$ assignment, and that it is the level seen by Esterl *et al.*[4] at 12.1 MeV, the separation between this level and the analog $J^\pi=\frac{3}{2}^-$, $T=\frac{3}{2}$ level at 14.7 MeV in ^{9}B is 2.6 MeV. This is nearly the same separation as that between the $T=0$ and $T=1$ $J^\pi=1^+$ levels in ^{12}C.[6]

VIII. SUMMARY

We have observed the population of the ground state and two low lying excited states in ^{9}B from the beta decay of ^{9}C, by implanting the radioactive ions in solid state detectors. A technique was developed to remove the beta energy loss contamination of the spectrum, allowing for the use of much thicker detectors than has been previously possible. The branching ratios to these levels have been determined, and the results compared to several measurements of the decay of the mirror nucleus ^{9}Li. We have also compared the beta decay data for both nuclei and the ^{9}Be(p,n)^{9}B cross sections to shell model predictions. The population of a state near 12 MeV from the decay of ^{9}C is confirmed, while a previ-

ously reported peak at 9 MeV in the delayed proton data is not seen. This supports the previous suggestion that the 9 MeV peak was generated by a state at 12 MeV decaying through the first excited state of ^{8}Be.[4]

Overall, the agreement between the present data, the mirror decay of ^{9}Li, the ^{9}Be(p,n)^{9}B reaction, and shell model calculations is quite good. The most striking disagreement is between the mirror B(GT) values for ^{9}C and ^{9}Li decay to the lowest $\frac{1}{2}^-$ level in ^{9}B and ^{9}Be, respectively. The three measurements for the ^{9}Li decay are all very close to each other, yet more than a factor of 2 greater than the value we observe for ^{9}C decay. We have suggested a possible systematic misinterpretation of the ^{9}Li decay data that might explain this observed asymmetry. The absolute difference between the observed matrix elements is ten times greater than predicted by Towner,[53] who is able to account for the asymmetries observed in other systems, and may be the largest observed to date.

There are many ambiguities that must be resolved before the level assignment and B(GT) strengths can be understood in mass 9. We feel that a new measurement of the beta decay of ^{9}Li is called for. The beta-delayed neutron spectrum of ^{9}Li should be remeasured with the decay of the ^{9}Li nuclei occurring within a silicon detector or between a pair of silicon detectors. This would provide a highly efficient coincident detection of the delayed 2α energy. The complementary pair of excitation energy spectra in ^{9}Be and ^{9}B from the decay of ^{9}Li and ^{9}C will allow for a more complete characterization of the beta decay strengths in this system.

The reactions ^{6}Li(^{6}Li,^{3}H) and ^{6}Li(^{6}Li,^{3}He) may also be used to study the region near 12 MeV of excitation in ^{9}B and ^{9}Be. These reactions have small calculated spectroscopic factors for the levels at low excitation, and large spectroscopic factors for states between 8 and 15 MeV of excitation in these nuclei.

ACKNOWLEDGMENTS

We would like to thank J. C. Hardy, D. J. Millener, and G. Bertsch for helpful comments on various subjects discussed in this paper. This work was supported in part by National Science Foundation Grant PHY 86-11210.

[1]Joseph Cerny and J. C. Hardy, Annu. Rev. Nucl. Sci. **27**, 333 (1977).
[2]M. A. C. Hotchkis, J. E. Reiff, D. J. Vieira, F. Blönnigen, T. F. Lang, D. M. Moltz, X. Xu, and Joseph Cerny, Phys. Rev. C **35**, 315 (1987).
[3]J. C. Hardy, R. I. Verrall, R. Barton, and R. E. Bell, Phys. Rev. Lett. **14**, 376 (1965).
[4]John E. Esterl, David Allred, J. C. Hardy, R. G. Sextro, and Joseph Cerny, Phys. Rev. C **6**, 373 (1972).
[5]J. C. Hardy, private communication.
[6]F. Ajzenberg-Selove, Nucl. Phys. **A413**, 1 (1984).
[7]D. H. Wilkinson, J. T. Sample, and D. E. Alburger, Phys. Rev. **146**, 662 (1970).
[8]Y. S. Chen, T. A. Tombrello, and R. W. Kavanagh, Nucl. Phys. **146**, 136 (1970).
[9]C. A. Barnes and Davis B. Nichols, Nucl. Phys. **A217**, 125 (1973).
[10]Robert A. Langley, Nucl. Instrum. Methods **113**, 109 (1973).
[11]K. Nichols and V. A. J. Van Lint, *Solid State Physics* (Advances in Research and Applications) (Academic, New York, 1966), Vol. 18, pp. 1–54.
[12]J. A. Nolen, Jr., L. H. Harwood, M. S. Curtin, E. Ormand, and S. Bricker, *Instrumentation for Heavy Ion Nuclear Research*, Proceedings of the International Conference on Instrumentation for Heavy Ion Research, Oak Ridge National Laboratory, Tennessee (Harwood Academic, New York, 1984).
[13]M. S. Curtin, L. H. Harwood, J. A. Nolen, B. Sherrill, Z. Q. Xie, and B. A. Brown, Phys. Rev. Lett. **56**, 34 (1986).
[14]J. M. Mosher, R. W. Kavanagh, and T. A. Tombrello, Phys. Rev. C **3**, 438 (1971).
[15]E. Teranishi and B. Furubayashi, Phys. Lett. **9**, 157 (1964).
[16]D. H. Wilkinson and B. E. F. Macefield, Nucl. Phys. **A232**, 58 (1974).
[17]G. Nyman, R. E. Azuma, B. Jonson, K.-L. Kratz, P. O. Larsson, S. Mattsson, and W. Ziegert, in Proceedings of the Fourth International Conference on Nuclei Far from Stability, Helsingør, 1981, edited by L. O. Skolen, Vol. I, p. 312.
[18]E. K. Warburton, Phys. Rev. C **33**, 303 (1986).
[19]D. Mikolas (unpublished).
[20]E. Roeckl, P. F. Dittner, C. Détraz, R. Klapisch, C. Thibault, and C. Rigaud, Phys. Rev. C **10**, 1181 (1974).
[21]B. E. F. Macefield, B. Wakefield, and D. H. Wilkinson, Nucl. Phys. **A131**, 250 (1969).
[22]Jürgen Mösner, Günter Schmidt, und Josef Schintlmeister, Nucl. Phys. **64**, 169 (1965).
[23]A. C. Fonseca and P. E. Shanley, Ann. Phys. (N.Y.) **117**, 268 (1979).
[24]A. C. Fonseca, J. Revai, and A. Matveenko, Nucl. Phys. **A326**, 182 (1979); J. Revai and A. V. Matveenko, *ibid.* **A339**, 448 (1980).
[25]W. C. Parke, A. Ghovanlou, C. T. Noguchi, M. Rajan, and D. R. Lehman, Phys. Lett. **74B**, 158 (1978); W. C. Parke and D. R. Lehman, Phys. Rev. C **29**, 2319 (1984); **34**, E1496 (1986).
[26]T. Björnstad, H. Å, Gustafsson, P. G. Hansen, B. Jonson, V. Lindfors, S. Mattsson, A. M. Poskanzer, and H. L. Ravn, Nucl. Phys. **A359**, 1 (1981).
[27]M. Langevin, C. Détraz, D. Guillemaud, F. Naulin, M. Epherre, R. Klapisch, S. K. T. Mark, M. de Saint Simon, C. Thibault, and F. Touchard, Nucl. Phys. **A366**, 449 (1981).
[28]R. R. Spencer, G. C. Phillips, and T. E. Young, Nucl. Phys. **21**, 310 (1960).
[29]E. M. Henley and P. D. Kunz, Phys. Rev. **118**, 248 (1960).
[30]C. D. Goodman, C. A. Goulding, M. B. Greenfield, J. Rapaport, D. E. Bainum, C. C. Foster, W. G. Love, and F. Petrovich, Phys. Rev. Lett. **44**, 1755 (1980).
[31]T. N. Taddeucci, C. A. Goulding, T. A. Carey, R. C. Byrd, C. D. Byrd, C. D. Goodman, C. Gaarde, J. Larsen, D. Horen, J. Rapaport, and E. Sugarbaker, Nucl. Phys. **A469**,

125 (1987), and E. Krofcheck, E. Sugarbaker, A. J. Wagner, J. Rapaport, D. Wang, J. N. Bahcall, R. C. Byrd, C. C. Foster, C. D. Goodman, C. Gaarde, D. J. Horen, T. Carey, and T. N. Taddeucci, Phys. Lett. **B189**, 299 (1987).

[32]A. Fazely, B. Anderson, A. R. Baldwin, A. Kalenda, R. Madey, R. J. McCarthy, P. Tandy, J. Watson, W. Bertozzi, T. N. Buti, J. M. Finn, J. Kelly, M. A. Kovash, B. Pugh, and C. C. Foster, Indiana University Cyclotron Facility Annual Report, 1982, p. 49.

[33]Billy Gene Pugh, Ph.D. thesis, Massachusetts Institute of Technology, 1985 (unpublished).

[34]A. Etchegoyen, W. M. D. Rae, and B. A. Brown, Michigan State University Cyclotron Laboratory Report 524, 1985.

[35]S. Cohen and D. Kurath, Nucl. Phys. **73**, 1 (1965).

[36]D. J. Millener, private communication. This interaction is based on a fit of the two-body matrix elements to 48 levels in the mass region $A = 10-15$.

[37]N. Kumar, Nucl. Phys. **A225**, 221 (1974).

[38]B. A. Brown and B. H. Wildenthal, At. Data Nucl. Data Tables **33**, 347 (1985).

[39]Munetake Ichimura, Akito Arima, E. C. Halbert, and Tokuo Terasawa, Nucl. Phys. **A204**, 225 (1973).

[40]D. J. Millener, private communication.

[41]A. M. Lane and R. G. Thomas, Rev. Mod. Phys. **30**, 257 (1958).

[42]J. B. French, in *Nuclear Spectroscopy*, edited by F. Ajzenberg-Selove (Academic, New York, 1960), p. 890.

[43]M. H. Macfarlane and J. B. French, Rev. Mod. Phys. **32**, 567 (1960).

[44]J. B. Marion and F. C. Young, *Nuclear Reaction Analysis* (North-Holland, Amsterdam, 1968), pp. 84–95 and 147.

[45]A. R. Barnett, Comput. Phys. Commun. **27**, 147 (1982).

[46]R. Sherr and G. Bertsch, Phys. Rev. C **32**, 1809 (1985).

[47]D. H. Wilkinson, Phys. Rev. Lett. **27**, 1018 (1971).

[48]D. H. Wilkinson, Phys. Lett. **48B**, 169 (1974).

[49]D. E. Alburger and A. M. Nathan, Phys. Rev. C **17**, 280 (1978).

[50]K. W. Jones, W. R. Harris, M. T. McEllistrem, and D. E. Alburger, Phys. Rev. **186**, 978 (1969).

[51]D. E. Alburger and D. R. Goosman, Phys. Rev. C **10**, 935 (1974).

[52]J. E. Esterl, J. C. Hardy, R. G. Sextro, and J. Cerny, Phys. Lett. **33B**, 287 (1970).

[53]I. S. Towner, Nucl. Phys. **A216**, 589 (1973).

[54]J. C. Adloff, K. H. Souw, and C. L. Cocke, Phys. Rev. C **3**, 1808 (1971).

[55]D. Schwalm and B. Povh, Nucl. Phys. **89**, 401 (1966).

[56]D. E. Alburger and D. H. Wilkinson, Phys. Rev. **153**, 1061 (1967).

[57]B. M. K. Nefkens, Phys. Rev. Lett. **10**, 243 (1963).

[58]A. H. Wapstra, A. Audi, and K. Bos, December 1983 Atomic Mass Adjustments, Nuclear Data Group, Brookhaven National Laboratory; Nucl. Phys. **A432**, 1 (1985).

[59]D. Bodansky, S. F. Eccles, and I. Halpern, Phys. Rev. **108**, 1019 (1957).

[60]P. R. Christensen and C. L. Cocke, Nucl. Phys. **89**, 656 (1966).

APPENDIX B

APPENDIX B

BETA DELAYED PARTICLE DECAY THRESHOLDS FOR LIGHT NUCLEI

Neutron Rich Nuclei:

6HE => 6LI MAXIMUM EXCITATION ENERGY FROM BETA DECAY 3.51
a + d = 6LI + 1.48 MeV

8HE => 8LI MAXIMUM EXCITATION ENERGY FROM BETA DECAY 10.65
7LI + n = 8LI + 2.03 MeV
a + t + n = 8LI + 4.50
5HE + t = 8LI + 5.39
a + 4H = 8LI + 7.32
6LI + 2n = 8LI + 9.28
6HE + d = 8LI + 9.78

8LI => 8BE MAXIMUM EXCITATION ENERGY FROM BETA DECAY 16.00
2a = 8BE + -0.09 MeV

9LI => 9BE MAXIMUM EXCITATION ENERGY FROM BETA DECAY 13.61
2a + n = 9BE + 1.57 MeV
8BE + n = 9BE + 1.67
5HE + a = 9BE + 2.47

11LI => 11BE MAXIMUM EXCITATION ENERGY FROM BETA DECAY 20.73
10BE + n = 11BE + 0.50 MeV
9BE + 2n = 11BE + 7.32
6HE + a + n = 11BE + 7.91
7HE + a = 11BE + 8.36
6HE + 5HE = 11BE + 8.81
2a + 3n = 11BE + 8.89
8BE + 3n = 11BE + 8.98
5HE + a + 2n = 11BE + 9.78
5HE + 5HE + n = 11BE + 10.68
8LI + t = 11BE + 15.72
7LI + n + t = 11BE + 17.75
9LI + d = 11BE + 17.92
9LI + p + n = 11BE + 20.14
a + 2t + n = 11BE + 20.22
7LI + 4H = 11BE + 20.57

11BE => 11B MAXIMUM EXCITATION ENERGY FROM BETA DECAY 11.51
7LI + a = 11B + 8.66 MeV
2a + t = 11B + 11.13
8BE + t = 11B + 11.22
10BE + p = 11B + 11.23
10B + n = 11B + 11.45

12BE => 12B MAXIMUM EXCITATION ENERGY FROM BETA DECAY 11.71
11B + n = 12B + 3.37 MeV

8LI + a = 12B + 10.00

14BE => 14B MAXIMUM EXCITATION ENERGY FROM BETA DECAY 17.36

13B + n = 14B + 0.97 MeV
12B + 2n = 14B + 5.85
11B + 3n = 14B + 9.22
11BE + t = 14B + 11.46
9LI + a + n = 14B + 11.79
10BE + t + n = 14B + 11.96
10LI + a = 14B + 12.59
9LI + 5HE = 14B + 12.68
12BE + d = 14B + 14.55
10BE + 4H = 14B + 14.78
8LI + 6HE = 14B + 14.87
8LI + a + 2n = 14B + 15.85
8LI + 5HE + n = 14B + 16.74
12BE + p + n = 14B + 16.77
7LI + 6HE + n = 14B + 16.91
7LI + 7HE = 14B + 17.35

12B => 12C MAXIMUM EXCITATION ENERGY FROM BETA DECAY 13.37

3a = 12C + 7.27 MeV
8BE + a = 12C + 7.37

13B => 13C MAXIMUM EXCITATION ENERGY FROM BETA DECAY 13.44

12C + n = 13C + 4.95 MeV
9BE + a = 13C + 10.65
3a + n = 13C + 12.22
8BE + a + n = 13C + 12.31
5HE + 2a = 13C + 13.11
8BE + 5HE = 13C + 13.21

14B => 14C MAXIMUM EXCITATION ENERGY FROM BETA DECAY 20.64

13C + n = 14C + 8.18 MeV
10BE + a = 14C + 12.01
12C + 2n = 14C + 13.12
9BE + a + n = 14C + 18.82
6HE + 2a = 14C + 19.42
8BE + 6HE = 14C + 19.51
9BE + 5HE = 14C + 19.72
3a + 2n = 14C + 20.40
8BE + a + 2n = 14C + 20.49
11B + t = 14C + 20.60

15B => 15C MAXIMUM EXCITATION ENERGY FROM BETA DECAY 19.10

14C + n = 15C + 1.22 MeV
13C + 2n = 15C + 9.39
11BE + a = 15C + 12.73
10BE + a + n = 15C + 13.23
10BE + 5HE = 15C + 14.12
12C + 3n = 15C + 14.34
12B + t = 15C + 18.45
9BE + 6HE = 15C + 19.07

17B => 17C MAXIMUM EXCITATION ENERGY FROM BETA DECAY 22.98

16C + n = 17C + 0.74 MeV
15C + 2n = 17C + 4.99
14C + 3n = 17C + 6.20
13C + 4n = 17C + 14.38
12BE + a + n = 17C + 14.54
12BE + 5HE = 17C + 15.44
11BE + 6HE = 17C + 16.74
10BE + 6HE + n = 17C + 17.24
14B + t = 17C + 17.58
10BE + 7HE = 17C + 17.69
11BE + a + 2n = 17C + 17.71
10BE + a + 3n = 17C + 18.22
13B + t + n = 17C + 18.55
11BE + 5HE + n = 17C + 18.61
10BE + 5HE + 2n = 17C + 19.11
12C + 5n = 17C + 19.32
15B + d = 17C + 21.08
13B + 4H = 17C + 21.37
9BE + 8HE = 17C + 21.92

16C => 16N MAXIMUM EXCITATION ENERGY FROM BETA DECAY 8.01

15N + n = 16N + 2.49 MeV

17C => 17N MAXIMUM EXCITATION ENERGY FROM BETA DECAY 13.16

16N + n = 17N + 5.88 MeV
15N + 2n = 17N + 8.37
14C + t = 17N + 10.10
13B + a = 17N + 11.12
16C + p = 17N + 13.11

18C => 18N MAXIMUM EXCITATION ENERGY FROM BETA DECAY 11.77

17N + n = 18N + 2.83 MeV
16N + 2n = 18N + 8.71
15N + 3n = 18N + 11.20
15C + t = 18N + 11.71

19C => 19N MAXIMUM EXCITATION ENERGY FROM BETA DECAY 16.89

18N + n = 19N + 5.32 MeV
17N + 2n = 19N + 8.14
16C + t = 19N + 12.77
16N + 3n = 19N + 14.02
15B + a = 19N + 15.52
18C + p = 19N + 16.31
15N + 4n = 19N + 16.51

20C => 20N MAXIMUM EXCITATION ENERGY FROM BETA DECAY 15.93

19N + n = 20N + 1.84 MeV
18N + 2n = 20N + 7.16
17N + 3n = 20N + 9.98
17C + t = 20N + 13.88
16C + t + n = 20N + 14.62
16N + 4n = 20N + 15.87

18C + d = 20N + 15.93

16N => 160 MAXIMUM EXCITATION ENERGY FROM BETA DECAY 10.42
12C + a = 160 + 7.16 MeV

17N => 170 MAXIMUM EXCITATION ENERGY FROM BETA DECAY 8.68
160 + n = 170 + 4.14 MeV
13C + a = 170 + 6.36

18N => 180 MAXIMUM EXCITATION ENERGY FROM BETA DECAY 13.90
14C + a = 180 + 6.23 MeV
170 + n = 180 + 8.04
160 + 2n = 180 + 12.19

19N => 190 MAXIMUM EXCITATION ENERGY FROM BETA DECAY 12.54
180 + n = 190 + 3.96 MeV
15C + a = 190 + 8.97
14C + a + n = 190 + 10.18
14C + 5HE = 190 + 11.08
170 + 2n = 190 + 12.00

20N => 200 MAXIMUM EXCITATION ENERGY FROM BETA DECAY 18.30
190 + n = 200 + 7.61 MeV
180 + 2n = 200 + 11.56
16C + a = 200 + 12.32
15C + a + n = 200 + 16.57
14C + 6HE = 200 + 16.82
15C + 5HE = 200 + 17.47
14C + a + 2n = 200 + 17.79

21N => 210 MAXIMUM EXCITATION ENERGY FROM BETA DECAY 17.92
200 + n = 210 + 3.74 MeV
190 + 2n = 210 + 11.34
180 + 3n = 210 + 15.30
17C + a = 210 + 15.32
16C + a + n = 210 + 16.06
16C + 5HE = 210 + 16.95

190 => 19F MAXIMUM EXCITATION ENERGY FROM BETA DECAY 4.82
15N + a = 19F + 4.01 MeV

210 => 21F MAXIMUM EXCITATION ENERGY FROM BETA DECAY 8.18
20F + n = 21F + 8.10 MeV

220 => 22F MAXIMUM EXCITATION ENERGY FROM BETA DECAY 6.61
21F + n = 22F + 5.19 MeV

230 => 23F MAXIMUM EXCITATION ENERGY FROM BETA DECAY 14.11
22F + n = 23F + 7.55 MeV
21F + 2n = 23F + 12.74
220 + p = 23F + 13.38

20F => 20NE MAXIMUM EXCITATION ENERGY FROM BETA DECAY 7.03
160 + a = 20NE + 4.73 MeV

22F => 22NE MAXIMUM EXCITATION ENERGY FROM BETA DECAY 10.86
180 + a = 22NE + 9.67 MeV
21NE + n = 22NE + 10.36

23F => 23NE MAXIMUM EXCITATION ENERGY FROM BETA DECAY 8.51
22NE + n = 23NE + 5.20 MeV

24F => 24NE MAXIMUM EXCITATION ENERGY FROM BETA DECAY 14.70
23NE + n = 24NE + 8.87 MeV
200 + a = 24NE + 12.17
22NE + 2n = 24NE + 14.07

25F => 25NE MAXIMUM EXCITATION ENERGY FROM BETA DECAY 14.70
24NE + n = 25NE + 4.28 MeV
210 + a = 25NE + 12.71
23NE + 2n = 25NE + 13.15

Neutron Deficient Nuclei:

```
8B    => 8BE       MAXIMUM EXCITATION ENERGY FROM BETA DECAY  16.96
           a   + a  =   8BE  + -0.09 MeV

9C    => 9B        MAXIMUM EXCITATION ENERGY FROM BETA DECAY  15.48
     a   + p   + a  =   9B   + -0.28 MeV
           8BE  + p  =   9B   + -0.19
           5LI  + a  =   9B   +  1.69

12N   => 12C       MAXIMUM EXCITATION ENERGY FROM BETA DECAY  16.32
     a   + a   + a  =   12C  +  7.27 MeV
           8BE  + a  =   12C  +  7.37
           11B  + p  =   12C  + 15.96

13O   => 13N       MAXIMUM EXCITATION ENERGY FROM BETA DECAY  16.74
          12C  + p  =   13N  +  1.94 MeV
   a   + a   + a   + p =   13N  +  9.22
       8BE  + p   + a  =   13N  +  9.31
            9B    + a  =   13N  +  9.50
       5LI  + a   + a  =   13N  + 11.18
            5LI   + 8BE =   13N  + 11.28

17NE  => 17F       MAXIMUM EXCITATION ENERGY FROM BETA DECAY  13.51
          16O  + p  =   17F  +  0.60 MeV
           13N + a  =   17F  +  5.82
       12C + p  + a  =   17F  +  7.76
           12C + 5LI =   17F  +  9.73
       15N + p  + p  =   17F  + 12.73

20NA  => 20NE      MAXIMUM EXCITATION ENERGY FROM BETA DECAY  12.87
          16O  + a  =   20NE +  4.73 MeV
       12C + a  + a  =   20NE + 11.90
           12C + 8BE =   20NE + 11.99
           19F + p   =   20NE + 12.85

20MG  => 20NA      MAXIMUM EXCITATION ENERGY FROM BETA DECAY   9.71
         19NE  + p  =   20NA +  2.20 MeV
       15O + p  + a  =   20NA +  5.73
           16F  + a  =   20NA +  6.26
           15O  + 5LI =  20NA +  7.69
       18F + p  + p  =   20NA +  8.61

21MG  => 21NA      MAXIMUM EXCITATION ENERGY FROM BETA DECAY  12.08
         20NE  + p  =   21NA +  2.43 MeV
           17F + a  =   21NA +  6.57
       16O + p  + a  =   21NA +  7.17
           16O + 5LI =   21NA +  9.13

22AL  => 22MG      MAXIMUM EXCITATION ENERGY FROM BETA DECAY  17.41
          21NA + p  =   22MG +  5.50 MeV
       20NE + p  + p  =  22MG +  7.93
```

18NE + a = 22MG + 8.14
17F + p + a = 22MG + 12.06
16O + p + a + p = 22MG + 12.66
14O + a + a = 22MG + 13.25
14O + 8BE = 22MG + 13.34
17F + 5LI = 22MG + 14.03
16O + 6BE = 22MG + 14.03
16O + p + 5LI = 22MG + 14.63
12C + 10C = 22MG + 16.10
19NE + 3HE = 22MG + 17.08

23AL => 23MG MAXIMUM EXCITATION ENERGY FROM BETA DECAY 11.22
22NA + p = 23MG + 7.58 MeV
19NE + a = 23MG + 9.65

24AL => 24MG MAXIMUM EXCITATION ENERGY FROM BETA DECAY 12.86
20NE + a = 24MG + 9.31 MeV
23NA + p = 24MG + 11.69

24SI => 24AL MAXIMUM EXCITATION ENERGY FROM BETA DECAY 9.79
23MG + p = 24AL + 1.87 MeV
20NA + a = 24AL + 9.32
22NA + p + p = 24AL + 9.45

25SI => 25AL MAXIMUM EXCITATION ENERGY FROM BETA DECAY 11.72
24MG + p = 25AL + 2.27 MeV
21NA + a = 25AL + 9.15
20NE + p + a = 25AL + 11.58

27P => 27SI MAXIMUM EXCITATION ENERGY FROM BETA DECAY 10.61
26AL + p = 27SI + 7.46 MeV
23MG + a = 27SI + 9.34

28P => 28SI MAXIMUM EXCITATION ENERGY FROM BETA DECAY 13.31
24MG + a = 28SI + 9.98 MeV
27AL + p = 28SI + 11.58

28S => 28P MAXIMUM EXCITATION ENERGY FROM BETA DECAY 10.27
27SI + p = 28P + 2.06 MeV
26AL + p + p = 28P + 9.53
24AL + a = 28P + 9.53

29S => 29P MAXIMUM EXCITATION ENERGY FROM BETA DECAY 12.77
28SI + p = 29P + 2.75 MeV
25AL + a = 29P + 10.46
24MG + p + a = 29P + 12.73

31CL => 31S MAXIMUM EXCITATION ENERGY FROM BETA DECAY 10.95
30P + p = 31S + 6.13 MeV
27SI + a = 31S + 9.08

32CL => 32S MAXIMUM EXCITATION ENERGY FROM BETA DECAY 11.66
28SI + a = 32S + 6.95 MeV

31P + p = 32S + 8.86

32AR => 32CL MAXIMUM EXCITATION ENERGY FROM BETA DECAY 10.13
31S + p = 32CL + 1.57 MeV
30P + p + p = 32CL + 7.70
28P + a = 32CL + 8.59

33AR => 33CL MAXIMUM EXCITATION ENERGY FROM BETA DECAY 10.60
32S + p = 33CL + 2.28 MeV
29P + a = 33CL + 6.48
28SI + p + a = 33CL + 9.23

35K => 35AR MAXIMUM EXCITATION ENERGY FROM BETA DECAY 10.86
34CL + p = 35AR + 5.90 MeV
31S + a = 35AR + 6.43

36K => 36AR MAXIMUM EXCITATION ENERGY FROM BETA DECAY 11.78
32S + a = 36AR + 6.64 MeV
35CL + p = 36AR + 8.51

36CA => 36K MAXIMUM EXCITATION ENERGY FROM BETA DECAY 9.96
35AR + p = 36K + 1.67 MeV
32CL + a = 36K + 6.52
34CL + p + p = 36K + 7.56
31S + p + a = 36K + 8.09

37CA => 37K MAXIMUM EXCITATION ENERGY FROM BETA DECAY 10.62
36AR + p = 37K + 1.86 MeV
33CL + a = 37K + 6.22
32S + p + a = 37K + 8.50
35CL + p + p = 37K + 10.36
32S + 5LI = 37K + 10.46

38CA => 38K MAXIMUM EXCITATION ENERGY FROM BETA DECAY 5.72
37AR + p = 38K + 5.14 MeV

40SC => 40CA MAXIMUM EXCITATION ENERGY FROM BETA DECAY 13.30
36AR + a = 40CA + 7.04 MeV
39K + p = 40CA + 8.33

40TI => 40SC MAXIMUM EXCITATION ENERGY FROM BETA DECAY 10.44
39CA + p = 40SC + 0.54 MeV
36K + a = 40SC + 5.53
38K + p + p = 40SC + 6.30
35AR + p + a = 40SC + 7.19
35AR + 5LI = 40SC + 9.16

41TI => 41SC MAXIMUM EXCITATION ENERGY FROM BETA DECAY 11.92
40CA + p = 41SC + 1.09 MeV
37K + a = 41SC + 6.27
36AR + p + a = 41SC + 8.13
39K + p + p = 41SC + 9.41
36AR + 5LI = 41SC + 10.09

```
42TI  => 42SC      MAXIMUM EXCITATION ENERGY FROM BETA DECAY   5.98
          41CA + p  =   42SC + 4.27 MeV
             38K + a  =   42SC + 5.75

43TI  => 43SC      MAXIMUM EXCITATION ENERGY FROM BETA DECAY   5.85
          39K  + a  =   43SC + 4.81 MeV
             42CA + p  =   43SC + 4.93

43V   => 43TI      MAXIMUM EXCITATION ENERGY FROM BETA DECAY  10.38
          39CA + a  =   43TI + 4.47 MeV
             42SC + p  =   43TI + 4.49
       41CA + p  + p  =   43TI + 8.76
             40CA + 3HE =   43TI + 9.41
       38K  + p  + a  =   43TI + 10.23

44V   => 44TI      MAXIMUM EXCITATION ENERGY FROM BETA DECAY  12.73
          40CA + a  =   44TI + 5.13 MeV
             43SC + p  =   44TI + 8.65
       36AR + a  + a  =   44TI + 12.17

44CR  => 44V       MAXIMUM EXCITATION ENERGY FROM BETA DECAY   9.56
          43TI + p  =   44V  + 1.77 MeV
             40SC + a  =   44V  + 5.70
       39CA + p  + a  =   44V  + 6.24
       42SC + p  + p  =   44V  + 6.25
             39CA + 5LI =   44V  + 8.20

45CR  => 45V       MAXIMUM EXCITATION ENERGY FROM BETA DECAY  11.39
          44TI + p  =   45V  + 1.61 MeV
             41SC + a  =   45V  + 5.66
       40CA + p  + a  =   45V  + 6.74
             40CA + 5LI =   45V  + 8.71
       43SC + p  + p  =   45V  + 10.26

46CR  => 46V       MAXIMUM EXCITATION ENERGY FROM BETA DECAY   6.58
          45TI + p  =   46V  + 5.36 MeV

47CR  => 47V       MAXIMUM EXCITATION ENERGY FROM BETA DECAY   6.43
          46TI + p  =   47V  + 5.17 MeV

46MN  => 46CR      MAXIMUM EXCITATION ENERGY FROM BETA DECAY  15.98
          45V  + p  =   46CR + 4.89 MeV
       44TI + p  + p  =   46CR + 6.50
             42TI + a  =   46CR + 6.77
       41SC + p  + a  =   46CR + 10.54
  40CA + p  + a  + p  =   46CR + 11.63
       38CA + a  + a  =   46CR + 12.26
             41SC + 5LI =   46CR + 12.51
       40CA + p  + 5LI =   46CR + 13.59
             43TI + 3HE =   46CR + 15.08
  43SC + p  + p  + p  =   46CR + 15.15
```

47MN => 47CR MAXIMUM EXCITATION ENERGY FROM BETA DECAY 10.88
46V + p = 47CR + 4.77 MeV
43TI + a = 47CR + 7.66
45TI + p + p = 47CR + 10.12

48MN => 48CR MAXIMUM EXCITATION ENERGY FROM BETA DECAY 12.58
44TI + a = 48CR + 7.69 MeV
47V + p = 48CR + 8.10

49FE => 49MN MAXIMUM EXCITATION ENERGY FROM BETA DECAY 12.12
48CR + p = 49MN + 2.08 MeV
45V + a = 49MN + 8.16
44TI + p + a = 49MN + 9.78
47V + p + p = 49MN + 10.18
44TI + 5LI = 49MN + 11.74

50FE => 50MN MAXIMUM EXCITATION ENERGY FROM BETA DECAY 7.13
49CR + p = 50MN + 4.59 MeV

51FE => 51MN MAXIMUM EXCITATION ENERGY FROM BETA DECAY 7.00
50CR + p = 51MN + 5.27 MeV

51CO => 51FE MAXIMUM EXCITATION ENERGY FROM BETA DECAY 11.78
50MN + p = 51FE + 4.88 MeV
47CR + a = 51FE + 8.09
49CR + p + p = 51FE + 9.47

52CO => 52FE MAXIMUM EXCITATION ENERGY FROM BETA DECAY 13.01
51MN + p = 52FE + 7.38 MeV
48CR + a = 52FE + 7.94
50CR + p + p = 52FE + 12.65

53NI => 53CO MAXIMUM EXCITATION ENERGY FROM BETA DECAY 12.21
52FE + p = 53CO + 1.60 MeV
49MN + a = 53CO + 7.45
51MN + p + p = 53CO + 8.98
48CR + p + a = 53CO + 9.54
48CR + 5LI = 53CO + 11.50

54NI => 54CO MAXIMUM EXCITATION ENERGY FROM BETA DECAY 7.78
53FE + p = 54CO + 4.35 MeV

55NI => 55CO MAXIMUM EXCITATION ENERGY FROM BETA DECAY 7.67
54FE + p = 55CO + 5.06 MeV

56CU => 56NI MAXIMUM EXCITATION ENERGY FROM BETA DECAY 14.38
55CO + p = 56NI + 7.17 MeV
52FE + a = 56NI + 8.00
54FE + p + p = 56NI + 12.23

57CU => 57NI MAXIMUM EXCITATION ENERGY FROM BETA DECAY 7.68
56CO + p = 57NI + 7.33 MeV
53FE + a = 57NI + 7.56

LIST OF REFERENCES

LIST OF REFERENCES

AGUILAR-BENITEZ88 Aguilar-Benitez, M. et al. Particle Data Group, "Particle Properties Data Booklet, April 1988.", and "Review of Particle Properties," Phys. Lett. B204, (1988).

AJZENBERG-SELOVE86 Ajzenberg-Selove, F., Nucl. Phys. A460, (1986), 1.

AJZENBERG-SELOVE87 Ajzenberg-Selove, F., Nucl. Phys. A475, (1987), 1.

AJZENBERG-SELOVE88 Ajzenberg-Selove, F., Nucl. Phys. A490, (1988), 1.

ALBURGER81 Alburger, D. E., D. J. Millener and D. H. Wilkinson, Phys. Rev. C23, (1981), 473.

ARNISON83 Arnison, G. et al. UA1 Collaboration, CERN, Geneva, Switzerland, Phys. Lett. 122B, No. 1, (1983), 103.

ASAHI84 Asahi, K., K. Matsuta, K. Takeyama, K. H. Tanaka, K. Ise, Y. Nojiri and T. Minamisono, Osaka University Laboratory of Nuclear Studies (OULNS) Annual Report for 1983, (1984), 74.

AWAYA79 Awaya, T., Nucl. Inst. Meth. 165, (1979), 317.

AWAYA80 Awaya, T., Nucl. Inst. Meth. 174, (1980), 237.

BANNER83 Banner, M. et al. UA2 Collaboration, CERN, Geneva, Switzerland, Phys. Lett. 122B, No. 5,6, (1983), 476.

BARNES73 Barnes, C. A., and Davis B. Nichols, Nucl. Phys. A217, (1973), 125.

BARNETT82 Barnett, A. R., Comput. Phys. Commun. 27, (1982), 147.

BECCHETTI81 Becchetti, F. D., C. A. Fields, R. S. Raymond, H. C. Bhang and D. Overway, Phys. Rev. C24, (1981), 2401.

BEHRENS82 H. Behrens and W. Bühring, "Electron Radial Wave Functions and Nuclear Beta-Decay," (Clarendon, Oxford, 1982).

BROWN87 Brown, B. A., and B. H. Wildenthal, Nucl. Phys. A474, (1987), 290.

BROWN85 B. A. Brown, and B. H. Wildenthal, At. Dat. Nuc. Dat. Tab. 33, (1985), 347.

CASKEY88 Caskey, G., L. Heilbronn, B. Remington, A. Galonsky, F. Deak, A. Kiss and Z. Seres, Phys. Rev. C37, (1988), 969.

CLAYTON69 Clayton, Donald. D., "Principles of Stellar Evolution and Nucleosynthesis," (McGraw-Hill, New York, 1968), p. 411.

CURTIN86 Curtin, M. S., L. H. Harwood, J. A. Nolen, B. Sherrill, Z. Q. Xie and B. A. Brown, Phys. Rev. Lett. 56, (1986), 34.

DUFOUR87 Dufour, J. P., R. Del Moral, F. Hubert, D. Jean, M. S. Pravikoff, A. Fleury, H. Delagrange, A. C. Mueller, K. -H. Schmidt, E. Hanelt, K. Summerer, J. Frehaut, M. Beau and G. Giraudet In Proceedings of the Fifth International Conference on Nuclei Far From Stability, Rosseau Lake, Ontario Canada, 1987, AIP, edited by Ian S. Towner, p344.

EHRMAN51 Ehrman, Joachim B., Phys. Rev. 81, (1951), 412.

ESTERL72 Esterl, John E., David Allred, J. C. Hardy, R. G. Sextro and Joseph Cerny, Phys. Rev. C6, (1972), 373.

ESTERL70 Esterl, J. E., J. C. Hardy, R. G. Sextro and J. Cerny,

FERMI33 E. Fermi, Ric. Sci. pt 12, (1933), and Z. Phys. 88, (1934), 1161.

FREEDMAN85 Freedman, S. J., "Correlation Coefficients in Polarized Neutron Decay - Experiments with PERKEO", Invited Talk, Workshop on The Investigation of Fundamental Interactions with Cold Neutrons, National Bureau of Standards, Gaithersburg, MD, November 1985, and Argonne National Laboratory Reprint PHY-4682-WI-85 (1985)

FREEDMAN86 Freedman, S. J., "Modern Implications of Neutron β-decay", Invited Talk - 2nd Conference on the Intersections Between Particle and Nuclear Physics, Lake Louise, Canada, May 1986, and Argonne National Laboratory Reprint PHY-4806-WI-86 (1986)

GAGLIARDI83 Gagliardi, C. A., G. T. Garvey, J. R. Wrobel and S. J. Freedman, Phys. Rev. C28, (1983), shit

GAMOW36 G. Gamow and E. Teller, Phys. Rev. 49, (1936), 895.

GIL88 Gil, S., E. Adelberger, A. Garcia, J. Gundlach, D. Mikolas, T. Murakami, W. Oliver and W. F. Rogers,

University of Washington Nuclear Physics Laboratory Annual Report, (1988), 2.

GLASHOW81 Glashow, S. L., Physica 96A, (1981), 27.

GOLDHABER74 Goldhaber et al. Phys. Lett. 53B, (1974), 306

GOLDHABER78 Goldhaber and Heckman, Ann. Rev. Nuc. Part. Sci., 28, (1978), 161.

GOODMAN65 Proceedings of the Conference on Correlations of Particles Emitted in Nuclear Reactions, Introduced by Goodman, Charles D., Rev. Mod. Phys. 37, (1965), 327.

GREINER75 Greiner, W. ET AL. Phys. Rev. Lett. 35, (1975), 152.

HAMEL85 Hamel, L. A., L. Lessard, H. Jeremie and J. Chauvin, Z. Phys. A321, (1985), 439.

HARDY65 Hardy, J. C., R. I. Verrall, R. Barton and R. E. Bell, Phys. Rev. Lett. 14, (1965), 376.

HARDY89 Hardy, J. C., I. S. Towner, V. T. Koslowsky, E. Hagberg and H. Schmeing, "Superallowed $0^+ \rightarrow 0^+$ Nuclear β decays: a Critical Survey with Tests of CVC and the Standard Model." Preprint TASCC-P-89-4, submitted Nucl. Phys. A. (1989)

HARKEWICZ89 Harkewicz, R. et al. Annual Report to be written!

HEATH85 Health, Alexandra R. and Gerald T. Garvey, Phys. Rev. C31, (1985),

HENLEY60 Henley, E. M. and P. D. Kunz, Phys. Rev. 118, (1960), 248.

HOLSTEIN74 Holstein, Barry R., Rev. Mod. Phys., 46, (1974), 789.

HUFNER85 Hufner, J. Phys. Rep. 125, (1985), 129.

KOBAYASHI88 Kobayashi, T. et al., Phys. Rev. Lett. 60, (1988), 2599.

KOSLOWSKY88 Koslowsky, V. T., E. Hagberg, J. C. Hardy, H. Schmeing, R. E. Azuma, and I. S. Towner, "Fermi β-Decay: an Experimental Summary," preprint, 1988.

KONOPINSKI66 E. J. Konopinski, "The Theory of Beta Radioactivity," (Oxford Univ. Press (Clarendon), London/New York, 1966).

KROLLE87 Krolle, D., K. Langanke, and C. Rolfs, Z. Phys. A328, (1987), 291.

LANE58 Lane, A. M. and R. G. Thomas, Rev. Mod. Phys. 30, (1958), 257.

LANGEVIN81 Langevin M., C. Detraz, D. Guillemaud, F. Naulin, M. Epherre, R. Klapisch, S. K. T. Mark, M. de Saint Simon, C. Thibault and F. Touchard, Nucl. Phys. A366, (1981), 449.

LYNCH87 Lynch, W. G., Ann. Rev. Nucl. Part. Sci. (1987), 493.

LYONS88a Lyons, Louis. and Peter Clifford, Nucl. Inst. Meth. A274, (1989), 557, and "How to Measure lifetimes with fractional errors smaller than $1/\sqrt{N}$," Oxford Nuclear Physics Laboratory preprint, March, 1988.

LYONS88b Lyons, L. et. al., Rep. Prog. Phys. 52, (1989), 1015.

MARION68 Marion, J. B. and F. C. Young, Nuclear Reaction Analysis (North-Holland, Amsterdam, 1968), pp.84-95 and 147.

MATT64 Matt, E., H. Pfander, H. Rieseberg and V. Soergel, Phys. Lett. 9, (1964), 174.

MAYER55 M. G. Mayer and J. H. D. Jensen, "Elementary theory of Nuclear Shell Structure," Wiley, NY (1955).

MIKOLAS88a Mikolas, D., B. A. Brown, W. Benenson, L. H. Harwood, E. Kashy, J. A. Nolen Jr., B. Sherrill, J, Stevenson, J. S. Winfield, Z. Q. Xie and R. Sherr, Phys. Rev. C37, (1988), 766.

MIKOLAS88b Mikolas, et al., National Superconducting Cyclotron Laboratory Annual Report, (1987).

MILLENER82 Millener, D. J., D. E. Alburger, E. K. Warburton and D. H. Wilkinson, Phys. Rev. C26, (1982), 1167.

MINAMISONO83 Minamisono, T., K. Takeyama, T. Ishigai, H. Takeshima, Y. Nojiri and K. Asahi, Phys. Lett. 130B, (1983), shit.

MINAMISONO84 Minamisono, T., Y. Nojiri, K. Asahi, K. H. Tanaka, K. Matsuta, K. Ise and K. Takeyama, Research Center for Nuclear Physics (RCNP) Annual Report for 1983, (1984) 130.

MORRISSEY79 Morrissey, D. J., L. F. Oliviera, J. O. Rasmussen, G. T. Seaborg, Y. Yariv, Z. Fraenkel, Phys. Rev. Lett. 43, (1979), 1139.

MORRISSEY89 Morrissey, D. J., Phys. Rev. C39, (1989), 460.

MORITA73 M. Morita, "Beta Decay and Muon Capture," (W. A. Benjamin, Reading, Mass., 1973).

MUELLER88 Mueller, A. C., D. Bazin, W. C. Schmidt-Ott, R. Anne, D. Guerreau, D. Guillemaud-Mueller, M. G. Saomt-Laurent, V. Borrel, J. C. Jacmart, F. Pougheon, and A. Richard, Z. GANIL Preprint P.88-02. (1988)

MURPHY82 Murphy, M. J., T. J. Symons, G. D. Westfall, and H. J. Crawford, Phys. Rev. Lett. 49, (1982), 455.

NAYAK88 Tapan Kumar Nayak. Private Communication.

NOLEN69 Nolen, J. A. Jr. and J. P. Schiffer, Ann. Rev. Nucl. Sci. 19, (1969), 471

NOLEN84 Nolen, J. A. Jr., L. H. Harwood, M. S. Curtin, E. Ormand and S. Bricker, "Instrumentation for Heavy Ion Nuclear Research," Proceedings of the International Conference on Instrumentation for Heavy Ion Research, Oak Ridge National Laboratory, Tennessee (Harwood Academic, New York, 1984).

NYMAN81 Nyman, G., R. E. Azuma, B. Jonson, K.-L. Kratz, P. O. Larsson, S. Mattsson and W. Ziegert, in Proceedings of the Fourth International Conference on Nuclei Far from Stability, Helsingør, 1981, edited by L. O. Skolen, Vol. I, p. 312.

OLIVEIRA79 Oliveira, Luiz, Raul Donangelo, John O. Rasmussen, Phys. Rev. C19, (1979), 826.

OLNESS82 Olness, J. W., E. K. Warburton, D. E. Alburger, C. J. Lister and D. J. Millener, Nucl. Phys. A373, (1982), 13.

ORMAND84 Ormand, E. National Superconducting Cyclotron Laboratory Annual Report, 1984.

ORMAND85 Ormand, W. E. and B. A. Brown, Nucl. Phys. A440, (1985), 274.

ORMAND86 Ormand, W. E. and B. A. Brown, Phys. Lett. B174, (1986), 128.

ORMAND89 Ormand, W. E. and B. A. Brown, Nucl. Phys. A491, (1989), 1.

PAULI33 W. Pauli, Noyaux Atomiques, Proc. Solvay Congr., Brussels (1933), 324.

REINES60 F. Reines and C. Cowan, Phys. Rev. 113, (1960) 273. and F. Reines, C. Cowan, F. B. Harrison, H. W. Kruse, and A. D. McGuire, Phys. Rev. 117, (1960), 159.(discovery of neutrino)

ROBERTSON88 Robertson, R. G. H., and D. A. Knapp, "Direct Measurement of Neutrino Mass," Los Alamos National Lab. Preprint LA-UR-88-291, (1988), and submitted to Ann. Rev. Nucl. Part. Sci.

ROECKL88 Roeckl, E. Nucl. Phys. A488, (1988), 95c-112c.

SAMSONENKO89 Samsonenko, N. V., C. L. Kathat and A. L. Samgin, Nucl. Phys. A491, (1989), 642.

SAMUEL88a Samuel, M., B. A. Brown, D. Mikolas, J. Nolen, B. Sherrill, J. Stevenson, J. S. Winfield, and Z. Q. Xie, Phys. Rev. C37, (1988), 1314.

SAMUEL88b Samuel, M. private communication.

SCHOPPER69 H. Schopper, "Weak Interactions and Nuclear Beta Decay," (North Holland, Amsterdam, 1969).

SCHWALM66 Schwalm, D., and B. Povh, Nucl. Phys. 89, (1966), 401.

SEKINE87 Sekine, T., J. Cerny, R. Kirchner, O. Klepper, V. T. Koslowsky, A. Plochocki, E. Roeckl, D. Schardt, B. Sherrill, and B. A. Brown, Nucl. Phys. A467, (1987), 93.

SHARP55 Sharp, W. T., H. E. Gove and E. B. Paul, Graph of Coulomb Functions, Second Edition, Atomic Energy of Canada Limited AECL No. 268. (1955).

STEVENSON88 Stevenson, J., B. A. Brown, Y. Chen, J. Clayton, E. Kashy, D. Mikolas, J. Nolen, M. Samuel, B. Sherrill, J. S. Winfield, Z. Q. Xie, R. E. Julies and W. A. Richter, Phys. Rev. C37, (1988), 2220.

SWAMI56 Swami, M. S., J. Schnepps and W. F. Fry, Phys. Rev. 103, (1956), 1134.

TANIHATA85a Tanihata, I. et al., Phys. Lett. 160B, (1985), 380.

TANIHATA85b Tanihata, I. et al., Phys. Rev. Lett. 55, (1985), 2676.

TANIHATA88 Tanihata, I. et al., Phys. Lett. 206B, (1988), 592.

THOMAS51 Thomas, R. G. Phys. Rev. 81, (1951), 148L.

TOWNER73a Towner, I. S., Nucl. Phys. A216, (1973), 589.

TOWNER73b Towner, I. S. and J. C. Hardy, Nucl. Phys. A205, (1973), 33.

VENTO84 Vento, V., and J. Navarro, Phys. Lett. 141B, (1984), 28.

VIYOGI78 Viyogi ET. AL. Phys. Rev. Lett. 42 (1978), 33.

WAPSTRA86 A. H. Wapstra and G. Audi, Nucl. Phys. A432, (1985), 1.

WARBURTON86 Warburton, E. K. Phys. Rev. C33, (1986), 303.

WATKINS86 P. Watkins, "Story of the W and Z," (Cambridge University Press, Cambridge, 1986).

WESTFALL79 Westfall, G. D. ET AL. Phys. Rev. C19, (1979), 309.

WESTFALL79 Westfall, G. D., T. J. Symons, D. E> Greiner, H. H. Heckman, J. Lindstrom, J. Mahoney, A. C. Shotter, D. K. Scott, H. J. Crawford, C. McParland, T. C. Awes, C. K. Gelbke and J. M. Kidd, Phys. Rev. Lett. 43, (1979), 1859.

WILKINSON71a Wilkinson, D. H., Phys. Rev. Lett. 27, (1971), 1018.

WILKINSON71b Wilkinson, D. H., D. E. Alburger, D. R. Goosman, K. W. Jones, E. K. Warburton, G. T. Garvey and R. L. Williams, Nucl. Phys. A166, (1971), 661.

WILKINSON73 D. H. Wilkinson, Nucl. Phys. A209, (1973), 470.

WILKINSON74a D. H. Wilkinson and B. E. F. Macefield, Nucl. Phys. A232, (1974), 58. (phase space calculation)

WILKINSON74b D. H. Wilkinson, Nucl. Phys. A232, (1974), 93.

WILKINSON74c Wilkinson, D. H., Phys. Lett. 48B, (1974), 169.

WILKINSON78 D. H. Wilkinson, A. Gallmann, and D. E. Alburger, Phys. Rev. C18, (1978), 401.

WILKINSON82 D. H. Wilkinson, Nucl. Phys. A377, (1982), 474.

ZHAO89 Zhao, Z., M. Gai, B. J. Lund, S. L. Rugari, D. Mikolas, B. A. Brown, J. A. Nolen Jr. and M. Samuel, Phys. Rev. C39, (1989) 1985, and Preprint number YALE-3074-966